

Simultaneous joint migration inversion as a high-resolution time-lapse imaging method for reservoir monitoring

Qu, Shan

DOI

[10.4233/uuid:f22c0da3-9d85-4c3a-9c07-949e242869d6](https://doi.org/10.4233/uuid:f22c0da3-9d85-4c3a-9c07-949e242869d6)

Publication date

2020

Document Version

Final published version

Citation (APA)

Qu, S. (2020). *Simultaneous joint migration inversion as a high-resolution time-lapse imaging method for reservoir monitoring*. [Dissertation (TU Delft), Delft University of Technology]. <https://doi.org/10.4233/uuid:f22c0da3-9d85-4c3a-9c07-949e242869d6>

Important note

To cite this publication, please use the final published version (if applicable). Please check the document version above.

Copyright

Other than for strictly personal use, it is not permitted to download, forward or distribute the text or part of it, without the consent of the author(s) and/or copyright holder(s), unless the work is under an open content license such as Creative Commons.

Takedown policy

Please contact us and provide details if you believe this document breaches copyrights. We will remove access to the work immediately and investigate your claim.

**SIMULTANEOUS JOINT MIGRATION INVERSION AS A
HIGH-RESOLUTION TIME-LAPSE IMAGING METHOD
FOR RESERVOIR MONITORING**

SIMULTANEOUS JOINT MIGRATION INVERSION AS A HIGH-RESOLUTION TIME-LAPSE IMAGING METHOD FOR RESERVOIR MONITORING

Proefschrift

ter verkrijging van de graad van doctor
aan de Technische Universiteit Delft,
op gezag van de Rector Magnificus prof. dr. ir. T.H.J.J. van der Hagen,
voorzitter van het College voor Promoties,
in het openbaar te verdedigen op Woensdag 26 Februari 2020 om 12:30

door

SHAN QU

Master of Engineering in Geophysical Prospecting and Information Technology
China University of Petroleum (Beijing), Beijing, China
geboren te Liaoning, China.

Dit proefschrift is goedgekeurd door de

promoters: Dr. ir. D.J. Verschuur and Prof. dr. ir. N. de Jong

Samenstelling promotiecommissie:

Rector Magnificus,
Dr. ir. D.J. Verschuur,
Prof. dr. ir. N. de Jong,

voorzitter
promotor, Technische Universiteit Delft
promotor, Technische Universiteit Delft

Onafhankelijke leden:

Prof. dr. ir. C. Vuik
Prof. dr. A.W. Martinius
Prof. dr. C. MacBeth
Dr. M. Houbiers
Dr. A.K. Soni

Technische Universiteit Delft
Technische Universiteit Delft
Heriot-Watt University
Equinor
Shell International B.V.



The work in this dissertation was conducted at the section Acoustic Wavefield Imaging (AWI), Faculty of Applied Sciences, Delft University of Technology and was financially supported by the Delphi consortium.

Printed by: Ridderprint B.V.

Copyright © 2020 by S. Qu

ISBN 978-94-6384-115-3

An electronic version of this dissertation is available at

<http://repository.tudelft.nl/>.

给我的家人

To my family

CONTENTS

Summary	xi
Samenvatting	xiii
1 Introduction	1
1.1 Overview of time-lapse seismic technology	2
1.2 The foundation of time-lapse processing workflow — Imaging method.	3
1.2.1 Least-Squares Reverse-Time Migration	4
1.2.2 Full Wavefield Migration	6
1.3 Considering velocity variations between different time-lapse surveys.	6
1.3.1 Time-shift map	6
1.3.2 Full Waveform Inversion	7
1.3.3 Joint Migration Inversion	8
1.4 Sequential vs Simultaneous strategy	10
1.5 Thesis outline	11
References	13
2 Sequential Joint Migration Inversion	19
2.1 Introduction	20
2.2 Full Wavefield Modeling	21
2.2.1 Reflection and transmission at each level	21
2.2.2 Propagation in-between two consecutive levels	22
2.2.3 Recursive modeling scheme	23
2.2.4 Numerical demonstration	24
2.3 Inversion	25
2.3.1 Definition of the objective function	26
2.3.2 Gradients of the reflectivity and propagation velocity	27
2.3.3 Optimization.	28
2.3.4 Numerical demonstration	29
2.4 Example	30
2.5 Discussion	33
2.5.1 Handling AVO effects.	33
2.5.2 Independent processing strategy.	34
2.6 Conclusion	35
References	36

3	High-resolution Simultaneous Joint Migration Inversion	41
3.1	Introduction	42
3.2	Simultaneous JMI	43
3.3	High-resolution S-JMI - Bridging the gap between reflectivity and velocity	44
3.4	Example	46
3.5	Discussion	47
3.5.1	Computational requirements	47
3.5.2	Constraint linking reflectivity and velocity update	48
3.6	Conclusion	48
	References	49
4	A realistic synthetic example and a field data example	51
4.1	Synthetic data example based on Grane model	52
4.1.1	An introduction to the time-lapse model	52
4.1.2	S-JMI as an effective time-lapse processing tool	52
4.1.3	More localized time-lapse changes brought by high-resolution S-JMI	56
4.2	Field data example based on Troll Field	58
4.3	Conclusion	62
4.4	Acknowledgment	63
	References	63
5	Feasibility and Robustness Study	65
5.1	Noise	66
5.1.1	Random noise	66
5.1.2	Coherent noise caused by the acoustic assumption	66
5.2	Quality of time-lapse surveys	67
5.2.1	Sparse surveys	68
5.2.2	Non-repeated surveys	70
5.2.3	Sparse and non-repeated surveys — OBN vs streamer	71
5.3	Non-repeated sources	73
5.3.1	Source positioning errors	73
5.3.2	Non-repeated source wavelets	74
5.4	Robustness to spatial weighting operators	75
5.5	Sensitivity to weak time-lapse effects	76
5.6	Conclusion	76
5.7	Acknowledgment	79
	References	79
6	S-JMI with calender-time constraints for semi-continuous surveys	81
6.1	Introduction	82
6.2	Review of i4D technology	83
6.3	Theory of S-JMI with calender-time constraints	84
6.4	Example	84
6.5	Discussion	89
6.5.1	Computational aspects	89
6.5.2	The feasibility of the calender-time constraints	90

6.6	Conclusion	91
	References	93
7	Conclusion and Recommendations	95
7.1	Conclusion	95
7.2	Recommendations for further research	96
7.2.1	3D extension	96
7.2.2	Including AVO effects	96
7.2.3	Including anisotropic effects	97
7.2.4	Towards target-oriented time-lapse inversion	97
7.2.5	Towards amplitude inversion and elastic inversion	97
7.2.6	Automatic way to choose the spatial weighting operators	97
	References	98
A	Appendix A: Mitigating AVO effects in JMI using local orthogonalization	99
A.1	Introduction	100
A.2	AVO-preserving JMI with Local orthogonalization	101
A.3	Example	101
A.4	Conclusion	104
	References	105
B	Appendix B: JMI with an automatic directional total variation constraint	107
B.1	Introduction	108
B.2	JMI with TV and Directional TV	108
B.3	Example	110
B.4	Discussion	112
B.5	Conclusion	113
	References	113
	Acknowledgement	115
	Curriculum Vitæ	119
	List of Publications	121

SUMMARY

During the past decade, time-lapse seismic technology has been widely applied in hydrocarbon reservoir management. It is a very powerful method to obtain information on reservoir changes in the inter-well regions. This information helps to identify bypassed hydrocarbons and extend the economic life of a field. In a typical scenario, one baseline survey and subsequent monitoring surveys are acquired over time. The survey geometry is usually exactly repeated and well-sampled to mitigate acquisition effects on the next steps in the process. By processing and comparing all the datasets, some physical changes, e.g. reflection amplitude and travel-time changes, can be estimated. These time-lapse changes are then used to calculate interpretable parameter changes in dynamic reservoir rock and fluid properties, e.g. pore pressure and fluid saturation.

In a conventional time-lapse processing workflow, all the multiples are first removed from the data, then independent imaging process is employed to each dataset, given the same propagation velocity model. Later on, to compensate the ignored velocity variations between different surveys, a time-shift map (travel-time differences) is estimated from the calculated images and then applied back to them, yielding the final reflection amplitude differences. However, this conventional processing strategy is usually sensitive to the success of multiple removal and survey repeatability, and also requires well-sampled surveys providing proper illumination. Moreover, artifacts are often generated in addition to the actual time-lapse changes due to the non-repeatable uncertainties during the independent processing steps. Regarding the time-shift-map tool, the relative velocity changes derived from the time-shift map are not the actual velocity changes due to its local 1D subsurface assumption that is embedded.

In order to relax these rigid requirements and have a better velocity change indicator, we propose Simultaneous Joint Migration Inversion (S-JMI) as an effective time-lapse tool for reservoir monitoring, which combines a simultaneous time-lapse data processing strategy with the Joint Migration Inversion (JMI) method. JMI is a full wavefield inversion method that explains the measured reflection data using a parameterization in terms of reflectivities and propagation velocities. JMI is able to make use of multiples and at the same time take velocity variations between surveys into account. The simultaneous strategy, which means fitting all the datasets simultaneously, allows the baseline and monitor parameters to communicate and compensate with each other dynamically during inversion via L2-norm constraints, thus, reducing the non-repeatable uncertainties during the time-lapse processing workflow. As a result, more accurate time-lapse differences can be achieved by S-JMI, compared to inverting each dataset independently. Moreover, in order to get more localized time-lapse velocity differences, we further extend the regular S-JMI to a robust high-resolution S-JMI (HR-S-JMI) process by making a link between the reflectivity/reflectivity-difference and velocity/velocity-difference during inversion. With a complex synthetic example based on the Marmousi model, we demonstrate the performance of the time-shift-map-based method, sequential JMI, the regular S-JMI and HR-S-

JMI is improving in this particular order.

Next, we further demonstrate the effectiveness of the proposed method in more real-life cases with a highly realistic synthetic model based on the Grane field, offshore Norway, and a time-lapse field dataset from the Troll Field. Moreover, in order to investigate the feasibility of HR-S-JMI in practice, several numerical experiments based on the realistic Grane model are conducted, regarding the following aspects: noise, including random noise and coherent noise caused by the acoustic assumption; the quality of time-lapse surveys, including sparse surveys, non-repeated surveys, and Ocean Bottom Node (OBN) vs streamer (different types of monitoring surveys); non-repeated sources, including source positioning errors and non-repeated source wavelets; spatial weighting operators in the L2-norm constraints; and sensitivity to weak time-lapse effects. These experiments show that HR-S-JMI is very robust to random noise, coherent noise, survey sparsity, survey non-repeatability, source positioning errors and source wavelet discrepancies. Furthermore, HR-S-JMI remains effective when the spatial weighting operators in the L2-norm constraints are largely relaxed and HR-S-JMI is capable of detecting weak time-lapse changes (e.g. velocity changes down to $\pm 35m/s$). These features make it a suitable time-lapse processing solution for cost-effective (semi-)continuous monitoring, termed i4D survey technology, in which inexpensive localized and sparse surveys are employed between the conventional full-field surveys. The simultaneous strategy of S-JMI allows the full-field survey information to compensate the poor illumination of the in-between sparse surveys during process. Furthermore, calendar-time constraints are proposed and applied to the parameter differences between the baseline and monitors along the calendar-time axis by taking advantage of the feature that time-lapse effects usually develop gradually over time. With a complex synthetic example based on the Marmousi model, we demonstrate that S-JMI is a promising tool to process datasets acquired from (semi-)continuous monitoring, like an i4D survey.

In conclusion, we propose high-resolution simultaneous JMI (HR-S-JMI) as an effective time-lapse processing tool for the following main reasons:

- HR-S-JMI is able to make use of multiples to extend the illumination of the subsurface, instead of removing them;
- HR-S-JMI is an extended imaging process, including automatic velocity updating. Therefore, it takes velocity variations between surveys directly into account;
- HR-S-JMI is a good indicator of velocity changes, it can invert for high-resolution accurate time-lapse velocity changes;
- HR-S-JMI is robust to the uncertainties existing in the monitoring surveys, e.g. noise, sparsity, non-repeatability, source positioning errors, source wavelet discrepancy, etc;
- HR-S-JMI has the ability to detect weak time-lapse changes (velocity changes down to $\pm 35m/s$).

SAMENVATTING

In het afgelopen decennium is de zogenaamde time-lapse seismische technologie breed toegepast in het beheren en monitoren van productie van olie- en gasreservoirs. Het is een effectieve methode om informatie te verkrijgen over veranderingen in het reservoir in de gebieden tussen putten. Deze informatie helpt om achtergebleven delfstoffen te vinden en het economische leven van een veld te verlengen. In een typisch scenario wordt één baseline survey en opeenvolgende monitoring surveys vergaard over tijd. De acquisitie geometrie van de survey wordt over het algemeen exact herhaald en is dicht gesampled, om acquisitie effecten te voorkomen in de vervolgstappen van het proces. Door alle datasets te verwerken en te vergelijken kunnen fysische veranderingen worden geschat, zoals de amplitude van reflecties en veranderingen in de aankomsttijden. Deze veranderingen worden vervolgens gebruikt om veranderingen in de parameters te berekenen die gebruikt worden voor de interpretatie van de dynamische gesteente- en vloeistofeigenschappen, zoals de druk in de poriën en de verzadiging van de vloeistof.

In een conventionele time-lapse processing workflow worden eerst alle meervoudige reflecties uit de data verwijderd, waarna afbeeldingsmethoden worden toegepast op elke dataset afzonderlijk, gegeven een gelijk snelheidsmodel voor propagatie. Om te compenseren voor de snelheidsvariëaties tussen verschillende surveys, welke in eerste instantie genegeerd worden, wordt een zogenaamde time-shift map (verschillen in looptijd) geschat van de verkregen afbeeldingen en vervolgens weer toegepast op deze afbeeldingen, wat de uiteindelijke verschillen in de reflectie amplitudes geeft. Echter, deze conventionele dataverwerkingsstrategie is meestal gevoelig voor het succes van het verwijderen van de meervoudige reflecties en de herhaalbaarheid van de survey, en vereist goedgesampled surveys die voldoende belichting geven. Daarbij worden er vaak artefacten gecreëerd, naast de daadwerkelijke time-lapse veranderingen, door onherhaalbare onzekerheden in de onafhankelijke verwerkingsstappen. Wat betreft het time-shift map aanpak zijn de relatieve veranderingen in de snelheid die afgeleid worden van de time-shift map niet de daadwerkelijke snelheidsveranderingen, door de verankerde aanname van een locale 1D ondergrond.

Om deze strikte voorwaarden te verzwakken en de indicator voor de snelheidsverandering te verbeteren stellen we “Simultaneous Joint Migration Inversion” (S-JMI) voor als een effectieve time-lapse middel voor het monitoren van reservoirs, wat een simultane time-lapse data verwerkingsstrategie combineert met de Joint Migration Inversion (JMI) methode. JMI is een full-wavefield inversie methode die de gemeten reflectiedata verklaart aan de hand van een parametrisatie in termen van reflectiecoëfficiënten en propagatiesnelheden. JMI kan gebruik maken van meervoudige reflecties en kan tegelijkertijd rekening houden met snelheidsvariëaties tussen de verschillende surveys. De simultane strategie, wat betekent dat alle datasets gelijktijdig worden gefit, laat communicatie tussen de baseline en de monitoring surveys toe en laat de surveys elkaar dynamisch compenseren tijdens de inversie via L2-norm randvoorwaarden, waardoor de onherhaalbare

onzekerheden gedurende de time-lapse verwerking workflow afnemen. Hierdoor kan S-JMI preciezere time-lapse verschillen bewerkstelligen in vergelijking met het inverteren van elke dataset afzonderlijk. Bovendien, om meer gelokaliseerde time-lapse snelheidsverschillen te verkrijgen, bereiden we het normale S-JMI proces uit tot een robuuste hoge-resolutie S-JMI (HR-S-JMI) proces door een link te maken tussen de reflectie- en snelheidsverschillen tijdens de inversie. Met een gecompliceerd synthetisch voorbeeld, gebaseerd op het Marmousi model, tonen we aan dat de prestaties van de time-shift-map-gebaseerde methode, sequentiële JMI, normale S-JMI en HR-S-JMI in deze volgorde oplopen.

Vervolgens tonen we de effectiviteit van de voorgestelde methode verder aan in een meer realistische situatie met een zeer realistisch synthetisch model gebaseerd op het Grane veld, voor de kust van Noorwegen, en een time-lapse veld dataset van het Troll veld. Bovendien, om de haalbaarheid van HR-S-JMI in de praktijk te onderzoeken, worden verschillende numerieke experimenten gebaseerd op het realistische Grane model uitgevoerd, met betrekking tot de volgende aspecten: ruis, waaronder random ruis en coherente ruis veroorzaakt door de akoestische aanname; de kwaliteit van time-lapse surveys, waaronder sparse surveys, niet-herhaalde surveys, en Ocean Bottom Node (OBN) vs streamer (verschillende soorten monitoring surveys); niet herhaalde bronnen, waaronder afwijkingen in bron plaatsing en niet herhaalde source wavelets; spatiële weegoperatoren in de L2-norm randvoorwaarden; en gevoeligheid voor zwakke time-lapse effecten. Deze experimenten tonen aan dat HR-S-JMI zeer robuust is voor random ruis, coherente ruis, survey sparsity, survey onherhaalbaarheid, afwijkingen in bron plaatsing en afwijkingen in het bronsignaal. Tevens blijft HR-S-JMI effectief wanneer de spatiële weegoperatoren in de L2-norm randvoorwaarden worden losgelaten, en is HR-S-JMI in staat om kleine time-lapse veranderingen te detecteren (e.g. snelheidsveranderingen tot 35 m/s). Deze eigenschappen maken het een geschikte time-lapse verwerkingsoplossing voor een kosteneffectieve (semi-)continue monitoring, i4D survey technologie genoemd, waarin goedkope gelokaliseerde en sparse surveys worden toegepast tussen de conventionele full-field surveys. De simultane strategie van S-JMI zorgt dat de full-field survey informatie kan compenseren voor de beperkte belichting van de tussentijdse sparse surveys gedurende de verwerking. Tevens worden kalender-tijd randvoorwaarden voorgesteld en toegepast op de parameterverschillen tussen de baseline en de monitor datasets langs de kalender-tijd-as door gebruik te maken van de eigenschap dat time-lapse effecten zich over het algemeen geleidelijk door de tijd heen ontwikkelen. Met een gecompliceerd synthetisch voorbeeld gebaseerd op het Marmousi model laten we zien dat S-JMI een veelbelovende methode is om datasets verkregen van (semi-)continue monitoring, zoals een i4D survey, te verwerken.

Concluderend: we stellen hoge-resolutie simultane JMI (HR-S-JMI) voor als een effectieve time-lapse verwerkingsmethode om de volgende hoofdredenen:

- HR-S-JMI is in staat om gebruik te maken van meervoudige reflecties om de belichting van de ondergrond uit te bereiden, in plaats van ze te verwijderen;
- HR-S-JMI is een uitgebreid afbeeldingsproces, inclusief automatische snelheidsaanpassing. Daardoor houdt het direct rekening met snelheidsveranderingen tussen de surveys;

- HR-S-JMI is een goede indicator van snelheidsveranderingen, het kan inverteren voor hoge-resolutie, accurate, time-lapse snelheidsveranderingen;
- HR-S-JMI is robuust voor de onzekerheden die voorkomen in de monitoring surveys, b.v. ruis, sparsity, onherhaalbaarheid, afwijkingen in bronplaatsing, afwijkingen in de bronsignalen, enzovoorts;
- HR-S-JMI biedt de mogelijkheid om zwakke time-lapse veranderingen te detecteren (snelheidsveranderingen tot 35 m/s).

1

INTRODUCTION

1.1. OVERVIEW OF TIME-LAPSE SEISMIC TECHNOLOGY

Seismic technology plays a key role in oil and gas exploration, in other forms of subsurface inspection or CO_2 injection. In a typical seismic survey, seismic waves are usually generated by imposing artificial seismic energy into the ground. These seismic waves propagate through the subsurface, reflect or refract off the subsurface geological formations, travel back to the surface and then get recorded by an array of sensors. Eventually, the physical properties of the Earth's subsurface can be estimated from the recorded seismic data. Time-lapse seismic technology is a very powerful method to obtain information on production-related changes away from the wells [1, 2]. During the past decade, it has been widely applied in hydrocarbon reservoir management [1–4]. The obtained information from time-lapse seismic helps to identify bypassed oil and extend the economic life of a field. In the case where fluid fronts (i.e. water, steam, CO_2) are injected, time-lapse seismic technology is able to monitor and optimize the costly injection programs [2, 5]. Figure 1.1 shows an example of seismic time-lapse images calculated from the seismic data obtained at the surface. In this case, gas replacing oil in hydrocarbon production is happening due to gas injection. In a typical scenario, one baseline survey and subsequent monitoring surveys are acquired over time. Afterwards, by processing and comparing all the datasets, some physical parameter changes can be estimated. These physical parameters could be seismic reflection amplitudes and travel-times, when imaging-based methods are being used [2, 6]. Or they could be elastic parameters, i.e. compressibility and shear compliance, when amplitude-versus-offset-analysis-based methods are being used [7]. These time-lapse changes are then used to calculate the changes in dynamic reservoir rock and fluid properties, e.g. pore pressure and fluid saturation, which are important in dynamic reservoir interpretation [8, 9].

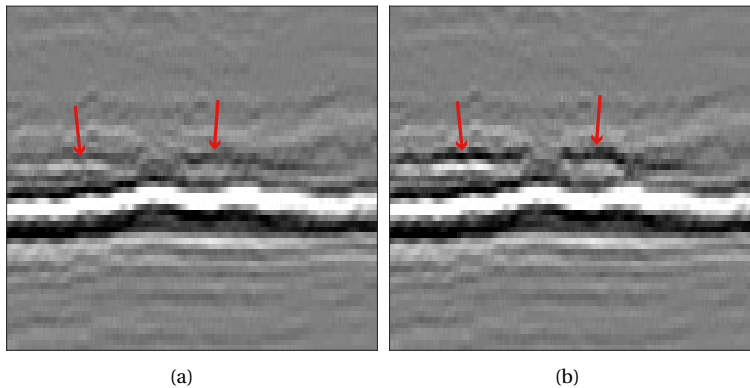


Figure 1.1: An example of seismic time-lapse images calculated from the seismic data obtained at the surface: (a) and (b) the baseline and monitor images. The red arrows point at some time-lapse changes.

1.2. THE FOUNDATION OF SEISMIC TIME-LAPSE PROCESSING WORKFLOW — IMAGING METHODS

Seismic imaging, also known as migration, is a method that uses the principles of seismology to estimate reflectivity images of the Earth's subsurface from seismic data. In the time-lapse scenario, in order to recover seismic reflection amplitude and travel-time changes, the basic step is to perform an imaging process to each dataset produced by monitoring surveys.

Seismic imaging methodologies have been developed continuously in the past decades. There are several ways to categorize these imaging methods:

- **Pre-stack and post-stack**

Post-stack migration operates on the stacked section, which is assumed to be a zero-offset. In contrast, pre-stack imaging is a process in which seismic data is migrated before being stacked, therefore, the data do not need to be reduced to an approximation of zero-offset section before imaging [10]. Improvements are brought by pre-stack imaging when the subsurface structures have complex velocity profiles, though, at the price of a considerable increase in the amount of computations [10]. Nowadays, pre-stack migration is the default method.

- **Time-domain and depth-domain**

Because seismic data are recorded in the time domain, imaging in the time-domain is less sensitive to depth and velocity ambiguities compared to depth-domain imaging methods [11]. Moreover, it is also cost-effective. Therefore, time-domain imaging is still one of the most commonly-used imaging methods in the industry. However, this methodology fails when there exist strong horizontal velocity variations or complex velocity profiles. Depth-domain imaging was proposed to adapt to this kind of complex scenarios [10]. It provides an image by mapping the data from the time-domain directly to the depth-domain given a sufficiently accurate velocity model (propagation velocity).

- **Ray-based, one-way-wave-equation-based, and two-way-wave-equation-based**

Ray-based methods are described in terms of migrating individual traces separately [12]. Kirchhoff migration is the most popular ray-based method. It considers every output grid point in the image as a diffractor that is reached from each source and receiver via a ray-path with certain travel times. These required travel times are often calculated by ray-tracing [13, 14]. Kirchhoff migration is still widely used because it does not require high-quality data and is cost-effective. However, Kirchhoff migration is based on high-frequency approximations, therefore, the accuracy of the resulting images is limited in structurally complex areas [15].

Wave-equation-based imaging methods, which are described in terms of wavefield propagation and an imaging condition, were proposed to address this issue. One-way-wave-equation imaging is based on a one-way approximation to the two-way wave-equation, and it propagates the wavefields upward and downward separately. As a contrast, the full two-way wave-equation propagates the full wavefields in all directions simultaneously [16–20].

For broadband imaging, one-way-wave-equation-based migration is cost-efficient, thus improving the vertical resolution; two-way methodology demands tighter spatial and temporal sampling and is computationally more expensive and memory-intensive. Moreover, one-way-based methods are less sensitive to the errors in the given propagation velocity, compared to two-way wave-equation methods [21]. However, they cannot propagate wavefields beyond 90° . In comparison, two-way methods do not have this dip limitation. [22, 23] proposed to overcome this limitation in the one-way methods by applying the one-way wavefield propagation in a tilted coordinate system. Furthermore, two-way wave-equation-based methods suffer from low-frequency artifacts caused by unwanted cross-correlation of the modeled and back-propagated measured wavefields at non-scattering points along the ray-path, which are not present in the one-way methods [24].

One-way wave-equation migration is usually positioned between ray-based migration and two-way wave-equation migration in terms of accuracy and cost-efficiency.

- **Non-inversion-based and inversion-based**

Inversion-based imaging methods are based on a data-driven process by minimizing the errors in the model with respect to some objective function. This objective function measures how well the data re-modeled from the obtained image fits the recorded data. It has been introduced to provide a subsurface image with more balanced illumination, reduced artifacts, improved resolution, improved signal-to-noise ratio, and more reliable amplitudes [25, 26]. However, the inversion scheme embedded in the imaging methodologies makes it much more expensive, proportional to the number of iterations used during inversion.

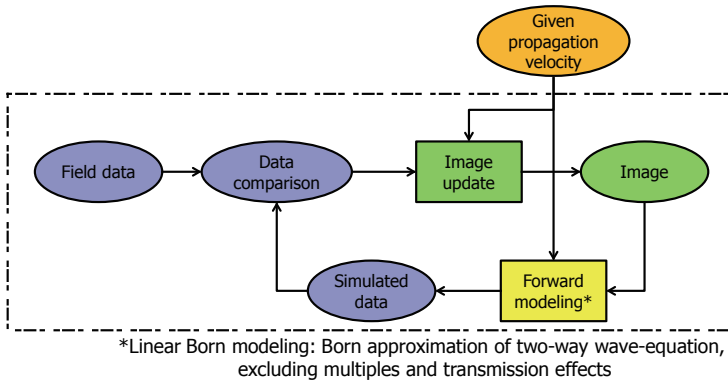
Next, a state-of-the-art imaging method — Least-Squares Reverse-Time Migration (LS-RTM) — and an advanced imaging method — Full Wavefield Migration (FWM) — are reviewed.

1.2.1. LEAST-SQUARES REVERSE-TIME MIGRATION

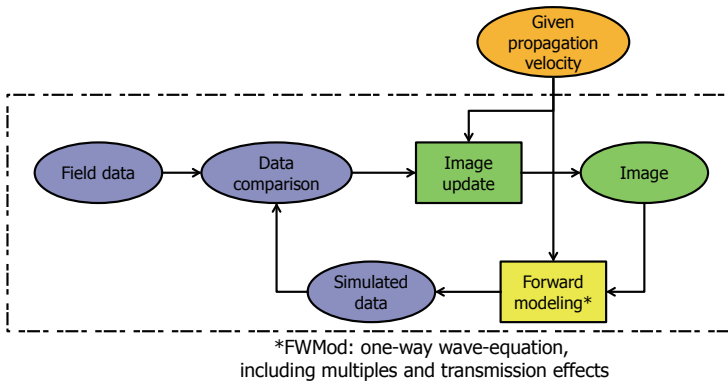
Reverse-Time Migration (RTM) was proposed by [27–29]. The wavefield propagation in RTM is based on a two-way wave-equation and is usually done by using a finite-difference scheme, given a propagation velocity model. After the modeled source wavefields and back-propagated measured wavefields are generated everywhere in the subsurface via forward and backward propagation, a cross-correlation imaging condition is applied to them to extract the images.

[30] combined RTM with a least-squares inversion scheme, compounding the Least-Squares Reverse-Time Migration (LS-RTM) method. In this method, the first step is an RTM process. Next, the data are modeled again from the current image, given the propagation velocity model, by a so-called Born modeling that is based on the linear Born approximation of the two-way wave-equation [31]. The Born approximation ignores both transmission effects and internal multiples in the data. The residual wavefields, which are obtained after a subtraction step between the modeled wavefields and measured wavefields, are gradually minimized in a least-squares sense by updating the image model, etc. The flow chart of LS-RTM is shown in Figure 1.2(a).

This imaging methodology falls into the categories of **pre-stack**, **depth-domain**, **two-way-wave-equation-based**, and **inversion-based**. It inherits the advantages and disadvantages of these categories. It performs well in the case of strong lateral velocity variations, complex velocity profiles or steep dips in the subsurface. Moreover, the inversion improves the image further with less artifacts and better resolution. However, LS-RTM is sensitive to the given velocity model, because the unwanted scatters in the forward- and back-propagated wavefields due to the high contrasts in the velocity model can introduce artifacts in the final image. Regarding the computational efficiency, it demands exponentially high computational effects and memory usage when going upto high frequency.



(a)



(b)

Figure 1.2: The flow charts of LS-RTM (a) and FWM (b).

1.2.2. FULL WAVEFIELD MIGRATION

In order to address these issues in LS-RTM, Full Wavefield Migration (FWM) has been proposed by [32, 33], as a method that honors all multiples and transmission effects properly, without relying on a finite-difference modeling algorithm.

FWM is also an inversion-based approach that explains the measured reflection data in terms of reflectivities. The forward modeling process in FWM, called Full Wavefield Modeling (FWMoD), is based on two separate sets of parameters — reflectivities and propagation velocity, which have orthogonal effects on the modeled data; reflectivities are responsible for the amplitude effects of the data and the propagation velocity is responsible for the kinematic effects of them [34–36]. With this modeling process, from the current estimated image, the seismic reflection responses are generated via one-way wavefield propagation in upward and downward manner. A benefit of using FWMoD is that multiples and transmission effects are explicitly included. Next, the modeled responses are compared to the measured ones and the resulting residual wavefields, which are then back-projected into the parameter space. This back-projection constitutes the gradient calculation of the parameter and a line search procedure. The scale factor for the gradient is defined and the reflectivity model is updated, from which new seismic data are modeled again, yielding the next iteration, etc. In this way, the residual is slowly driven to zero [32, 33, 36]. The flow chart of FWM is shown in Figure 1.2(b).

FWM falls into the categories of **pre-stack**, **depth-domain**, **one-way-wave-equation-based** and **inversion-based**. It also inherits the advantages and disadvantages of these categories. It is cost-effective and able to go up to high frequency easily because finite-difference method is not involved in the wavefield propagation steps. It takes all the multiples and transmission effects into account. Moreover, it is less sensitive to the given velocity model, because the forward and backward wavefield propagation is by definition scattering-free. However, without modifications, it fails to image steep dips [23].

1.3. CONSIDERING VELOCITY VARIATIONS BETWEEN DIFFERENT TIME-LAPSE SURVEYS

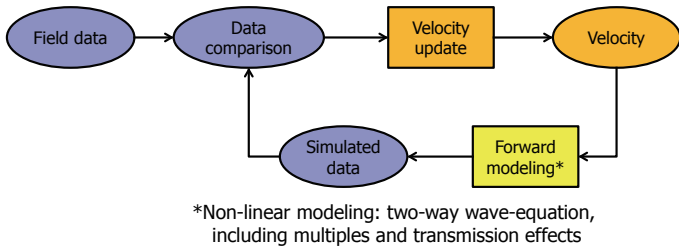
In a typical time-lapse processing workflow, after the imaging process is applied to all the seismic datasets, given the same baseline propagation velocity model, the subtraction between the estimated images is not providing the actual reflection amplitude changes, because the velocity variations of the subsurface between different time-lapse surveys are not taken into account yet. In this section, several strategies, which take care of the velocity variations and result in velocity change indicator, will be reviewed.

1.3.1. TIME-SHIFT MAP

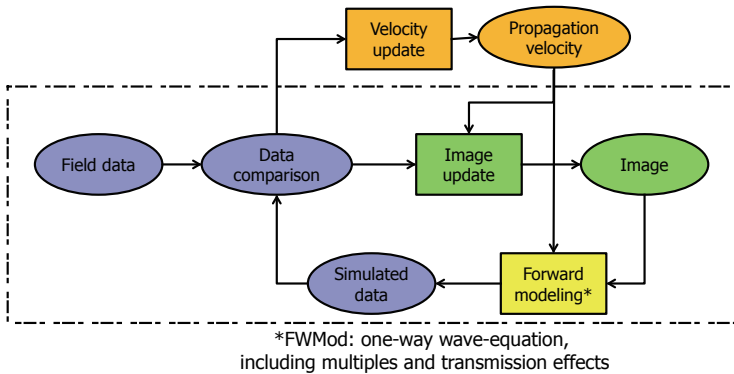
The current time-lapse practice is to first perform an independent imaging process on each dataset based on the same given baseline velocity model. In order to compensate the velocity variations between different time-lapse surveys, a time-shift map is estimated from the baseline and monitor images using a local cross-correlation method along a certain moving time window [6]. Then this time-shift map is applied back to realign the images, yielding the so-called shifted images. The subtraction between the shifted images is providing the final reflection amplitude differences [37–41]. The schematic representation

of this time-shift approach is shown in Figure 1.4.

The outputs of this traditional method are travel-time differences (time-shift maps) and reflection amplitude differences. The time-shift map is only a coarse indicator of the velocity changes. The relative velocity changes derived from a time-shift map are not the actual velocity changes because its estimation is normally under the assumption of a local 1D subsurface (only vertical variations) [38]. Therefore, a better imaging processing strategy that is able to take velocity variations between different surveys into account, is desirable.



(a)



(b)

Figure 1.3: The flow charts of FWI (a) and JMI (b).

1.3.2. FULL WAVEFORM INVERSION

Full waveform inversion (FWI) is a powerful method for providing a quantitative description of the subsurface velocity by iteratively minimizing an objective function that mea-

sures the misfit between measured and modeled data in a least-squares sense [42].

Compared to the imaging method LS-RTM, FWI also solves two-way wave-equation using a finite-difference scheme, however, with a parameterization of the velocity model. Thus, linear Born approximation of the two-way wave-equation is not involved in FWI and internal multiples and transmission effects are in principle properly considered. However, this non-linear two-way modeling makes FWI a non-linear and ill-posed inversion problem and its non-convex objective function may suffer from local minima that are not informative about the true parameters. The local minima corresponds to the cycle-skipping case when the phase match between the modeled and measured data is greater than half a wavelength and will cause erroneous model updates [43, 44]. Moreover, density variations are usually not included, thus, compensated by velocity variations. To partly avoid these issues, FWI is usually only applied to diving waves or to the low-frequency part of the data [45, 46] and starts from a sufficiently good input velocity model. Thus, it cannot easily handle reflections in the data and requires long-offset data to have enough depth penetration as well as very low-frequency components in the data, in order to be less dependent on the starting model [44]. In order to mitigate these issues, [47] suggested a workflow, called reflection FWI, to invert long-wavelength components of the velocity model by using the modeled reflection data generated from images, which are calculated by applying an imaging method to the reflection data. However, it has the problem of using one inversion parameter to explain both the reflection and propagation effects in the data, making the inversion even more nonlinear [48, 49]. Therefore, [50] proposed to reduce this non-linearity by separating the velocity gradients into low-frequency (propagation) and high-frequency (reflection) parts during the inversion. Note that R-FWI is more expensive than the conventional FWI due to the extra step of imaging.

The flow chart of FWI is shown in Figure 1.3(a). One straightforward time-lapse workflow based on FWI is to use FWI as a tool to estimate the velocity models for each vintage sequentially, and then these velocity models are used in a separate imaging process, yielding the final reflection amplitudes. This workflow based on sequential FWI and imaging is shown in Figure 1.5.

1.3.3. JOINT MIGRATION INVERSION

Joint Migration Inversion (JMI) was proposed as one of the methods to overcome the above-mentioned limitations in FWI [33, 48, 49, 51]. JMI uses the same modeling engine as FWM: FWM_{Mod}, which is based on a parameterization in terms of reflectivities and propagation velocity [35]. Unlike FWM, instead of fixing the given propagation velocity model during inversion, JMI updates the propagation velocity as well. Therefore, JMI can be considered as an extended form of FWM, because reflectivity is one of its parameters and it includes automatic velocity updating (see Figure 1.3(b)). It inherits all the advantages and disadvantages of FWM. Moreover, compared to FWI, the scale separation of parameters in JMI makes it more linear and robust to the initial model. Furthermore, because a finite-difference-based algorithm is not involved in JMI, it only needs to follow the Nyquist criterion and does not have to satisfy the Neumann stability condition, therefore, it costs much less computationally when going up to high frequency.

Please note that various ways of combining of FWI and JMI seem to give improved results [52–55]. [53, 54] demonstrated that JMI provides an impressive capability to further

update fine details in the velocity model when using a good initial velocity model, such as the results from FWI. [55] showed that JMI achieves a better reconstruction of the velocity trend in the starting model that sufficiently explains the seismic data for the subsequent FWI.

JMI can be extended to the time-lapse case in a straightforward way by performing independent JMI processes on each dataset, termed as sequential JMI [56, 57]. The schematic representation of time-lapse sequential JMI is shown in Figure 1.6.

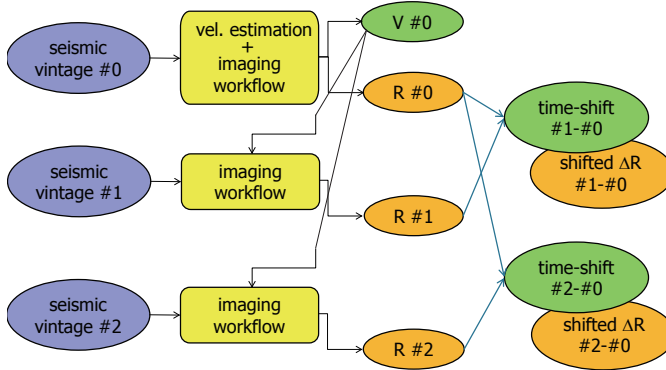


Figure 1.4: Schematic representation of a time-lapse processing method based on a time-shift map.

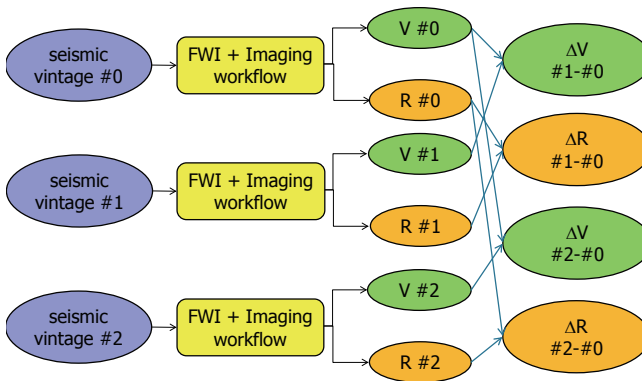


Figure 1.5: Schematic representation of a time-lapse processing method based on sequential FWI.

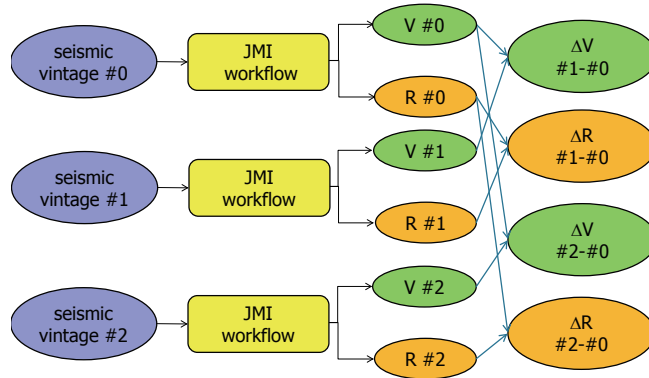


Figure 1.6: Schematic representation of a time-lapse processing method based on sequential JMI.

1.4. SEQUENTIAL VS SIMULTANEOUS STRATEGY

The three workflows mentioned above (Figures 1.4-1.6, i.e. sequential imaging + a time-shift map, sequential FWI + sequential imaging, and sequential JMI) are all based on a straightforward independent processing strategy, also termed as sequential strategy. This strategy is usually sensitive to the differences of noise, acquisition designs, and the uncertainties happening during the process between different datasets. Therefore, the current time-lapse acquisition practice is to exactly repeat well-sampled geometries to mitigate acquisition effects on the final time-lapse differences [58] and the independent processing step also needs to be carefully tailored regarding some various processing "tricks", such as illumination, preconditioning, smoothing of the gradients, etc [59–61]. However, we usually are unable to perfectly reconcile large differences in the acquisitions between different surveys or fully avoid the uncertainty differences in the independent processes. Therefore, a better processing strategy, which is less sensitive to these non-repeatable effects, is a demand.

The time-lapse simultaneous strategy was first proposed by [62]. It processes all the datasets simultaneously and allows the baseline and monitor parameters to communicate and compensate with each other dynamically during inversion via constraints, thus, reducing the non-repeatable uncertainties during time-lapse processing workflow, compared to inverting each dataset independently. [62] proposed to combine this simultaneous strategy with the LS-RTM process. [61, 63, 64] extended this simultaneous strategy to time-lapse FWI. [65, 66] designed a cost-efficient non-repeated time-lapse acquisition, and then proposed to use a simultaneous recovery scheme based on the curvelet transform to recover the 4D vintages.

By combining this simultaneous strategy with the methods mentioned in Section 1.3, we can design the following workflows:

- Simultaneous imaging process + a time-shift map;

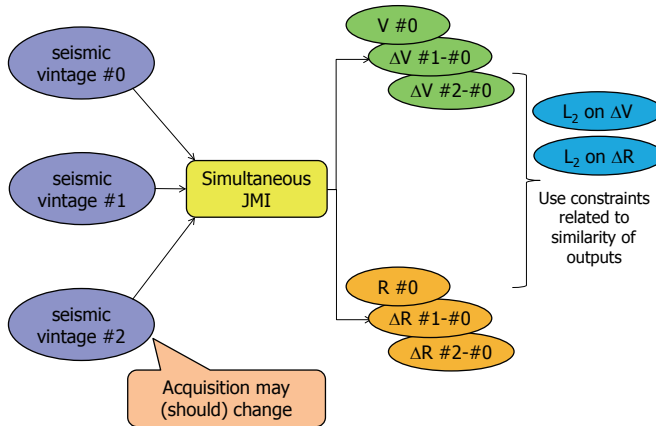


Figure 1.7: Schematic representation of a time-lapse processing method based on simultaneous JMI.

- Simultaneous FWI + simultaneous imaging process;
- Simultaneous JMI.

As was just discussed, a typical time-lapse processing workflow — independent imaging followed by a time-shift map estimation — has two main issues:

- The relative velocity changes derived from a time-shift map are not the actual velocity changes due to the local 1D subsurface assumption;
- This time-lapse workflow requires well-sampled and exactly repeated monitoring surveys, because it is sensitive to the non-repeatable uncertainties caused by monitoring surveys; this requirement for monitoring surveys is costly and makes it not suitable to frequent monitoring.

Therefore, the main research questions which this thesis will cover are as follows:

- Can we utilize a better imaging process that makes use of multiples and at the same time taking velocity variations between monitoring surveys into account?
- Can we propose a better indicator for the velocity changes?
- Is there a better processing or inversion strategy, which is less sensitive to the non-repeatable uncertainties caused by monitoring surveys?
- Do we require the time-lapse acquisition surveys to be well-sampled and exactly repeated?

1.5. THESIS OUTLINE

In this section, an outline of this thesis will be given.

- **Chapter 2:**

This chapter first describes the theoretical details behind FWMoD and JMI. Later on, in a time-lapse scenario, a conventional time-shift-map-based strategy (i.e. a FWM process + a time-shift map estimation) and sequential JMI are demonstrated and compared with a complex synthetic example.

- **Chapter 3:**

This chapter begins with the theory of S-JMI, including L2 constraints on both reflectivity- and velocity-differences via user-defined spatial weighting operators. After that, the theory of high-resolution S-JMI (HR-S-JMI) is introduced, including two extra constraints: directional total variation regularization on velocities and a time-lapse reflectivity-difference constraint, which makes a link between reflectivity- and velocity-difference by constraining the relationship between them. Finally, the effectiveness of regular S-JMI and HR-S-JMI is demonstrated based on a complex synthetic example.

- **Chapter 4:**

In this chapter, we further demonstrate the effectiveness of HR-S-JMI as a tool for reservoir monitoring with a highly realistic synthetic model based on the Grane field, offshore Norway, and a time-lapse field dataset from the Troll Field. In the Grane field numerical example, we first investigate whether various time-lapse effects in this model, i.e. the reservoir time-lapse changes, the effects due to injection in the overburden, the weak stress-induced effects over the reservoir, and small water velocity perturbation, can be detected with S-JMI. Then, we compare the inverted results using S-JMI with those using a conventional time-lapse method based on creating time-shift maps and results from a sequential strategy based on JMI. Furthermore, we show that HR-S-JMI results in a more localized time-lapse velocity update when there are not enough strong reflections around the target area helping the inversion of the velocity in regular S-JMI. In the end, with one field data example based on marine time-lapse data from the Troll Field, we show the feasibility of the proposed method in a real case where the repeatability of the time-lapse datasets is not very good.

- **Chapter 5:**

In this chapter, we investigate the feasibility of using HR-S-JMI in practice, some numerical experiments are conducted to test the dependence of HR-S-JMI on the quality of the time-lapse datasets including the following aspects: non-repeated noise, including random noise and coherent noise; the quality of time-lapse surveys, including sparse surveys, non-repeated surveys, and Ocean Bottom Node (OBN) vs Streamer (sparse and non-repeated time-lapse surveys); the quality of sources, including source positioning error and non-repeated source wavelet. Moreover, its robustness to the spatial weighting operators in L2-norm constraints and sensitivity to weak time-lapse effects are also tested.

- **Chapter 6:**

This chapter begins with a review of a semi-continuous monitoring technology: i4D

seismic monitoring, where monitor surveys are much more sparsely sampled compared to the baseline survey. After that, we introduce the theory of S-JMI with extra calendar-time constraints, which take advantage of the feature that time-lapse effects change (semi-)continuously along the calendar-time axis during (semi-)continuous monitoring. In the end, with one complex synthetic example, we demonstrate that S-JMI is an effective tool to process datasets acquired from the semi-continuous monitoring surveys, which are designed according to the i4D technology. We also show that the proposed calendar-time constraints significantly improve the quality of the time-lapse results. In addition, we compare the time-lapse results assuming all the monitoring datasets are available to those results where only the datasets up to the current one are used.

- **Chapter 7:**

This chapter describes the main conclusions of this thesis, followed by some recommendations for further research.

Please note that Chapter 3 and 4 are an extended version of work published in [67–73]. Chapter 6 is an extended version of work published in [74]. Appendix B is an extended version of work published in [75].

REFERENCES

- [1] K. Koster, P. Gabriels, M. Hartung, J. Verbeek, G. Deinum, and R. Staples, *Time-lapse seismic surveys in the North Sea and their business impact*, *The Leading Edge* **19** (2000), pp. 286–293.
- [2] D. E. Lumley, *Time-lapse seismic reservoir monitoring*, *Geophysics* **66** (2001), pp. 50–53.
- [3] D. Johnston, *Time-lapse 4D technology: Reservoir surveillance*, *AAPG Search and Discovery* (2005).
- [4] C. MacBeth, M.-D. Mangriotis, and H. Amini, *Post-stack 4D seismic time-shifts: Interpretation and evaluation*, *Geophysical Prospecting* **67** (2019), pp. 3–31.
- [5] R. Calvert, *4D technology: Where are we, and where are we going?* *Geophysical Prospecting* **53** (2005), pp. 161–171.
- [6] P. Hatchell and S. Bourne, *Rocks under strain: Strain-induced time-lapse time shifts are observed for depleting reservoirs*, *The Leading Edge* **24** (2005), pp. 1222–1225.
- [7] P. Haffinger, F. J. Eyvazi, P. Doulgeris, P. Steeghs, D. Gisolf, and E. Verschuur, *Quantitative prediction of injected CO₂ at sleipner using wave-equation based AVO*, *First Break* **35** (2017), pp. 65–70.
- [8] M. Batzle and Z. Wang, *Seismic properties of pore fluids*, *Geophysics* **57** (1992), pp. 1396–1408.

- [9] M. Dadashpour, M. Landrø, and J. Kleppe, *Nonlinear inversion for estimating reservoir parameters from time-lapse seismic data*, *Journal of Geophysics and Engineering* **5** (2007), p. 54.
- [10] Ö. Yilmaz, *Seismic data analysis: Processing, inversion, and interpretation of seismic data* (Society of exploration geophysicists, 2001).
- [11] S. H. Bickel, *Velocity-depth ambiguity of reflection traveltimes*, *Geophysics* **55** (1990), pp. 266–276.
- [12] J. Etgen, S. H. Gray, and Y. Zhang, *An overview of depth imaging in exploration geophysics*, *Geophysics* **74** (2009), pp. WCA5–WCA17.
- [13] W. S. French, *Computer migration of oblique seismic reflection profiles*, *Geophysics* **40** (1975), pp. 961–980.
- [14] W. A. Schneider, *Integral formulation for migration in two and three dimensions*, *Geophysics* **43** (1978), pp. 49–76.
- [15] S. H. Gray, J. Etgen, J. Dellinger, and D. Whitmore, *Seismic migration problems and solutions*, *Geophysics* **66** (2001), pp. 1622–1640.
- [16] J. F. Claerbout, *Toward a unified theory of reflector mapping*, *Geophysics* **36** (1971), pp. 467–481.
- [17] J. F. Claerbout and S. M. Doherty, *Downward continuation of moveout-corrected seismograms*, *Geophysics* **37** (1972), pp. 741–768.
- [18] J. Gazdag, *Wave equation migration with the phase-shift method*, *Geophysics* **43** (1978), pp. 1342–1351.
- [19] A. J. Berkhout, *Seismic migration, imaging of acoustic energy by wave field extrapolation, A: theoretical aspects* (Elsevier (second edition), 1982).
- [20] C. P. A. Wapenaar and A. J. Berkhout, *Elastic wave field extrapolation: redatuming of single- and multi-component seismic data* (Elsevier Science Publ. Co., Inc., 1989).
- [21] G. Shan, L. Zhang, Y. Wang, T. Nemeth, and W. Liu, *Velocity sensitivity of reverse-time migration*, in *SEG Technical Program Expanded Abstracts 2008* (Society of Exploration Geophysicists, 2008) pp. 2321–2325.
- [22] X. Jia and R.-S. Wu, *Superwide-angle one-way wave propagator and its application in imaging steep salt flanks*, *Geophysics* **74** (2009), pp. S75–S83.
- [23] M. Davydenko, D. Verschuur, and A. Berkhout, *Omnidirectional extension of full wavefield migration*, in *76th EAGE Conference and Exhibition 2014* (2014).
- [24] W. A. Mulder and R.-E. Plessix, *A comparison between one-way and two-way wave-equation migration*, *Geophysics* **69** (2004), pp. 1491–1504.

- [25] G. T. Schuster, *Least-squares cross-well migration*, in *SEG Technical Program Expanded Abstracts 1993* (Society of Exploration Geophysicists, 1993) pp. 110–113.
- [26] T. Nemeth, C. Wu, and G. T. Schuster, *Least-squares migration of incomplete reflection data*, *Geophysics* **64** (1999), pp. 208–221.
- [27] E. Baysal, D. D. Kosloff, and J. W. Sherwood, *Reverse time migration*, *Geophysics* **48** (1983), pp. 1514–1524.
- [28] G. A. McMechan, *Migration by extrapolation of time-dependent boundary values*, *Geophysical Prospecting* **31** (1983), pp. 413–420.
- [29] N. D. Whitmore, *Iterative depth migration by backward time propagation*, in *SEG Technical Program Expanded Abstracts 1983* (Society of Exploration Geophysicists, 1983) pp. 382–385.
- [30] W. Dai, P. Fowler, and G. T. Schuster, *Multi-source least-squares reverse time migration*, *Geophysical Prospecting* **60** (2012), pp. 681–695.
- [31] H. H. Jaramillo and N. Bleistein, *The link of Kirchhoff migration and demigration to Kirchhoff and Born modeling*, *Geophysics* **64** (1999), pp. 1793–1805.
- [32] A. J. Berkhout and D. J. Verschuur, *Full wavefield migration, utilizing surface and internal multiple scattering*, in *SEG Technical Program Expanded Abstracts 2011* (Society of Exploration Geophysicists, 2011) pp. 3212–3216.
- [33] A. J. Berkhout, *Review paper: An outlook on the future of seismic imaging, Part II: Full-wavefield migration*, *Geophysical Prospecting* **62** (2014), pp. 931–949.
- [34] A. J. Berkhout, *Combining full wavefield migration and full waveform inversion, a glance into the future of seismic imaging*, *Geophysics* **77** (2012), pp. S43–S50.
- [35] A. J. Berkhout, *Review paper: An outlook on the future of seismic imaging, Part I: forward and reverse modelling*, *Geophysical Prospecting* **62** (2014), pp. 911–930.
- [36] M. Davydenko and D. J. Verschuur, *Full-wavefield migration: using surface and internal multiples in imaging*, *Geophysical Prospecting* **65** (2017), pp. 7–21.
- [37] R. Arts, R. Elsayed, L. Van Der Meer, O. Eiken, S. Ostmo, A. Chadwick, G. Kirby, and B. Zinszner, *Estimation of the mass of injected CO₂ at Sleipner using time-lapse seismic data*, in *64th EAGE Conference & Exhibition* (2002).
- [38] R. Arts, O. Eiken, A. Chadwick, P. Zweigel, L. Van der Meer, and B. Zinszner, *Monitoring of CO₂ injected at Sleipner using time-lapse seismic data*, *Energy* **29** (2004), pp. 1383–1392.
- [39] A. Tura, T. Barker, P. Cattermole, C. Collins, J. Davis, P. Hatchell, K. Koster, P. Schutjens, and P. Wills, *Monitoring primary depletion reservoirs using amplitudes and time shifts from high-repeat seismic surveys*, *The Leading Edge* **24** (2005), pp. 1214–1221.

- [40] M. Trani, R. Arts, O. Leeuwenburgh, and J. Brouwer, *Estimation of changes in saturation and pressure from 4D seismic AVO and time-shift analysis*, *Geophysics* **76** (2011), pp. C1–C17.
- [41] P. Routh, G. Palacharla, I. Chikichev, and S. Lazaratos, *Full wavefield inversion of time-lapse data for improved imaging and reservoir characterization*, in *SEG Technical Program Expanded Abstracts 2012* (Society of Exploration Geophysicists, 2012) pp. 1–6.
- [42] A. Tarantola, *Inversion of seismic reflection data in the acoustic approximation*, *Geophysics* **49** (1984), pp. 1259–1266.
- [43] W. W. Symes, *Migration velocity analysis and waveform inversion*, *Geophysical prospecting* **56** (2008), pp. 765–790.
- [44] J. Virieux and S. Operto, *An overview of full-waveform inversion in exploration geophysics*, *Geophysics* **74** (2009), pp. WCC127 – WCC152.
- [45] S. Operto, C. Ravaut, L. Imbrota, J. Virieux, A. Herrero, and P. Dell’Aversana, *Quantitative imaging of complex structures from dense wide-aperture seismic data by multi-scale traveltime and waveform inversions: A case study*, *Geophysical prospecting* **52** (2004), pp. 625–651.
- [46] R.-E. Plessix, G. Baeten, J. W. de Maag, M. Klaassen, Z. Rujie, and T. Zhifei, *Application of acoustic full waveform inversion to a low-frequency large-offset land data set*, in *SEG Technical Program Expanded Abstracts 2010* (Society of Exploration Geophysicists, 2010) pp. 930–934.
- [47] S. Xu, D. Wang, F. Chen, Y. Zhang, and G. Lambare, *Full waveform inversion for reflected seismic data*, in *74th EAGE Conference and Exhibition incorporating EUROPEC 2012* (2012).
- [48] A. J. Berkhout, *Review paper: An outlook on the future of seismic imaging, Part III: Joint migration inversion*, *Geophysical Prospecting* **62** (2014), pp. 950–971.
- [49] D. J. Verschuur, X. R. Staal, and A. J. Berkhout, *Joint migration inversion: Simultaneous determination of velocity fields and depth images using all orders of scattering*, *The Leading Edge* **35** (2016), pp. 1037–1046.
- [50] Z. Wu and T. Alkhalifah, *Simultaneous inversion of the background velocity and the perturbation in full-waveform inversion*, *Geophysics* **80** (2015), pp. R317–R329.
- [51] X. R. Staal, *Combined imaging and velocity estimation by Joint Migration Inversion*, *Ph.D. thesis*, Delft University of Technology (2015).
- [52] M. Davydenko and D. J. Verschuur, *Full-wavefield estimation of angle-dependent reflectivity and migration velocity*, in *SEG Technical Program Expanded Abstracts 2017* (Society of Exploration Geophysicists, 2017) pp. 5631–5635.

- [53] Y. Sun, Y. Kim, S. Qu, D. Verschuur, A. Almomin, and R. van Borselen, *Joint migration inversion versus fwi-rtm—a comparison study on a 2d realistic deep water model*, in *80th EAGE Conference and Exhibition 2018* (2018).
- [54] Y. Sun, Y. S. Kim, S. Qu, E. Verschuur, A. Almomin, and R. van Borselen, *Angle-dependent full wavefield migration based upon full waveform inversion and joint migration inversion*, in *SEG Technical Program Expanded Abstracts 2018* (Society of Exploration Geophysicists, 2018) pp. 4357–4361.
- [55] G. Eisenberg, E. Schuenemann, G. Gierse, E. Verschuur, and S. Qu, *Robust velocity estimation via joint migration inversion and full waveform inversion*, in *SEG Technical Program Expanded Abstracts 2019* (Society of Exploration Geophysicists, 2019) pp. 1224–1228.
- [56] D. Verschuur and X. Staal, *Using primaries and multiples in time-lapse imaging and velocity estimation*, in *SEG Technical Program Expanded Abstracts 2014* (Society of Exploration Geophysicists, 2014) pp. 4955–4959.
- [57] D. J. Verschuur, *Time-lapse imaging for a strongly scattering overburden via joint-migration inversion*, in *77th EAGE Conference and Exhibition 2015* (Eur. Ass. of Geosc. and Eng., Expanded abstracts, 2015).
- [58] F. Smit, J. Brain, and K. Watt, *Repeatability monitoring during marine 4D streamer acquisition*, in *67th EAGE Conference and Exhibition 2016* (Eur. Ass. of Geosc. and Eng., Expanded abstracts, 2005).
- [59] T. Watanabe, S. Shimizu, E. Asakawa, and T. Matsuoka, *Differential waveform tomography for time-lapse crosswell seismic data with application to gas hydrate production monitoring*, in *SEG Technical Program Expanded Abstracts 2004* (Society of Exploration Geophysicists, 2004) pp. 2323–2326.
- [60] D. Yang, M. Meadows, P. Inderwiesen, J. Landa, A. Malcolm, and M. Fehler, *Double-difference waveform inversion: Feasibility and robustness study with pressure data*, *Geophysics* **80** (2015), pp. M129–M141.
- [61] M. Maharramov, B. Biondi, and M. A. Meadows, *Time-lapse inverse theory with applications*, *Geophysics* **81** (2016), pp. R485–R501.
- [62] G. Ayeni and B. Biondi, *Target-oriented joint least-squares migration/inversion of time-lapse seismic data sets*, *Geophysics* **75** (2010), pp. R61–R73.
- [63] M. Maharramov and B. Biondi, *Joint full-waveform inversion of time-lapse seismic data sets*, in *SEG Technical Program Expanded Abstracts 2014* (Society of Exploration Geophysicists, 2014) pp. 954–959.
- [64] M. Maharramov and B. Biondi, *Robust simultaneous time-lapse full-waveform inversion with total-variation regularization of model difference*, in *77th EAGE Conference and Exhibition 2016* (Eur. Ass. of Geosc. and Eng., Expanded abstracts, 2015).

- [65] F. Oghenekohwo, H. Wason, E. Esser, and F. J. Herrmann, *Low-cost time-lapse seismic with distributed compressive sensing—part 1: Exploiting common information among the vintages*, *Geophysics* **82** (2017), pp. P1–P13.
- [66] H. Wason, F. Oghenekohwo, and F. J. Herrmann, *Low-cost time-lapse seismic with distributed compressive sensing—part 2: Impact on repeatability*, *Geophysics* **82** (2017), pp. P15–P30.
- [67] S. Qu and D. J. Verschuur, *Simultaneous time-lapse imaging via joint migration and inversion*, in *78th EAGE Conference and Exhibition 2016* (Eur. Ass. of Geosc. and Eng., Expanded abstracts, 2016).
- [68] S. Qu and D. J. Verschuur, *Getting accurate time-lapse information using geology-constrained simultaneous joint migration-inversion*, in *SEG Technical Program Expanded Abstracts 2016* (Society of Exploration Geophysicists, 2016) pp. 5451–5456.
- [69] S. Qu and D. J. Verschuur, *Simultaneous joint migration inversion for accurate time-lapse analysis of sparse monitor surveys*, in *First EAGE Workshop on Practical Reservoir Monitoring* (Eur. Ass. of Geosc. and Eng., Expanded abstracts, 2017).
- [70] S. Qu and D. J. Verschuur, *Time-lapse simultaneous joint migration inversion applied to realistic synthetic data based on Grane field*, in *80th EAGE Conference and Exhibition 2018* (Eur. Ass. of Geosc. and Eng., Expanded abstracts, 2018).
- [71] S. Qu and D. J. Verschuur, *Time-lapse simultaneous joint migration inversion for high-resolution imaging/inversion based on a realistic synthetic model from the Grane field*, in *SEG Technical Program Expanded Abstracts 2018* (Society of Exploration Geophysicists, 2018) pp. 5362–5366.
- [72] S. Qu and D. J. Verschuur, *A robust high-resolution time-lapse simultaneous joint migration inversion process applied to synthetic data from grane field*, in *81th EAGE Conference and Exhibition 2019* (Eur. Ass. of Geosc. and Eng., Expanded abstracts, 2019).
- [73] S. Qu and D. J. Verschuur, *A robust high-resolution time-lapse simultaneous joint migration inversion process applied to the time-lapse Troll field datasets*, in *Second EAGE Workshop on Practical Reservoir Monitoring* (Eur. Ass. of Geosc. and Eng., Expanded abstracts, 2019).
- [74] S. Qu and D. Verschuur, *Simultaneous joint migration inversion for semicontinuous time-lapse seismic data*, in *SEG Technical Program Expanded Abstracts 2017* (Society of Exploration Geophysicists, 2017) pp. 5808–5813.
- [75] S. Qu, E. Verschuur, and Y. Chen, *Full waveform inversion and joint migration inversion with an automatic directional total variation constraint*, *Geophysics* **84** (2018), pp. 1–37.

2

SEQUENTIAL JOINT MIGRATION INVERSION

The current time-lapse practice is to first remove all multiples from the data, and then perform an independent imaging process on each dataset based on the same estimated baseline velocity model. In order to compensate the velocity variations of the subsurface between different surveys, a time-shift-map-based method is applied to realign the images.

However, in practice, we usually are unable to remove all multiples from the datasets completely in the first step. Moreover, the time-shift-map tool is normally under the assumption of a local 1D subsurface (only vertical variations), thus, the relative velocity changes derived from the time-shift map are not the actual velocity changes. Therefore, a better imaging process, which is able to make use of multiples and at the same time take velocity variations between surveys into account, is desirable.

We propose to use the inversion-based Joint Migration Inversion (JMI) method as an effective time-lapse processing tool for reservoir monitoring. JMI is a full wavefield inversion method that explains the measured reflection data using a parameterization in terms of reflectivity and propagation velocity. Transmission effects and internal multiples are included in the forward modeling process of JMI, which is termed Full Wavefield Modeling (FWM), based on a multi-dimensional version of the Bremmer series. Since reflectivity is one of the inversion parameters of JMI and velocity only describes the wave propagation effects, JMI can also be considered as an extended form of least-squares imaging, although it includes all the multiple scattering and transmission effects, and also employs automatic velocity updating. We apply JMI in the time-lapse case by conducting JMI for the baseline and monitor datasets independently, termed as sequential JMI. The differences of the resulting models make the final time-lapse changes. Finally, we demonstrate the effectiveness of sequential JMI with a complex synthetic example based on the Marmousi model, compared to the conventional time-shift-map-based method, i.e. a FWM process + a time-shift map estimation.

2.1. INTRODUCTION

After the baseline and subsequent monitoring surveys are acquired, the time-lapse changes in the seismic parameters between different surveys are estimated by processing all the datasets. As was discussed earlier, the most conventional processing workflow is to first remove all multiples from the data, and then perform an independent imaging process on each dataset based on the same baseline propagation velocity model. However, the true velocity model usually varies from survey to survey, yielding misalignments in the calculated images, which need to be further processed using a time-shift-map-based tool [1–5]. The schematic representation of this conventional approach was already shown in Figure 1.4. In practice, we usually are unable to remove all multiples from the datasets completely in the first step and the time-shift-map-based tool operates normally under the assumption of a local 1D subsurface (only vertical variations) [2]. Therefore, one important question arises here: "Can we address a better imaging process that makes use of multiples, and at the same time taking velocity differences between different surveys into account?"

Least-squares migration (LSM) and full-waveform inversion (FWI) are two popular time-lapse processing methods [5–7]. However, because of the strong non-linearity of FWI, related to the inversion parameters velocity and (poorly resolved) density, this may not be the best engine for time-lapse analysis. Ignoring non-linear propagation effects (i.e. multiples and transmission effects) means that LSM will not optimally perform in situations with large contrasts. More details about FWI and LSM were already discussed in Section 1.2 and 1.3. Therefore, we propose to employ the inversion-based Joint Migration Inversion (JMI) method, as proposed as one of the methods to overcome the above mentioned limitations in FWI and LSM [8–12].

The main engine of JMI is a forward modeling process called Full Wavefield Modeling (FWMod), which is based on a parameterization in term of reflectivity and propagation velocity [13]. Note that based on this parameterization, density variations are implicitly included in the reflectivity. The aim of JMI is to match the modeled data with the measured data sample by sample. Therefore, JMI can be called a full-waveform inversion process. JMI can also be considered as an extended form of least-squares imaging [14], because reflectivity is one of its parameter, although it includes all the multiple scattering and transmission effects, as well as automatic velocity updating. JMI can be extended to the time-lapse case by performing independent JMI on each dataset, termed as sequential JMI [15, 16]. The schematic representation of time-lapse sequential JMI was already shown in Figure 1.6.

This chapter is organized as follows: we first describe the theoretical details behind FWMod and JMI. Please note that the FWMod/JMI process is done in the frequency-space domain. Therefore, in order to simplify the derivations of FWMod and gradients of JMI, we consider one frequency slice and one shot, which are all orthogonal to each other. It will be easy to extend this theory to the full frequency and full shots case. The FWMod/JMI theory is described in 2D here, but can be extended to 3D [17]. Moreover, only P-P reflections are considered in this work. Finally, in the time-lapse scenario, we demonstrate this time-lapse approach with a complex synthetic example, compared to the conventional time-shift-map-based method (i.e. a FWM process + a time-shift map estimation).

2.2. FULL WAVEFIELD MODELING

In FWMod, the model space (x, z) is divided into a fine set of depth levels $z_m, m = 0, \dots, N_z - 1$ separated by a small distance Δz along a certain spatial direction $z - axis$, which are so-called building blocks. For each building block, parameters (reflectivity and propagation velocity) are defined and wavefields are calculated. One building block used in FWMod is shown in Figure 2.1. It consists of two parts: (1) reflection and transmission at each level and (2) propagation in-between two conjunctive levels. Four wavefields are calculated at each depth level relative to the $z - axis$ direction: the down-going incoming wavefield $\mathbf{p}^+(z_m)$, the up-going incoming wavefield $\mathbf{p}^-(z_m)$, the down-going outgoing wavefield $\mathbf{q}^+(z_m)$, the up-going outgoing wavefield $\mathbf{q}^-(z_m)$. In addition, two source wavefields — down-going source wavefield $\mathbf{s}^+(z_m)$ and up-going source wavefield $\mathbf{s}^-(z_m)$ — are added at each depth level. Note that, for one depth level, the dimension of the monochromatic wavefields $(\mathbf{p}^\pm(z_m), \mathbf{q}^\pm(z_m), \mathbf{s}^\pm(z_m))$ is $(N_x \times 1)$ denoting the size of the $x - axis$ in the solution space. All the wavefields are illustrated in Figure 2.1(a).

2.2.1. REFLECTION AND TRANSMISSION AT EACH LEVEL

At the depth level z_m , reflection is described via upwards and downwards reflectivity operators $\mathbf{R}^U(z_m)$ and $\mathbf{R}^\cap(z_m)$, respectively; and transmission is described via down- and up-going transmission operators $\mathbf{T}^+(z_m)$ and $\mathbf{T}^-(z_m)$, respectively. All the operators are also illustrated in Figure 2.1(b). For one depth level, the reflectivity and transmission operators $(\mathbf{R}^{U/\cap}(z_m), \mathbf{T}^\pm(z_m))$ are matrices with the dimension of $(N_x \times N_x)$. The wavefields are connected by reflectivity and transmission effects (see also [13, 18, 19]):

$$\begin{aligned}\mathbf{q}^+(z_m) &= \mathbf{s}^+(z_m) + \mathbf{T}^+(z_m)\mathbf{p}^+(z_m) + \mathbf{R}^U(z_m)\mathbf{p}^-(z_m), \\ \mathbf{q}^-(z_m) &= \mathbf{s}^-(z_m) + \mathbf{T}^-(z_m)\mathbf{p}^-(z_m) + \mathbf{R}^\cap(z_m)\mathbf{p}^+(z_m).\end{aligned}\quad (2.1)$$

The transmission operator $\mathbf{T}^\pm(z_m)$ can be further written as follows:

$$\mathbf{T}^\pm(z_m) = \mathbf{I} + \delta\mathbf{T}^\pm(z_m), \quad (2.2)$$

where \mathbf{I} is a unit matrix sharing the same size as the other operators and $\delta\mathbf{T}^\pm(z_m)$ is the differential transmission in the down/up directions [13].

Furthermore, in the situations where wave conversion can be neglected (like the acoustic case), we have

$$\begin{aligned}\mathbf{R}^\cap(z_m) &= -\mathbf{R}^U(z_m), \\ \delta\mathbf{T}^+(z_m) &= \mathbf{R}^U(z_m), \\ \delta\mathbf{T}^-(z_m) &= \mathbf{R}^\cap(z_m).\end{aligned}\quad (2.3)$$

Therefore, three unknowns are eliminated in equation 2.1. We further simplify $\mathbf{R}^U(z_m)$ as $\mathbf{R}(z_m)$ yielding:

$$\begin{aligned}\mathbf{q}^+(z_m) &= \mathbf{s}^+(z_m) + (\mathbf{I} + \mathbf{R}(z_m))\mathbf{p}^+(z_m) + \mathbf{R}(z_m)\mathbf{p}^-(z_m), \\ \mathbf{q}^-(z_m) &= \mathbf{s}^-(z_m) + (\mathbf{I} - \mathbf{R}(z_m))\mathbf{p}^-(z_m) - \mathbf{R}(z_m)\mathbf{p}^+(z_m).\end{aligned}\quad (2.4)$$

Note that the reflectivity operator $\mathbf{R}(z_m)$ is supposed to be an angle-dependent parameter [11, 18], which means it is a function of incident angle of the waves and leads to a large solution space, therefore puts the inversion into the danger of over-parameterization. Thus,

in this work, we make an assumption of a scalar reflectivity operator by ignoring the influences of incident angles and using the diagonal values $\mathbf{r}(z_m) = \text{diag}(\mathbf{R}(z_m))$ at each depth level (see Appendix A).

2

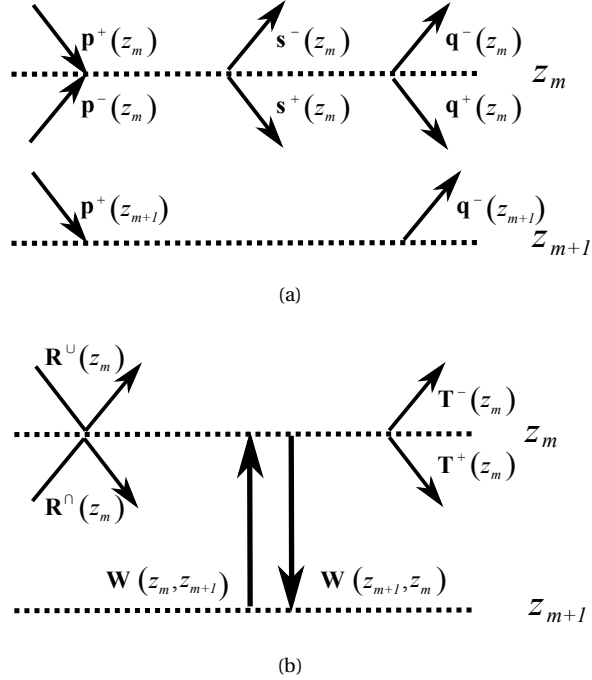


Figure 2.1: The fundamental building block of FWMod: schematic illustration of (a) the modeled wavefields and source wavefields; (b) reflectivity, transmission and propagation operators.

2.2.2. PROPAGATION IN-BETWEEN TWO CONSECUTIVE LEVELS

In-between the z_m and z_{m+1} levels, the propagation of wavefields are described via down- and up-going propagation operators $\mathbf{W}(z_{m+1}, z_m)$ and $\mathbf{W}(z_m, z_{m+1})$. The four wavefields of two consecutive levels are connected by propagation operators (see also [13, 18, 19]):

$$\begin{aligned} \mathbf{p}^+(z_{m+1}) &= \mathbf{W}(z_{m+1}, z_m) \mathbf{q}^+(z_m), \\ \mathbf{p}^-(z_m) &= \mathbf{W}(z_m, z_{m+1}) \mathbf{q}^-(z_{m+1}). \end{aligned} \quad (2.5)$$

We build the propagation operators in the frequency-wavenumber domain first and then transform it back to the frequency-space domain. Within one layer, the dimension of the propagation operators is $(N_x \times N_x)$. By assuming the medium in between each two consecutive levels is locally homogeneous, we can relate i^{th} row of the propagation operator $\mathbf{W}(z_{m+1}, z_m)$ to a phase-shift operator [20] propagating the wavefields from one depth

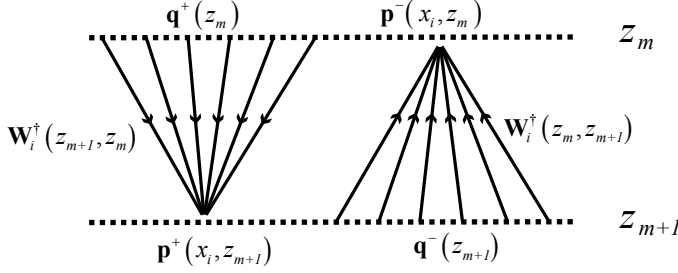


Figure 2.2: Schematic illustration of the i^{th} row of propagation operator $\mathbf{W}(z_{m+1}, z_m)$: $\mathbf{w}_i^\dagger(z_{m+1}, z_m)$ and $\mathbf{w}_i^\dagger(z_m, z_{m+1})$ in equation 2.6.

level z_m to one point at the next depth level (x_i, z_{m+1}) (illustrated in Figure 2.2):

$$\begin{aligned} \mathbf{w}_i^\dagger(z_{m+1}, z_m) &= \mathcal{F}_x^{-1} \left[e^{-jk_z \Delta z} e^{jk_x x_i} \right], \\ k_z &= \begin{cases} \sqrt{k^2 - k_x^2} & |k_x| \leq |k| \\ -j\sqrt{k_x^2 - k^2} & |k_x| > |k|, \end{cases} \\ k &= \frac{\omega}{v_i(z_{m+1}, z_m)}, \end{aligned} \quad (2.6)$$

where $\mathbf{w}_i^\dagger(z_{m+1}, z_m)$ denotes the i^{th} row of $\mathbf{W}(z_{m+1}, z_m)$. \mathcal{F}_x^{-1} is the inverse Fourier transform from the (k_x, z) domain to the (x, z) domain. "j" is the imaginary unit and $v_i(z_{m+1}, z_m)$ is a scalar, representing the propagation velocity at lateral location x_i in between z_m and z_{m+1} levels.

As we can see from equation 2.6, the propagation velocity is implicitly embedded in the propagation operator. Numerically, we define v_i to the grids of the solution space for simplicity as follows:

$$\begin{aligned} v_i(z_{m+1}, z_m) &\equiv v_i(z_m), \\ v_i(z_m, z_{m+1}) &\equiv v_i(z_m). \end{aligned} \quad (2.7)$$

Based on the definition equation 2.7, the propagation operators between two consecutive levels have the following simplified relationship.

$$\mathbf{W}(z_{m+1}, z_m) \equiv \mathbf{W}(z_m, z_{m+1}). \quad (2.8)$$

2.2.3. RECURSIVE MODELING SCHEME

The above describes the basic building blocks of FWMod, which is formulated by equation 2.4 and 2.5. Based on the current reflectivity values \mathbf{r} and propagation velocity distribution \mathbf{v} , by extrapolating the four wavefields (\mathbf{p}^\pm and \mathbf{q}^\pm) downwards from z_0 to z_{N_z-1} and then upwards from z_{N_z-1} to z_0 with these building blocks, one round-trip of modeling is constructed, yielding only primaries. Subsequently, based on the updated four wavefields, next round-trip of modeling is constructed, then the first order of internal multiples is included. Transmission effects are automatically included as well. By recursively applying

these building blocks, contributions from more orders of multiples are taken into account, thereby making the four wavefields more complete. Note that such a recursive modeling scheme can be treated as a generalization of the so-called Bremmer series [21, 22].

2

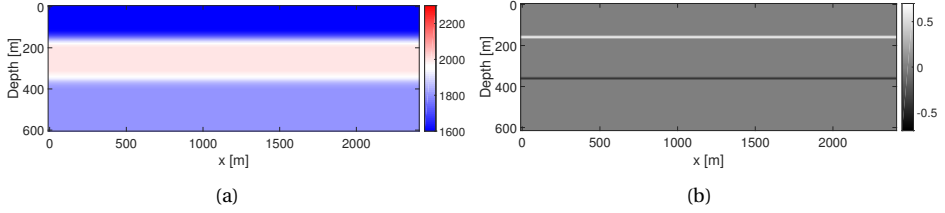


Figure 2.3: Numerical example: (a) and (b) the true velocity and reflectivity model.

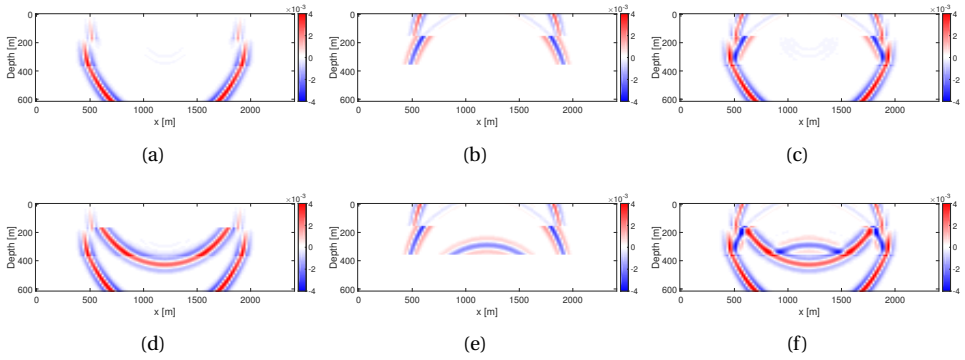


Figure 2.4: Numerical example based on the model in Figure 2.3: snapshots at 0.44s: the first round-trip of modeling yielding only primaries: (a) downwards from z_0 to z_{N_z-1} (\mathbf{p}^+), (b) upwards from z_{N_z-1} to z_0 (\mathbf{p}^-) and (c) their summation ($\mathbf{p}^+ + \mathbf{p}^-$); the second round-trip modeling yielding primaries and the first order of internal multiples: (d) downwards from z_0 to z_{N_z-1} (\mathbf{p}^+), (e) upwards from z_{N_z-1} to z_0 (\mathbf{p}^-) and (f) their summation ($\mathbf{p}^+ + \mathbf{p}^-$).

Furthermore, FWMod based on these building blocks is quite flexible and can be easily extended to include more physics by upgrading the building block. For example, by reformulating the propagation operator \mathbf{W} , anisotropy [23] or Q-effects [24] can be taken into account. Moreover, the reflectivity operator \mathbf{R} is fully data-driven and able to explain the elastic amplitudes (if non-diagonal elements in \mathbf{R} are included) without explicitly imposing an elastic wave-equation [25].

2.2.4. NUMERICAL DEMONSTRATION

In this subsection, based on a simple 1.5 D model shown in Figure 2.3, one numerical example will be demonstrated to visualize the process of FWMod.

With the velocity and reflectivity models in Figure 2.3 as the parameters, FWMod is implemented recursively based on the basic building blocks described by equation 2.4

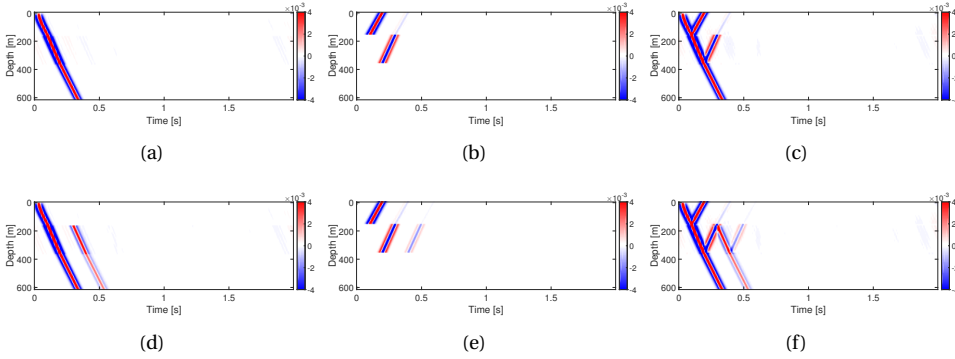


Figure 2.5: Numerical example based on the model in Figure 2.3: pseudo VSP cross-section at 1600m: the first round-trip of modeling yielding only primaries: (a) downwards from z_0 to z_{N_z-1} (\mathbf{p}^+), (b) upwards from z_{N_z-1} to z_0 (\mathbf{p}^-) and (c) their summation ($\mathbf{p}^+ + \mathbf{p}^-$); the second round-trip modeling yielding primaries and the first order of internal multiple: (d) downwards from z_0 to z_{N_z-1} (\mathbf{p}^+), (e) upwards from z_{N_z-1} to z_0 (\mathbf{p}^-) and (f) their summation ($\mathbf{p}^+ + \mathbf{p}^-$).

and 2.5. By one down-going extrapolation from z_0 to z_{N_z-1} and one up-going extrapolation from z_{N_z-1} to z_0 , one round-trip of modeling is constructed, yielding the primaries. Based on the current wavefields, another round-trip of modeling is constructed, yielding primaries and the first-order of internal multiples. Note that transmission effects are automatically included as well. We visualize the whole process with the snapshots at 0.44s and pseudo VSP cross-sections at 1600m of the modeled middle-shot wavefields in Figure 2.4 and Figure 2.5, respectively. It is clearly visible that the internal multiples are generated during the second round-trip of modeling.

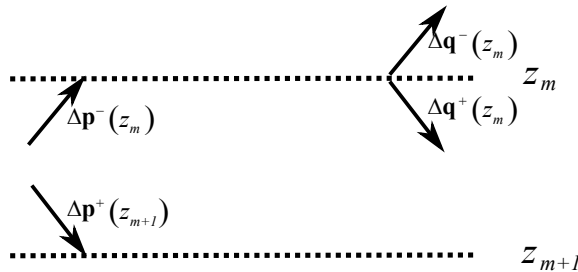


Figure 2.6: Schematic illustration of the redatumed residual wavefields.

2.3. INVERSION

Due to the recursive form of FWMod, it is known that all wavefields at each depth level are functions of the parameters in the full solution space, which makes rigorous gradient

derivation impossible. Therefore, we make two assumptions in this work:

- All the wavefields saved from the previous round-trip of modeling are not treated as functions of reflectivity and propagation velocity;
- The contributions of transmissions are ignored when it comes to calculating the reflectivity gradients. Note that transmission effects are still taken into account in the modeling.

2

2.3.1. DEFINITION OF THE OBJECTIVE FUNCTION

In the inversion, subsurface parameters are updated by fitting the measured wavefields with the modeled wavefields. Therefore, we can define the following least-squares objective function at the surface:

$$J = \frac{1}{2} \sum_{\omega} \sum_{shots} \|\Delta \mathbf{p}^{-}(z_0)\|_2^2, \quad (2.9)$$

where $\|\cdot\|_2^2$ describes the sum of the squares of the values (i.e. the Frobenius norm). $\Delta \mathbf{p}^{-}(z_0)$ is the residual wavefield at the surface z_0 , which is the difference between the measured and modeled wavefields at the surface.

The nature of FWMod yields wavefields (up-/down-going in/outgoing wavefields) at each depth level. Assume we can 'measure' all the wavefields in the whole solution space, our forward modeled wavefields should perfectly match the 'measured' wavefields at each depth level, when the models are absolutely true. Therefore, in order to simplify the derivation of the gradients of reflectivities and velocity at a certain depth level z_m , we can project the objective function along with the measured wavefield at the surface into the following redefined objective functions [19, 26]:

$$\begin{aligned} J_1 &= \frac{1}{2} \|\Delta \mathbf{p}^{+}(z_{m+1})\|_2^2, \\ J_2 &= \frac{1}{2} \|\Delta \mathbf{p}^{-}(z_m)\|_2^2, \\ J_3 &= \frac{1}{2} \|\Delta \mathbf{q}^{+}(z_m)\|_2^2, \\ J_4 &= \frac{1}{2} \|\Delta \mathbf{q}^{-}(z_m)\|_2^2, \end{aligned} \quad (2.10)$$

where four redatumed residual wavefields are as follows: the down-going incoming residual wavefield $\Delta \mathbf{p}^{+}(z_{m+1})$, the up-going incoming residual wavefield $\Delta \mathbf{p}^{-}(z_m)$, the down-going outgoing residual wavefield $\Delta \mathbf{q}^{+}(z_m)$, the up-going outgoing residual wavefield $\Delta \mathbf{q}^{-}(z_m)$, illustrated in Figure 2.6. Under the two assumptions mentioned at the beginning of this section and based on equations 2.4 and 2.5, $\Delta \mathbf{q}^{+}(z_m)$ and $\Delta \mathbf{q}^{-}(z_m)$ are functions of $\mathbf{R}(z_m)$. Therefore, we will use J_3 and J_4 to update reflectivities. Note that $\Delta \mathbf{p}^{+}(z_{m+1})$ is also a function of $\mathbf{R}(z_m)$, however, according to equation 2.5, J_1 has the same contribution as J_3 regarding reflectivity update. When it comes to velocity update, $\Delta \mathbf{p}^{+}(z_{m+1})$ and $\Delta \mathbf{p}^{-}(z_m)$ are functions of $\mathbf{W}(z_m, z_{m+1})$ or $\mathbf{W}(z_{m+1}, z_m)$, which are the propagation operators in-between two consecutive levels. Therefore, J_1 and J_2 are used to update velocity. Note that $\Delta \mathbf{q}^{-}(z_m)$ is also a function of $\mathbf{W}(z_m, z_{m+1})$, however, based on equation 2.4, J_4 has

the same contribution as J_2 regarding velocity update. These redatumed residual wavefields are calculated by adjoint (time-reverse) full wavefield modeling with the residual wavefield at the surface $\Delta \mathbf{p}^- (z_0)$ as the adjoint source [27].

2.3.2. GRADIENTS OF THE REFLECTIVITY AND PROPAGATION VELOCITY

Regarding the gradient of the reflectivity model, by using equations 2.4 and 2.5 and considering the assumptions, we take the partial derivative of J_3 and J_4 relative to $r_i (z_m)$ (one element: $\mathbf{r} (z_m)$ at lateral location x_i):

$$\begin{aligned}
 \frac{\partial J_3}{\partial r_i (z_m)} &= -\frac{\partial q_i^+ (z_m)}{\partial r_i (z_m)} \{\Delta q_i^+ (z_m)\}^H \\
 &= -\frac{\partial \{r_i (z_m) p_i^- (z_m)\}}{\partial r_i (z_m)} \{\Delta q_i^+ (z_m)\}^H \\
 &= -p_i^- (z_m) \{\Delta q_i^+ (z_m)\}^H, \\
 \frac{\partial J_4}{\partial r_i (z_m)} &= -\frac{\partial q_i^- (z_m)}{\partial r_i (z_m)} \{\Delta q_i^- (z_m)\}^H \\
 &= -\frac{\partial \{-r_i (z_m) p_i^+ (z_m)\}}{\partial r_i (z_m)} \{\Delta q_i^- (z_m)\}^H \\
 &= p_i^+ (z_m) \{\Delta q_i^- (z_m)\}^H,
 \end{aligned} \tag{2.11}$$

where $(.)^H$ represents Hermitian conjugate. $p_i^\pm (z_m)$, $q_i^\pm (z_m)$, $\Delta q_i^\pm (z_m)$, $\Delta p_i^\pm (z_m)$ denote the wavefields at lateral location x_i . From equation 2.11, we can see that the gradient of reflectivity operator is given by cross-correlating wavefields propagating in opposite directions. The schematic illustration is shown in Figure 2.7.

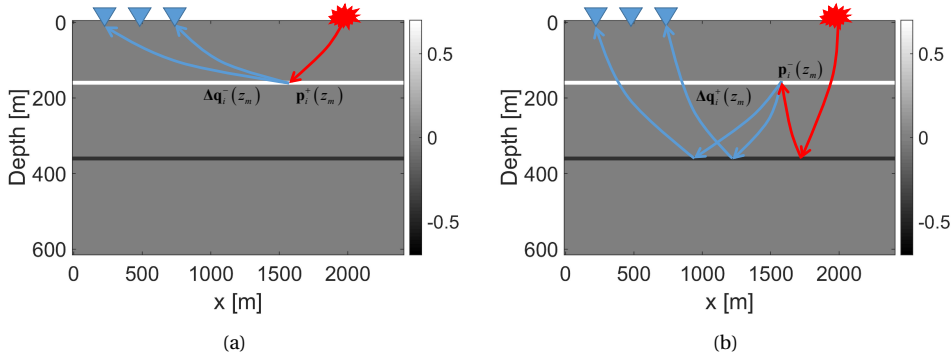


Figure 2.7: Schematic illustration of the reflectivity gradient contributions by combining wavefields propagating in opposite directions: (a) the contribution by combining the down-going incoming modeled wavefield $\mathbf{p}^+ (z_m)$ with the up-going outgoing residual wavefield $\Delta \mathbf{q}^- (z_m)$; (b) the contribution by combining the up-going incoming modeled wavefield $\mathbf{p}^- (z_m)$ with the down-going outgoing residual wavefield $\Delta \mathbf{q}^+ (z_m)$. The blue triangles and red explosive mark on the surface represent receivers and source, respectively.

In a similar way, for the gradient of the propagation velocity, we take the partial derivative of J_1 and J_2 relative to the in-between propagation velocity $v_i(z_m)$:

$$\begin{aligned}
\frac{\partial J_1}{\partial v_i(z_m)} &= -\frac{\partial p_i^+(z_{m+1})}{\partial v_i(z_m)} \{\Delta p_i^+(z_{m+1})\}^H \\
&= -\frac{\partial \{\mathbf{w}_i^\dagger(z_{m+1}, z_m) \mathbf{q}^+(z_m)\}}{\partial v_i(z_m)} \{\Delta p_i^+(z_{m+1})\}^H \\
&= -\left\{ \frac{\partial \mathbf{w}_i^\dagger(z_{m+1}, z_m)}{\partial v_i(z_m)} \mathbf{q}^+(z_m) \right\} \{\Delta p_i^+(z_{m+1})\}^H \\
\frac{\partial J_2}{\partial v_i(z_m)} &= -\frac{\partial p_i^-(z_m)}{\partial v_i(z_m)} \{\Delta p_i^-(z_m)\}^H \\
&= -\frac{\partial \{\mathbf{w}_i^\dagger(z_m, z_{m+1}) \mathbf{q}^-(z_{m+1})\}}{\partial v_i(z_m)} \{\Delta p_i^-(z_m)\}^H \\
&= -\left\{ \frac{\partial \mathbf{w}_i^\dagger(z_m, z_{m+1})}{\partial v_i(z_m)} \mathbf{q}^-(z_{m+1}) \right\} \{\Delta p_i^-(z_m)\}^H.
\end{aligned} \tag{2.12}$$

Now, we elaborate the gradient of $\mathbf{w}_i^\dagger(z_{m+1}, z_m)$ and $\mathbf{w}_i^\dagger(z_m, z_{m+1})$ relative to $v_i(z_m)$. The derivative of a vector by a scalar is known as the tangent vector:

$$\frac{\partial \mathbf{w}_i^\dagger(z_{m+1}, z_m)}{\partial v_i(z_m)} \equiv \frac{\partial \mathbf{w}_i^\dagger(z_m, z_{m+1})}{\partial v_i(z_m)} = \mathcal{F}_x^{-1} \left[\frac{j\omega\Delta z}{v_i^2(z_m)} \frac{k}{k_z} e^{-jk_z\Delta z} e^{jk_x x_i} \right]. \tag{2.13}$$

Note that the size of $\frac{\partial \mathbf{w}_i^\dagger(z_{m+1}, z_m)}{\partial v_i(z_m)}$, $\frac{\partial \mathbf{w}_i^\dagger(z_m, z_{m+1})}{\partial v_i(z_m)}$, $\mathbf{q}^+(z_m)$ and $\mathbf{q}^-(z_{m+1})$ is $(1 \times N_x)$ and $(N_x \times 1)$, respectively. Therefore, the size of their multiplication is (1×1) which matches $\{\Delta p_i^+(z_{m+1})\}^H$ and $\{\Delta p_i^-(z_m)\}^H$. From equation 2.12, we can see that the gradient of propagation velocity is given by combining the wavefields going in the same direction. The schematic illustration is shown in Figure 2.8.

By repeating equation 2.11 and 2.12, we calculate all the gradient contributions in the full solution space. In the end, we sum them together over shots and frequencies, yielding the final gradients.

2.3.3. OPTIMIZATION

After the gradients are calculated, the parameters can be updated and the residual wavefields are slowly driven to zero by utilizing an appropriate optimization approach [10, 12]. The flow diagram of the JMI process was already shown in Figure 1.3(b). One of the key features of the JMI process is the parameterization: two separate sets of parameters — \mathbf{r} and \mathbf{v} — have orthogonal effects on the modeled data; the reflectivity is responsible for the amplitudes of the reflections, and the propagation velocity is responsible for the phase effects of them. Regarding minimizing the residual wavefields during inversion, the zero-phase part of the residual contributes to the reflectivity gradient and the non-zero-phase part contributes to the propagation velocity gradient, which are also orthogonal to each other. This type of parameterization allows temporarily non-physical solutions: if the velocity is wrong at the beginning, the reflectivity will be estimated at the wrong depth level,

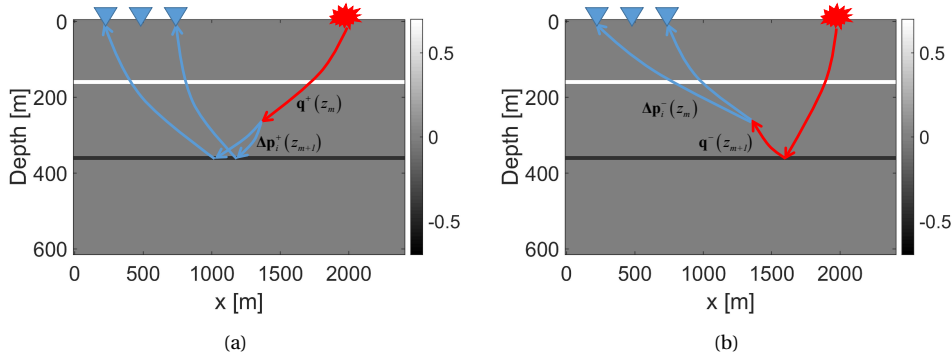


Figure 2.8: Schematic illustration of the velocity gradient contributions by combining wavefields propagating in the same direction: (a) the contribution by combining the down-going outgoing modeled wavefield $\mathbf{q}^+(z_m)$ with the down-going incoming residual wavefield $\Delta\mathbf{p}^+(z_{m+1})$; (b) the contribution by combining the up-going outgoing modeled wavefield $\mathbf{q}^-(z_{m+1})$ with the up-going incoming residual wavefield $\Delta\mathbf{p}^-(z_m)$. The blue triangles and red explosive mark on the surface represent receivers and source, respectively.

but the modeled events are still not too far from the measured data (i.e. the near-offset part of data fits well). Therefore, the cycle-skipping effects are largely suppressed. This feature makes JMI robust to the initial model.

2.3.4. NUMERICAL DEMONSTRATION

As we mentioned in Section 2.3.2, the gradient of reflectivity is calculated by combining wavefields propagating in opposite directions and the gradient of propagation velocity is given by combining wavefields going in the same direction. For the purpose of visualizing the gradient calculation, we assume two scenarios: (1) when there is an error in the reflectivity model, but the velocity model is correct; (2) when there is an error in the velocity model and the associated error in the reflector depth level.

The first scenario is shown in Figure 2.9. Due to the reflectivity error, the amplitude of the modeled wavefield is wrong compared to the measured one (Figures 2.9(a)-2.9(c)). This residual wavefield is then back-projected into the reflectivity gradient. Figure 2.9(d) shows the gradient from one shot record and Figure 2.9(e) shows the full gradient by summing together the contributions from all the shots.

The second scenario is shown in Figure 2.10. There is a velocity error in the first layer. In Figures 2.10(a)-2.10(c), it can be observed that the zero-offset part of the modeled wavefield fits well with the measured one, because the reflectivity updates in JMI are always estimated at certain depth levels to at least make the near-offset part of data fit well. Therefore, error in the velocity model results in the associated error in the reflector depth levels. In the case of a too low velocity model, the reflectors are estimated at shallower depth levels, and vice versa. In this way, the cycle-skipping effects are suppressed. Another observation is that the larger the offset, the larger the misfits between the modeled and measured wavefield, which are then used to calculate the velocity gradient. For one shot

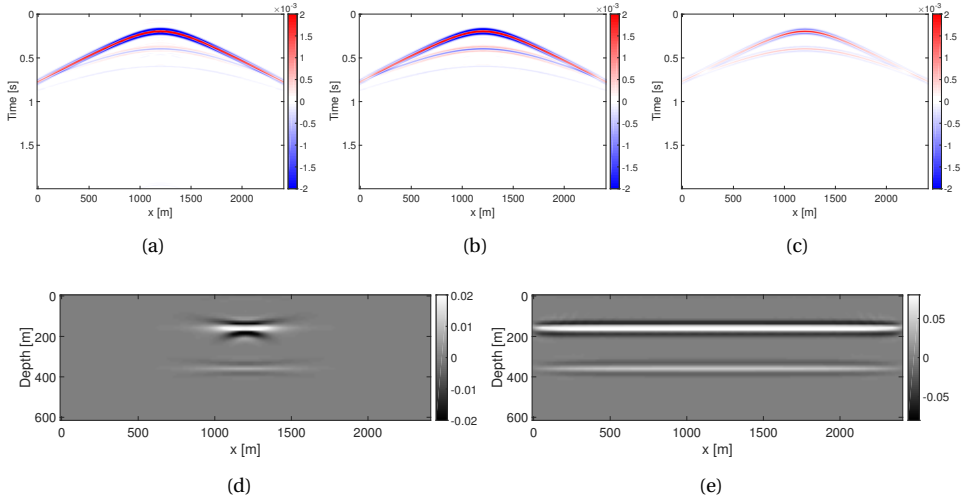


Figure 2.9: Numerical example based on the simple model in Figure 2.3: the scenario when there is an error in the reflectivity model, but the velocity model is correct. (a) The measured wavefield, (b) the modeled wavefield, (c) the residual wavefield; (d) the reflectivity gradient calculated from one shot record, (e) the reflectivity gradient by summing together the contributions from all the shot records.

record, the gradient is shown in Figure 2.10(d). After combining the contributions from all the shot records, the full gradient is shown in Figure 2.10(e).

2.4. EXAMPLE

In order to demonstrate the effectiveness of JMI as a time-lapse processing tool, we consider the baseline model shown in Figures 2.11(a) and 2.11(b), which are modified from the well-known Marmousi model. We add two gas-sand traps and one oil-sand trap to the original Marmousi model according to the geology information of Marmousi provided by [28]. Several time-lapse changes are embedded in the monitor model. For the gas-sand traps, water-gas replacement causes a 100 m/s increase on the reservoir velocity, and for the oil-sand trap, injection reduces the reservoir velocity by -150 m/s . Furthermore, overall subsurface, pressure perturbations are also considered. The reasonable velocity changes caused by such pressure perturbation in the reservoir are approximately 4% of the local velocity. And that of the overburden and underburden areas are around 0 – 2% and decreases as a function of distance to the reservoir. In addition, a small water-layer velocity change caused by an assumed water temperature change is also included. Details about the imposed time-lapse variation are shown in Figures 2.11(c) and 2.11(d). According to OBN (Ocean Bottom Node) acquisition, the source sampling is designed as 20 m , and the receiver sampling is 200 m . The time-lapse datasets are generated using FWMod, including multiples (both surface and internal multiples) and transmission effects. Initial reflectivities are zero and the initial velocity model is a very simple vertical gradient (shown

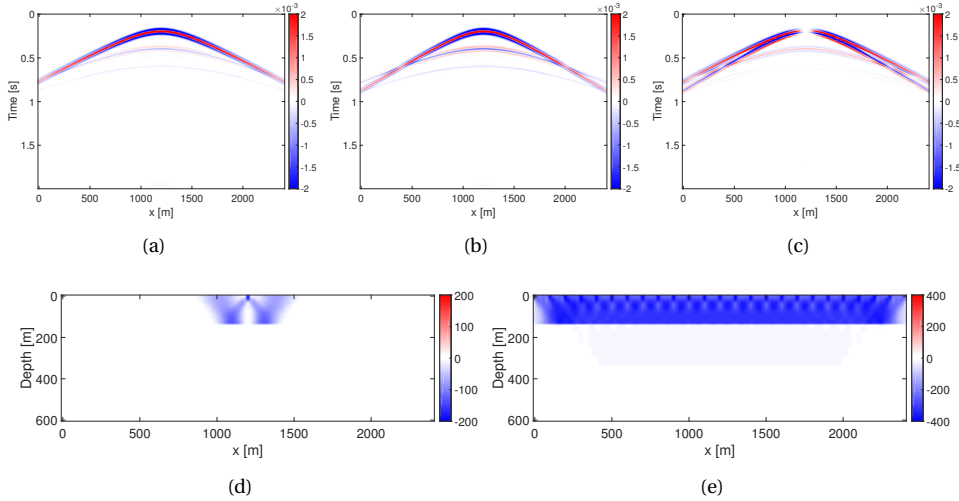


Figure 2.10: Numerical example based on the simple model in Figure 2.3: the scenario when there is an error in the velocity model and the associated error in the reflector depth level. (a) The measured wavefield, (b) the modeled wavefield, (c) the residual wavefield; (d) the velocity gradient calculated from one shot record, (e) the velocity gradient by summing together the contributions from all the shot records.

in Figures 2.11(e) and 2.11(f)). The band-width of frequency used for JMI is $5\text{ Hz} - 40\text{ Hz}$, and 20% random noise energy is added to the datasets. Table 2.1 shows a list of acquisition and inversion parameters used in this example.

Table 2.1: Marmousi example: a list of acquisition and inversion parameters.

Modeling method	Band-width	Surface/Internal multiple	Random noise	Wavelet	Source arrangement	Receiver arrangement	Other
FWMod	5 – 40 Hz	Yes/Yes	20%	Ricker, 20 Hz peak freq.	0 – 4000 m with 20 m spacing at $z = 0\text{ m}$	0 – 4000 m with 200 m spacing at $z = 0\text{ m}$	

In this example, we compare two strategies: a conventional time-lapse strategy based on a time-shift map and sequential JMI. First of all, the baseline reflectivity and velocity are inverted using JMI and the results are shown in Figures 2.12. This baseline velocity then serves as the velocity model in the conventional time-shift-based method and as the starting model for sequential JMI. Because of the inversion process included in JMI, the inverted image is quite accurate and the estimated velocity model also exhibits some details regarding the true structures. Here fine details are not expected in the inverted velocity model, as it only explains the propagation effects in the data.

The workflow of the conventional strategy based on a time-shift map is shown in Figure 2.13. The monitor image is then inverted using FWM with the baseline velocity model in Figure 2.12(a). This inverted monitor image is shown in Figure 2.15(a). Afterwards, both

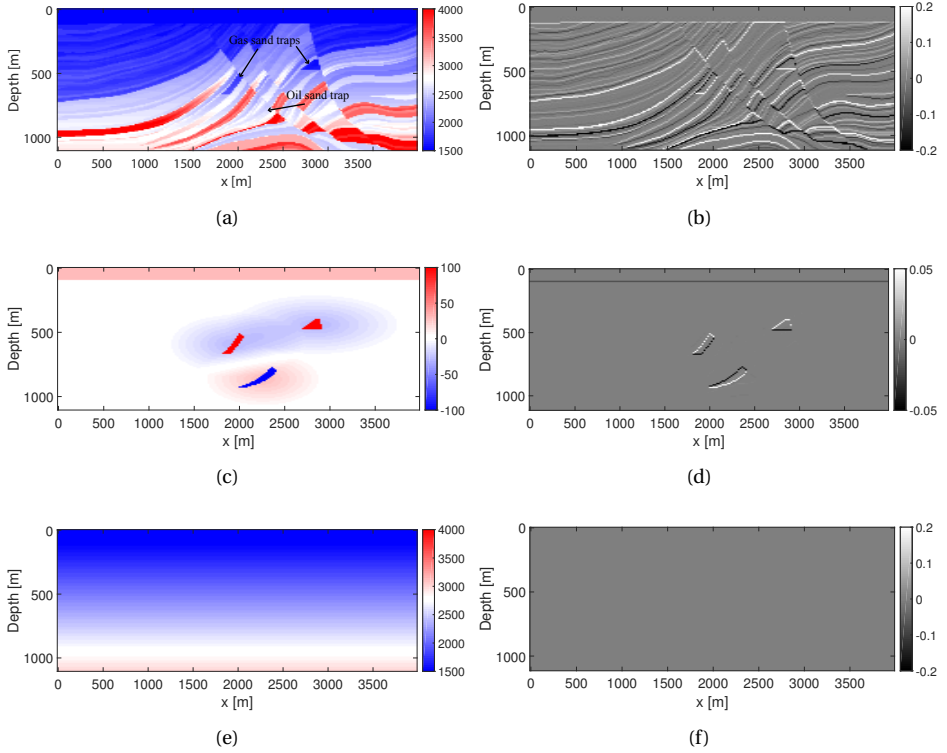


Figure 2.11: Marmousi example: (a) and (b) the true baseline velocity and reflectivity model; (c) and (d) the true time-lapse velocity difference and reflectivity difference; (e) and (f) the initial velocity and reflectivity model.

baseline and monitor images are converted to the time domain via stretching. Next, the corresponding time-variant time-shift map is calculated using a local cross-correlation method with a 300ms time window, the results being shown in Figure 2.15(b). By ignoring the layer compaction, the time-shift τ is related to the velocity difference ΔV by $\frac{\partial \tau}{\partial t} = -\frac{\Delta V}{V}$ [29]. Therefore, the velocity difference can be calculated from $\Delta V = -V \frac{\partial \tau}{\partial t}$, which is shown in Figure 2.15(c). It can be seen that this velocity difference is a very coarse indicator of the true velocity changes with low resolution and accuracy. The shifted image difference calculated by the time-shift map is shown in Figure 2.15(d). The positions of the true time-lapse changes are pointed out with black and white arrows. We can see that the shifted time-lapse image difference is of quite good quality. To some extent, this conventional approach with FWM as the imaging tool, which takes multiples and transmission effects into account, serves its purpose, however, fails to indicate the time-lapse velocity changes accurately.

The workflow of sequential JMI is shown in Figure 2.14. We apply JMI again to both the baseline and monitor datasets, yielding the inverted baseline and monitor results shown

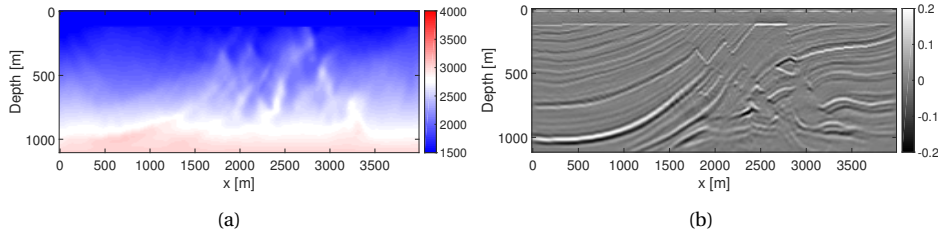


Figure 2.12: Marmousi example: (a) and (b) the inverted baseline velocity and reflectivity model using JMI. This baseline velocity then serves as the velocity model in the conventional time-shift-based method and as the starting model for sequential JMI.

in Figures 2.16(a)-2.16(d). After subtracting the inverted results of JMI of each dataset, the time-lapse differences are shown in Figures 2.16(e) and 2.16(f). It is obvious that the time-lapse changes in Figure 2.16(e) can be easily distinguished, including the small changes due to the velocity changes in the water-layer. Therefore, sequential JMI is a more effective time-lapse velocity indicator compared to the conventional time-shift strategy. By comparing Figure 2.16(f) to Figure 2.15(d), we can see that the inverted image changes using sequential JMI are further improved by employing automatic velocity updating during the independent process, especially the time-lapse changes in the oil-sand trap. However, there are still many obvious imprints in both time-lapse image and velocity differences.

2.5. DISCUSSION

2.5.1. HANDLING AVO EFFECTS

In order to handle the angle-versus-offset (AVO) effects in the data, the reflectivity operator \mathbf{R} in Equation 2.4 is supposed to be an angle-dependent parameter [11, 18], which means it is a function of incident angles. However, this complete version of reflectivity leads to a very large solution space, therefore puts JMI into the danger of over-parameterization. The velocity errors might be compensated by some wrong updates of angle-dependent reflectivities. Thus, in this work, we make an assumption of scalar reflectivity operators by only using the diagonal values of the reflectivity operator. As a result, this version of JMI cannot easily handle large-offset data due to the AVO effects. We propose to mitigate this AVO challenge in JMI using a local attribute – local orthogonalization – between the modeled and measured data during inversion. The smoothed local orthogonalization weight indicates those areas of modeled data that do not correlate well with the measured data. Afterwards, the high weight part containing strong AVO effects is suppressed adaptively from the residual based on the local orthogonalization weights. As a result, the artifacts brought by the AVO effects in the inverted models are largely suppressed. Appendix A provides more theoretical details and demonstrates the effectiveness of this proposed method with a complex synthetic example.

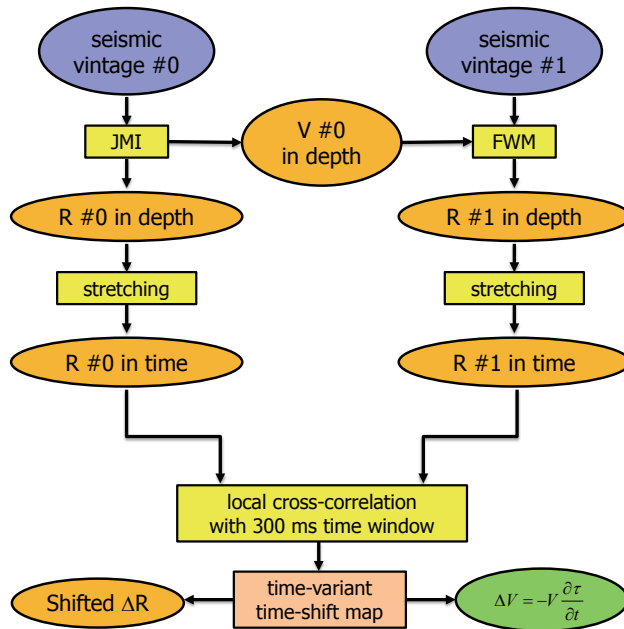


Figure 2.13: The flow chart related to the conventional strategy based on a time-shift map.

2.5.2. INDEPENDENT PROCESSING STRATEGY

Both the conventional time-shift-map-based method and sequential JMI are based on an independent processing strategy, which means the time-lapse changes are obtained by subtracting the results of independent process on each dataset. Artifacts are often introduced in addition to the real time-lapse changes due to the non-repeatable uncertainties between different datasets, which are caused by noise, acquisition designs, and independent processing steps. For example, in the following three scenarios, this independent processing strategy fails:

- The acquisition geometries of the monitoring surveys are not repeated very well;
- The acquisition geometries of the monitoring surveys are under-sampled with very sparse receivers or sources;
- Various processing "tricks" are included inside the independent processing sequence, such as illumination preconditioning, smoothing of the gradients, advanced optimization methods, etc.

All these scenarios increase the non-repeatable uncertainties during the process of different datasets. In order to relax these rigid requirements, a better processing strategy is desirable, and this leads to the next chapter.

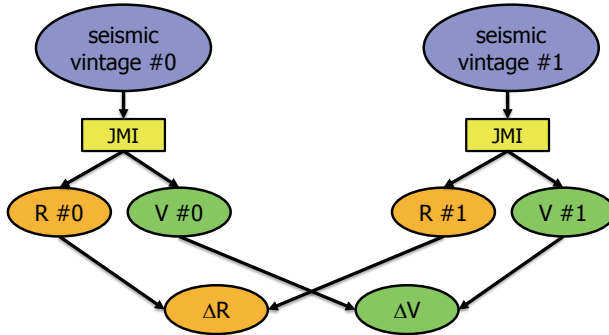


Figure 2.14: The flow chart related to sequential JMI.

2.6. CONCLUSION

In the conventional time-lapse processing workflow, multiple removal from the data is needed as a preprocessing step. Then an independent imaging process is employed on each dataset based on the same estimated baseline velocity model. Afterwards, a time-shift-map-based method is applied to realign the images to compensate the ignored velocity variations between different surveys. However, in practice, we usually are unable to remove all multiples from the datasets completely and the time-shift-map tool is normally under the assumption of a local 1D subsurface. Therefore, we propose to use a better imaging process — JMI — which is able to make use of multiples and at the same time take velocity variations between surveys into account.

Joint Migration Inversion with its modeling tool Full Wavefield Modeling has been described. The main features of JMI are as follows:

- Scale separation of parameters:
Two separate sets of parameters — reflectivity and propagation velocity — have orthogonal effects on the modeled data; the reflectivity is responsible for the amplitude effects of the data, and the propagation velocity is responsible for the phase effects.
- Flexible building block in FWMod (no finite-difference-based methods are used):
It consists of two parts: reflection and transmission at each level and propagation in-between two consecutive levels. It is quite flexible and can be easily extended to include more physics, e.g. anisotropy, Q-effects, and elastic amplitudes.
- Transmission effects and internal multiples are included.
- Propagation velocity estimation is automatically included in a fully hands-off manner.
- It is robust to the initial model:
When given the wrong velocity model, JMI always estimates the reflectors at the most proper depth levels to at least make the near-offset part of data fit well. Therefore, cycle-skipping effects are suppressed.

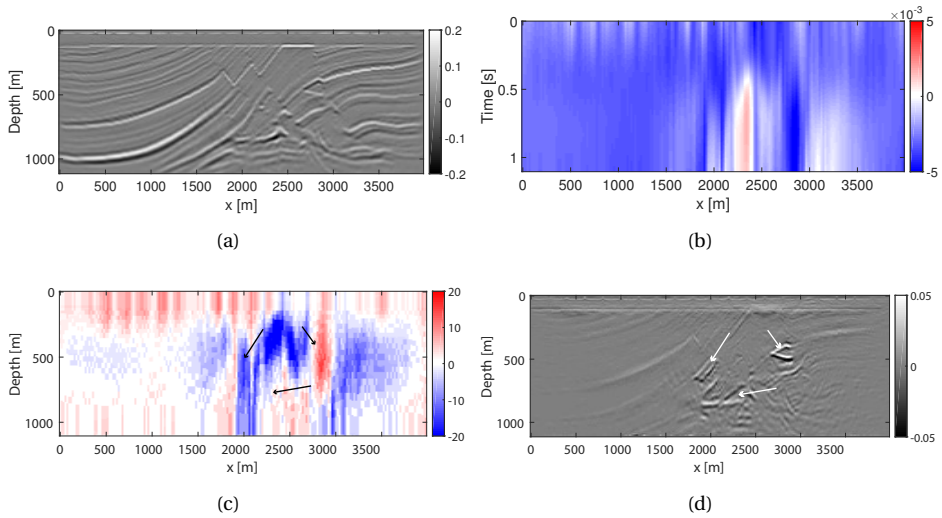


Figure 2.15: Marmousi example: (a) the inverted monitor reflectivity model using FWM with the baseline velocity model in Figure 2.12(b); (b) the time-variant time-shift map; (c) and (d) the calculated time-lapse velocity-difference and shifted reflectivity-difference based on the time-shift map. The positions of the true time-lapse changes are pointed out with black and white arrows.

Finally, with a complex synthetic example based on the Marmousi model, we demonstrate that sequential JMI, which utilizes JMI as the time-lapse processing tool, is a better indicator of the time-lapse effects, compared to the conventional time-shift-map-based method.

REFERENCES

- [1] R. Arts, R. Elsayed, L. Van Der Meer, O. Eiken, S. Ostmo, A. Chadwick, G. Kirby, and B. Zinszner, *Estimation of the mass of injected CO₂ at Sleipner using time-lapse seismic data*, in *64th EAGE Conference & Exhibition* (2002).
- [2] R. Arts, O. Eiken, A. Chadwick, P. Zweigel, L. Van der Meer, and B. Zinszner, *Monitoring of CO₂ injected at Sleipner using time-lapse seismic data*, *Energy* **29** (2004), pp. 1383–1392.
- [3] A. Tura, T. Barker, P. Cattermole, C. Collins, J. Davis, P. Hatchell, K. Koster, P. Schutjens, and P. Wills, *Monitoring primary depletion reservoirs using amplitudes and time shifts from high-repeat seismic surveys*, *The Leading Edge* **24** (2005), pp. 1214–1221.
- [4] M. Trani, R. Arts, O. Leeuwenburgh, and J. Brouwer, *Estimation of changes in saturation and pressure from 4D seismic AVO and time-shift analysis*, *Geophysics* **76** (2011), pp. C1–C17.

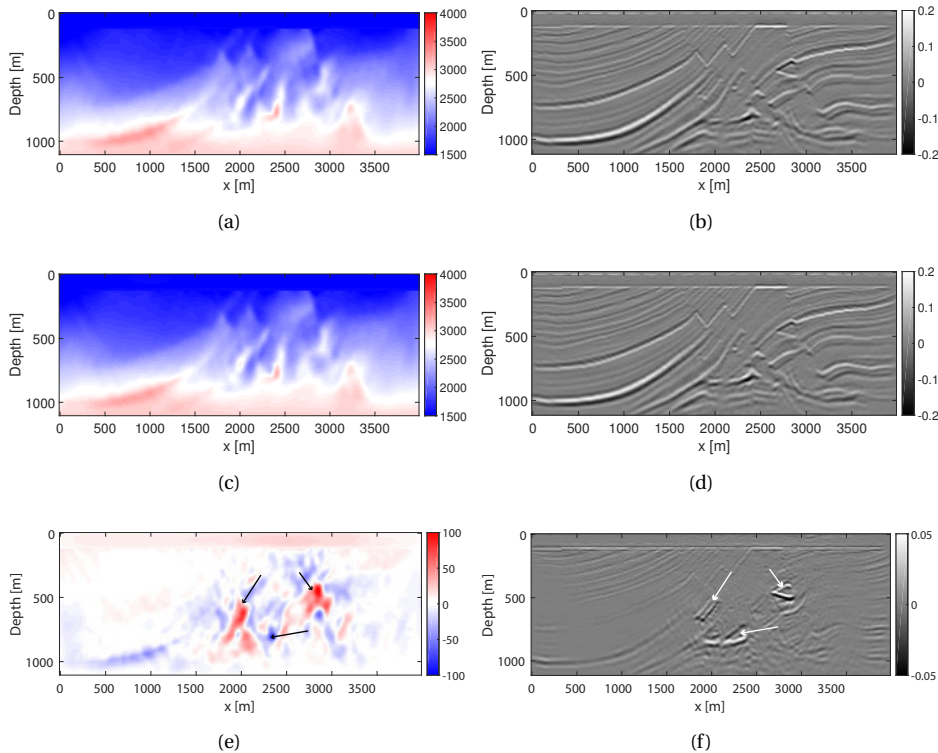


Figure 2.16: Marmousi example: the results using sequential JMI with Figure 2.12(b) as the starting model: (a) and (b) the inverted baseline velocity and reflectivity model; (c) and (d) the inverted monitor velocity and reflectivity model; (e) and (f) the inverted time-lapse velocity- and reflectivity-difference. The positions of the true time-lapse changes are pointed out with black and white arrows.

- [5] P. Routh, G. Palacharla, I. Chikichev, and S. Lazaratos, *Full wavefield inversion of time-lapse data for improved imaging and reservoir characterization*, in *SEG Technical Program Expanded Abstracts 2012* (Society of Exploration Geophysicists, 2012) pp. 1–6.
- [6] G. Ayeni and B. Biondi, *Target-oriented joint least-squares migration/inversion of time-lapse seismic data sets*, *Geophysics* **75** (2010), pp. R61–R73.
- [7] D. Yang, M. Meadows, P. Inderwiesen, J. Landa, A. Malcolm, and M. Fehler, *Double-difference waveform inversion: Feasibility and robustness study with pressure data*, *Geophysics* **80** (2015), pp. M129–M141.
- [8] A. J. Berkhout, *Combining full wavefield migration and full waveform inversion, a glance into the future of seismic imaging*, *Geophysics* **77** (2012), pp. S43–S50.

- [9] X. Staal and D. Verschuur, *Velocity estimation using internal multiples*, in *SEG Technical Program Expanded Abstracts 2012* (Society of Exploration Geophysicists, 2012) pp. 1–5.
- [10] X. R. Staal and D. J. Verschuur, *Joint migration inversion, imaging including all multiples with automatic velocity update*, in *75th EAGE Conference & Exhibition incorporating SPE EUROPEC 2013* (2013).
- [11] A. J. Berkhout, *Review paper: An outlook on the future of seismic imaging, Part III: Joint migration inversion*, *Geophysical Prospecting* **62** (2014), pp. 950–971.
- [12] D. J. Verschuur, X. R. Staal, and A. J. Berkhout, *Joint migration inversion: Simultaneous determination of velocity fields and depth images using all orders of scattering*, *The Leading Edge* **35** (2016), pp. 1037–1046.
- [13] A. J. Berkhout, *Review paper: An outlook on the future of seismic imaging, Part I: forward and reverse modelling*, *Geophysical Prospecting* **62** (2014), pp. 911–930.
- [14] T. Nemeth, C. Wu, and G. T. Schuster, *Least-squares migration of incomplete reflection data*, *Geophysics* **64** (1999), pp. 208–221.
- [15] D. Verschuur and X. Staal, *Using primaries and multiples in time-lapse imaging and velocity estimation*, in *SEG Technical Program Expanded Abstracts 2014* (Society of Exploration Geophysicists, 2014) pp. 4955–4959.
- [16] D. J. Verschuur, *Time-lapse imaging for a strongly scattering overburden via joint-migration inversion*, in *77th EAGE Conference and Exhibition 2015* (Eur. Ass. of Geosc. and Eng., Expanded abstracts, 2015).
- [17] N. K. Kinneging, V. Budejicky, C. P. A. Wapenaar, and A. J. Berkhout, *Efficient 2D and 3D shot record redatuming*, *Geophysical Prospecting* **37** (1989), pp. 493–530.
- [18] M. Davydenko and D. J. Verschuur, *Full-wavefield migration: using surface and internal multiples in imaging*, *Geophysical Prospecting* **65** (2017), pp. 7–21.
- [19] Y. Sun, E. Verschuur, and S. Qu, *Research note: derivations of gradients in angle-independent joint migration inversion*, *Geophysical Prospecting* **67** (2019), pp. 572–579.
- [20] J. Gazdag, *Wave equation migration with the phase-shift method*, *Geophysics* **43** (1978), pp. 1342–1351.
- [21] H. Bremmer, *The W.K.B. approximation as the first term of a geometric-optical series*, *Communications on Pure and Applied Mathematics* **4** (1951), pp. 105–115.
- [22] C. P. A. Wapenaar, N. K. Kinneging, and A. J. Berkhout, *Principle of prestack migration based on the full elastic two-way wave equation*, *Geophysics* **52** (1987), pp. 151–173.
- [23] A. A. Alshuhail and D. J. Verschuur, *Robust estimation of vertical symmetry axis models via joint migration inversion: Including multiples in anisotropic parameter estimation*, *Geophysics* **84** (2019), pp. C57–C74.

- [24] H. Alasmri and D. J. Verschuur, *Towards Q-compensation in full wavefield migration and joint migration inversion*, in *81th EAGE Conference and Exhibition 2019* (Eur. Ass. of Geosc. and Eng., Expanded abstracts, 2019).
- [25] A. Garg and D. Verschuur, *Elastic reflectivity preserving full-wavefield inversion*, in *SEG Technical Program Expanded Abstracts 2017* (Society of Exploration Geophysicists, 2017) pp. 5561–5566.
- [26] S. Qu, Y. Sun, and E. Verschuur, *Mitigating amplitude versus ray-parameter effect in joint migration inversion using a zero-lag crosscorrelation objective function of redatumed wavefields*, in *SEG Technical Program Expanded Abstracts 2018* (Society of Exploration Geophysicists, 2018) pp. 1133–1137.
- [27] R.-E. Plessix, *A review of the adjoint-state method for computing the gradient of a functional with geophysical applications*, *Geophysical Journal International* **167** (2006), pp. 495–503.
- [28] G. S. Martin, R. Wiley, and K. J. Marfurt, *Marmousi2: An elastic upgrade for marmousi*, *The Leading Edge* **25** (2006), pp. 156–166.
- [29] P. Hatchell and S. Bourne, *Rocks under strain: Strain-induced time-lapse time shifts are observed for depleting reservoirs*, *The Leading Edge* **24** (2005), pp. 1222–1225.

3

HIGH-RESOLUTION SIMULTANEOUS JOINT MIGRATION INVERSION

In both the conventional method based on a time-shift map and sequential JMI proposed in Chapter 2, time-lapse changes are obtained by subtracting the results of independent process on each dataset. Artifacts are often generated in addition to the actual time-lapse changes due to the non-repeatable uncertainties between different datasets caused by noise, acquisition designs, and independent process. Therefore, the currently employed time-lapse acquisition practice requires to exactly repeat well-sampled geometries to mitigate acquisition effects on the final time-lapse differences. Moreover, the independent process is always carefully tailored to maximally reduce the non-repeatable uncertainties during the processing step.

In order to relax these rigid requirements, we propose Simultaneous Joint Migration Inversion (S-JMI) as an effective time-lapse tool for reservoir monitoring, which combines a joint time-lapse data processing strategy with the Joint Migration Inversion (JMI) method. S-JMI inverts for both datasets simultaneously and utilizes various constraints on the estimated reflectivities and velocity. As a result, the obtained time-lapse differences have higher accuracy compared to inverting each dataset separately. S-JMI fits both datasets simultaneously and allows the baseline and monitor parameters to communicate and compensate with each other dynamically during inversion via a user-defined spatial weighting operator, thus, reducing the non-repeatable uncertainties during the time-lapse process. Moreover, in order to get more localized velocity differences, we further extend the regular S-JMI to a robust high-resolution S-JMI (HR-S-JMI) process by using the time-lapse reflectivity-difference as an extra constraint for the velocity-difference estimation during inversion. This constraint makes a link between the reflectivity- and the velocity-difference by exploiting the relationship between them. We demonstrate the feasibility of the proposed method with a complex synthetic example based on the same time-lapse models described in Section 2.4.

3.1. INTRODUCTION

In order to recover time-lapse physical changes (i.e. reflection amplitudes, travel-time), the most conventional approach is to perform an independent imaging process on each dataset produced by exactly repeated acquisitions, after multiple removal. Later on, a time-shift map estimated from the images is used to realign the reflectors, yielding the final time-lapse differences [1–5].

Joint Migration Inversion (JMI) aims to estimate the reflectivities along with propagation velocity through a data-fitting process [6–10]. The most straightforward extension of JMI to the time-lapse case is sequential JMI, which was discussed in Chapter 2. It conducts JMI on the baseline and monitor datasets independently, and the differences of the two resulting models should reveal the time-lapse changes. The schematic representations of the conventional time-shift-based approach and sequential JMI were already shown in Figures 1.4 and 1.6, respectively. Both methods mentioned above are based on an independent processing strategy. Artifacts are often introduced in addition to the true time-lapse changes due to the differences of noise, the acquisition design, and the uncertainties in the process between different datasets. Therefore, in order to mitigate these non-repeatable effects, the current time-lapse acquisition practice is to exactly repeat well-sampled geometries to mitigate acquisition effects on the final time-lapse differences [11]. Moreover, some processing "tricks" in the independent process, such as illumination, preconditioning, smoothing of gradients, etc, are always carefully tailored to maximally reduce the non-repeatable uncertainties [12–14]. However, we usually are unable to perfectly reconcile large differences in the acquisitions between different surveys or fully avoid the uncertainty differences between the independent processes. Therefore, one important question is: "Is there a better processing strategy which is less sensitive to these non-repeatable effects?"

Some researchers have already done investigations on the non-repeatability issues. [15] addressed it by using a joint time-lapse least-squares migration process, which reduces the differences of the uncertainties during process by fitting both datasets simultaneously. [14, 16, 17] extended this joint strategy to full waveform inversion. [18, 19] designed a cost-efficient non-repeated time-lapse acquisition, and then proposed to use a joint recovery scheme based on the curvelet transform to recover the 4D vintages. [20] proved that, because JMI is an inversion process, the actual locations of the seismic measurements — providing a sufficient illumination of the subsurface with primaries and multiples is achieved — is not so important, such that the method becomes largely independent of geometry. In this work, to mitigate the artifacts brought by these non-repeatable effects, we propose a high-resolution simultaneous JMI (HR-S-JMI) process, which combines the joint time-lapse strategy with the benefit of JMI, together with various constraints helping to get use of all the information and improve the resolution.

This chapter is organized as follows: we begin with the theory of S-JMI, including L2 constraints on both reflectivity- and velocity-differences via a user-defined spatial weighting function. After that, we introduce the theory of high-resolution S-JMI with two extra constraints on velocities: directional total variation regularization and a time-lapse reflectivity-difference constraint, which makes a link between reflectivity- and velocity-difference by constraining the relationship between them. Finally, we demonstrate the effectiveness of regular S-JMI and HR-S-JMI with a complex synthetic example based on

the same time-lapse model described in Section 2.4.

3.2. SIMULTANEOUS JMI

We rewrite the objective function 2.9 as:

$$J_{JMI} = \frac{1}{2} \sum_{\omega} \sum_{shots} \|\mathbf{d}^{-}(z_0) - \mathbf{p}^{-}(z_0, \mathbf{r}, \mathbf{v})\|_2^2, \quad (3.1)$$

where $\mathbf{p}^{-}(z_0, \mathbf{r}, \mathbf{v})$ describes the modeled up-going wavefield as a function of \mathbf{r} and \mathbf{v} . \mathbf{r} and \mathbf{v} represent reflectivity and propagation velocity in the whole solution space, respectively. Their size is $(N_x \times N_z)$. $\mathbf{d}^{-}(z_0)$ denotes the recorded wavefield at depth z_0 .

We proposed a simultaneous JMI method, which combines JMI with a simultaneous time-lapse processing strategy. Compared to the sequential JMI inverting each dataset sequentially, this simultaneous JMI makes it more suitable to handle non-repeatable effects. The flowchart of simultaneous JMI (S-JMI) is shown in Figure 3.1.

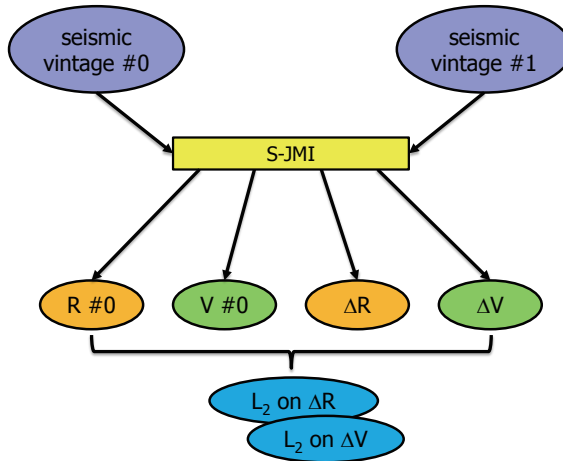


Figure 3.1: The flow chart of regular S-JMI.

In this work, we parameterize the S-JMI algorithm with the baseline reflectivity/velocity and the time-lapse reflectivity-/velocity-difference. In order to obtain more accurate time-lapse differences, we also extend it to include L2-norm constraints by minimizing the fol-

lowing objective function:

$$\begin{aligned}
J_{S-JMI} = & \frac{1}{2} \sum_{\omega} \sum_{shots} \|\mathbf{d}^-(z_0)[T_0] - \mathbf{p}^-(z_0, \mathbf{r}[T_0], \mathbf{v}[T_0])\|_2^2 \\
& + \frac{1}{2} \sum_{n=1}^{N_T-1} \sum_{\omega} \sum_{shots} \|\mathbf{d}^-(z_0)[T_n] - \mathbf{p}^-(z_0, \mathbf{r}[T_0] + \Delta\mathbf{r}[T_n], \mathbf{v}[T_0] + \Delta\mathbf{v}[T_n])\|_2^2 \\
& + \sum_{n=1}^{N_T-1} \lambda_1[T_n] \{ \|\Lambda_{\mathbf{r}}(x, z) \Delta\mathbf{r}[T_n]\|_2^2 + \|\Lambda_{\mathbf{v}}(x, z) \Delta\mathbf{v}[T_n]\|_2^2 \}, \\
\Delta\mathbf{r}[T_n] = & \mathbf{r}[T_n] - \mathbf{r}[T_0], n = 1, 2, \dots, N_T - 1, \\
\Delta\mathbf{v}[T_n] = & \mathbf{v}[T_n] - \mathbf{v}[T_0], n = 1, 2, \dots, N_T - 1,
\end{aligned} \tag{3.2}$$

where T_n represents the calendar-time (i.e. acquisition time) of the n^{th} dataset, and N_T is the total number of datasets. In particular, T_0 represents the baseline calendar-time. The first two terms in equation 3.2 are re-written from equation 3.1 corresponding to all the datasets as a function of baseline reflectivity/velocity and time-lapse reflectivity-/velocity-difference. The third term describes L2-norm constraints on the reflectivity- and velocity-difference, respectively, where $\lambda_1[T_n]$ is a weighting parameter. $\Lambda_{\mathbf{r}}$ and $\Lambda_{\mathbf{v}}$ are spatial weighting operators, where the values vary between 0 and 1. They are usually derived from some prior information and indicate where time-lapse variations in the subsurface model are expected (values close to 0 therefore, less penalized). This constraint makes it possible for the baseline and monitor parameters to communicate and compensate with each other during inversion: we impose that the reflectivities and velocities should be almost the same outside the area influenced by production, indicated via $\Lambda_{\mathbf{r}}$ and $\Lambda_{\mathbf{v}}$ being close to the value 1.

3.3. HIGH-RESOLUTION S-JMI — BRIDGING THE GAP BETWEEN REFLECTIVITY AND VELOCITY UPDATE

As explained in the theory of JMI, the propagation velocity inverted using JMI can only explain propagation effects in the data, while the high-frequency components of velocity are hidden in the reflectivities. Therefore, a high-resolution time-lapse velocity-difference can not be obtained using regular JMI. However, it is usually a demand. Therefore, we propose to add two extra constraints to equation 3.2 on baseline velocity and velocity-difference to get a more localized time-lapse velocity-difference. The flow chart of HR-S-JMI is shown in Figure 3.2. The new objective function can be formulated as follows:

$$\begin{aligned}
J_{high-res} = & J_{S-JMI} \\
& + \{\lambda_2[T_0] \|\mathbf{r}[T_0] - \mu[T_0] \mathbf{r}_{est}(\mathbf{v}[T_0])\|_2^2 \\
& + \sum_{n=1}^{N_T-1} \lambda_2[T_n] \|\Delta\mathbf{r}[T_n] - \mu[T_n] \Delta\mathbf{r}_{est}(\Delta\mathbf{v}[T_n])\|_2^2\}, \\
& + \{\lambda_3[T_0] (\|\nabla_1 \mathbf{v}[T_0]\|_1 + \|\nabla_2 \mathbf{v}[T_0]\|_1) \\
& + \sum_{n=1}^{N_T-1} \lambda_3[T_n] (\|\nabla_1 \Delta\mathbf{v}[T_n]\|_1 + \|\nabla_2 \Delta\mathbf{v}[T_n]\|_1)\}.
\end{aligned} \tag{3.3}$$

The first constraint in this equation helps to make a link between not only baseline reflectivity and velocity, but also time-lapse reflectivity- and velocity-difference. This basically is a constraint on the relationship between reflectivity and velocity, which can also be explained as a constraint on density. Note that this constraint was proposed by [21] and we extend it to a time-lapse application.

Assuming waves are normal-incident to the boundary between different depth levels and the density is constant, the reflectivities as a function of velocity can be simplified to:

$$r_{est}(x, z_{n+1}) \simeq \frac{v(x, z_{n+1}) - v(x, z_n)}{v(x, z_{n+1}) + v(x, z_n)}. \tag{3.4}$$

By additionally assuming that the horizontal variation of velocity is much smaller than the vertical variation, a numerical approximation of r_{est} and Δr_{est} can be obtained from v and Δv :

$$\begin{aligned} r_{est}(x, z_{n+1}) &\sim \{v(x, z_{n+1}) - v(x, z_n)\} * constant, \\ \Delta r_{est}(x, z_{n+1}) &\sim \{\Delta v(x, z_{n+1}) - \Delta v(x, z_n)\} * constant. \end{aligned} \tag{3.5}$$

As we can see from equation 3.5, the estimated reflectivity r_{est} and reflectivity-difference Δr_{est} do not contain the scale of the correct reflectivity, therefore, we approximate the correct scaling μ in equation 3.3 by balancing the energy between the estimated r_{est} and r , Δr_{est} and Δr . Afterwards, we obtain the high-frequency components of velocity and velocity-difference update from this constraint by taking the numerical integral of $\{r[T_0] - \mu[T_0] r_{est}(v[T_0])\}$ and $\{\Delta r[T_n] - \mu[T_n] \Delta r_{est}(\Delta v[T_n])\}$ along the z axis with a weighting parameter $\lambda_2[T_n]$.

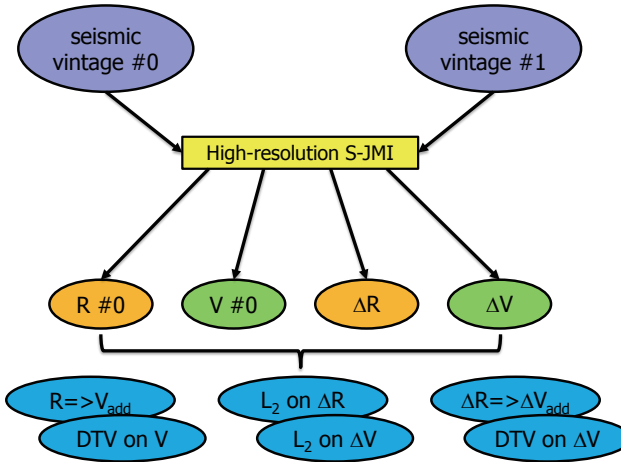


Figure 3.2: The flow chart of HR-S-JMI.

The second constraint in equation 3.3 denotes a directional total variation regularization [22] on the baseline velocity and velocity-difference. This constraint smooths the model by enhancing the sparsity of the spatial gradient of the velocity, thereby, preserving

its edges and meanwhile it optimally includes geologic information. ∇_1 and ∇_2 are the rotated and scaled version of horizontal and vertical gradient operator according to the local dip and weighting parameter, respectively. $\lambda_3 [T_n]$ controls the strength of the regularization. We solve the directional total variation using the split-Bregman iterative algorithm [23]. Appendix B provides more theoretical details and demonstrates the effectiveness of the directional total variation regularization with a complex synthetic example.

3

3.4. EXAMPLE

In order to demonstrate the effectiveness of S-JMI and high-resolution S-JMI as time-lapse processing tools, we consider the same time-lapse models, geometry settings and parameter settings described in Section 2.4. In this section, we show two more strategies: regular S-JMI and HR-S-JMI, and compare their results with the those from sequential JMI in Section 2.4.

The inverted baseline reflectivity and velocity using S-JMI are shown in Figures 3.3(a) and 3.3(b). Compared to Figures 2.16(a) and 2.16(b), S-JMI achieves better results with less distortions by making use of both datasets during inversion. From the inverted baseline results and some information about injection wells, we get to know the approximate positions of the reservoir and injection point, based on which the spatial weighting operators used in S-JMI are designed and shown in Figures 3.3(c) and 3.3(d).

In terms of time-lapse differences, much better results are achieved by using S-JMI for both reflectivity and velocity model shown in Figures 3.3(e) and 3.3(f), when comparing them to the results using sequential JMI in Figures 2.16(e) and 2.16(f). The true reservoir-related time-lapse changes are pointed out with black and white arrows. The image-difference is very clear and the velocity time-lapse effects can also be distinguished now, even through their resolution is not as good as the true time-lapse effects. They look somehow smeared, because the velocity model achieved by the regular S-JMI can only explain propagation effects in the data. The high-frequency components of velocity are still hidden in the reflectivities. Still, by observing the good recovery of the reflectivity-differences, we can tell that the current inverted velocity model is good enough to explain the propagation effects, which means the vertical integral of this smooth velocity difference is almost equal to the integral of the true one. Regarding the changes outside the reservoirs, the small water-layer change is also well-recovered.

The inverted baseline results by using HR-S-JMI are shown in Figures 3.4(a) and 3.4(b). More fine details can be seen in Figure 3.4(a) due to the link between the velocity and reflectivity update together with the directional TV in HR-S-JMI. Because the inverted velocity using regular S-JMI is already able to explain the propagation effects very well, a velocity model with fine details does not make an obvious difference to improving the reflectivity result. The inverted time-lapse differences obtained by using HR-S-JMI are shown in Figures 3.4(c) and 3.4(d). The inverted velocity-difference is more localized compared to Figure 3.3(e) by exploiting the relationship between the reflectivity- and the velocity-difference. However, as was mentioned earlier, a more localized velocity-difference does not make much difference for the improvement of the inverted reflectivity-difference.

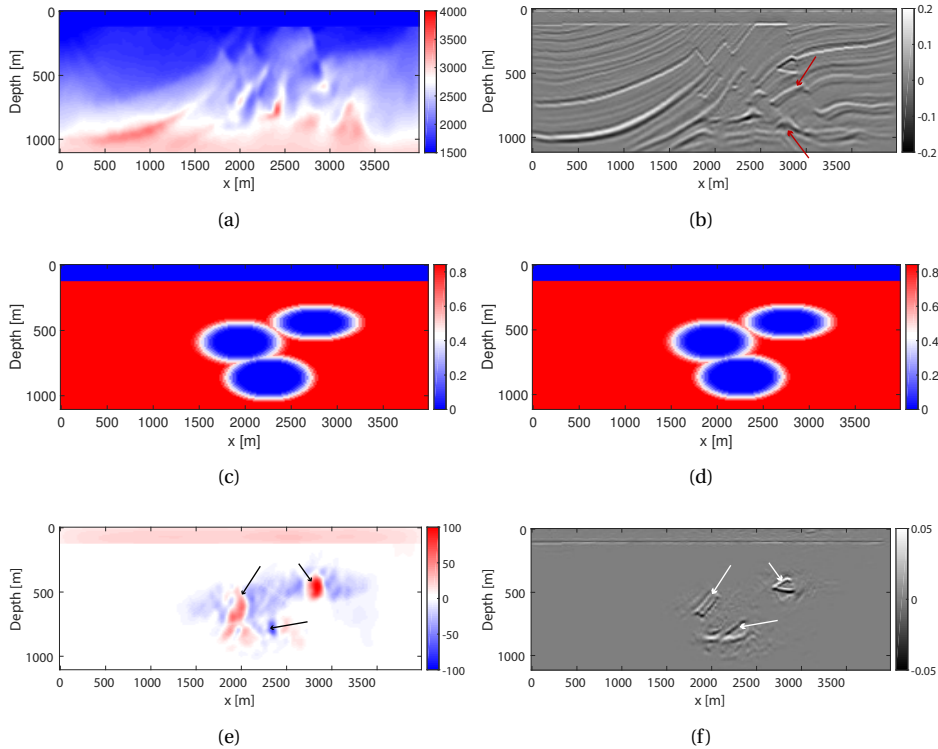


Figure 3.3: Marmousi example: (a) and (b) the inverted baseline velocity and reflectivity model using regular S-JMI. The improvements compared to Figure 2.16(b) are highlighted using red arrows; (c) and (d) the spatial weighting operators for velocity and reflectivity; (e) and (f) the inverted time-lapse velocity- and reflectivity-difference using regular S-JMI. The positions of the true time-lapse changes are pointed out with black and white arrows.

3.5. DISCUSSION

3.5.1. COMPUTATIONAL REQUIREMENTS

The conventional method based on a time-shift map is the most efficient one. However, it fails to act as an indicator of the actual velocity-difference. Assuming the amount of computation efforts of JMI applied to one vintage is K , the computation time of S-JMI and sequential JMI is around $2K$. In the case when more seismic vintages are available, there is no need to invert all the datasets together. Instead, one high-quality dataset from a full-field survey can be chosen as the reference baseline dataset for S-JMI to invert simultaneously together with the target seismic vintages. This aspect will be discussed with more details in Chapter 6.

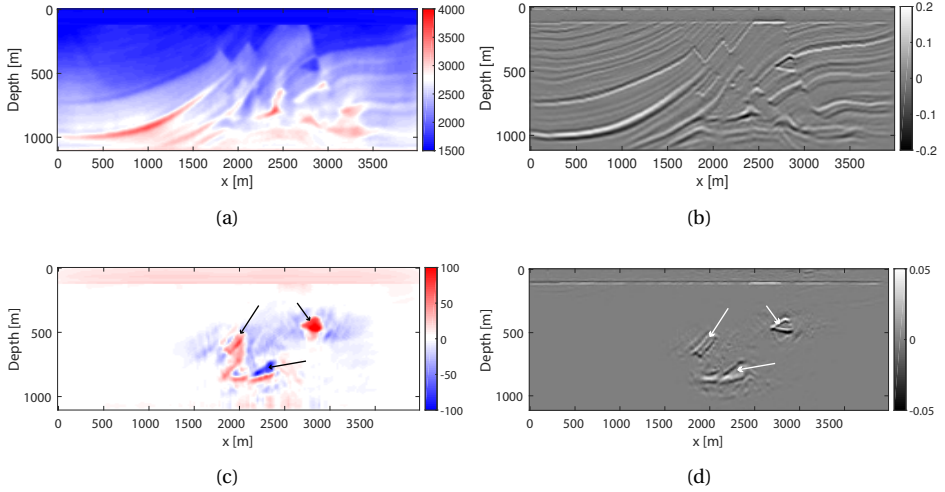


Figure 3.4: Marmoussi example: (a) and (b) the inverted baseline velocity and reflectivity model using HR-S-JMI; (c) and (d) the inverted time-lapse velocity- and reflectivity-difference using HR-S-JMI. The positions of the true time-lapse changes are pointed out with black and white arrows.

3.5.2. CONSTRAINT LINKING REFLECTIVITY AND VELOCITY UPDATE

Regarding the constraint that makes a link between reflectivity and velocity update, there is one step of approximating the correct scaling μ in equation 3.3. Currently, we simply calculate it linearly by balancing the energy of the estimated \mathbf{r}_{est} and \mathbf{r} , $\Delta\mathbf{r}_{est}$ and $\Delta\mathbf{r}$, which might lead to an unbalanced velocity contribution. One possible solution is to estimate a 2D spatially varying μ adaptively. More research will be done in the future to make it more robust.

3.6. CONCLUSION

In order to ensure the success of the conventional method based on a time-shift map and sequential JMI, the currently employed time-lapse acquisition practice is needed to exactly repeat well-sampled geometries to mitigate acquisition effects on the final time-lapse differences. Moreover, the independent process is always carefully tailored regarding some processing "tricks" to maximally reduce the non-repeatable uncertainties to the maximum. To relax these rigid requirements, a flexible and efficient method is needed.

We proposed a so-called (high-resolution-)S-JMI as a tool for reservoir monitoring. The simultaneous strategy of S-JMI reduces the non-repeatable uncertainties by fitting both datasets simultaneously and at the same time allows the baseline and monitor parameters to communicate and compensate with each other flexibly and dynamically during inversion. In order to obtain a more localized time-lapse velocity-difference, we extend the regular S-JMI to a robust HR-S-JMI process by adding two extra constraints on the velocity update — a directional total variation constraint and a time-lapse reflectivity-

difference constraint — during inversion. This time-lapse reflectivity-difference constraint elegantly connects reflectivity- and velocity-difference update by exploiting the relationship between them during inversion. In the end, one complex synthetic example based on marmousi model (the same time-lapse models described in Section 2.4) shows that (HR-)S-JMI is able to reliably recover the time-lapse effects in the reflectivity and velocity model. In particular, HR-S-JMI is capable of achieving a high-resolution velocity-difference.

REFERENCES

- [1] R. Arts, R. Elsayed, L. Van Der Meer, O. Eiken, S. Ostmo, A. Chadwick, G. Kirby, and B. Zinszner, *Estimation of the mass of injected CO₂ at Sleipner using time-lapse seismic data*, in *64th EAGE Conference & Exhibition* (2002).
- [2] R. Arts, O. Eiken, A. Chadwick, P. Zweigel, L. Van der Meer, and B. Zinszner, *Monitoring of CO₂ injected at Sleipner using time-lapse seismic data*, *Energy* **29** (2004), pp. 1383–1392.
- [3] A. Tura, T. Barker, P. Cattermole, C. Collins, J. Davis, P. Hatchell, K. Koster, P. Schutjens, and P. Wills, *Monitoring primary depletion reservoirs using amplitudes and time shifts from high-repeat seismic surveys*, *The Leading Edge* **24** (2005), pp. 1214–1221.
- [4] M. Trani, R. Arts, O. Leeuwenburgh, and J. Brouwer, *Estimation of changes in saturation and pressure from 4D seismic AVO and time-shift analysis*, *Geophysics* **76** (2011), pp. C1–C17.
- [5] P. Routh, G. Palacharla, I. Chikichev, and S. Lazaratos, *Full wavefield inversion of time-lapse data for improved imaging and reservoir characterization*, in *SEG Technical Program Expanded Abstracts 2012* (Society of Exploration Geophysicists, 2012) pp. 1–6.
- [6] A. J. Berkhout, *Combining full wavefield migration and full waveform inversion, a glance into the future of seismic imaging*, *Geophysics* **77** (2012), pp. S43–S50.
- [7] X. Staal and D. Verschuur, *Velocity estimation using internal multiples*, in *SEG Technical Program Expanded Abstracts 2012* (Society of Exploration Geophysicists, 2012) pp. 1–5.
- [8] X. R. Staal and D. J. Verschuur, *Joint migration inversion, imaging including all multiples with automatic velocity update*, in *75th EAGE Conference & Exhibition incorporating SPE EUROPEC 2013* (2013).
- [9] A. J. Berkhout, *Review paper: An outlook on the future of seismic imaging, Part III: Joint migration inversion*, *Geophysical Prospecting* **62** (2014), pp. 950–971.
- [10] D. J. Verschuur, X. R. Staal, and A. J. Berkhout, *Joint migration inversion: Simultaneous determination of velocity fields and depth images using all orders of scattering*, *The Leading Edge* **35** (2016), pp. 1037–1046.

- [11] F. Smit, J. Brain, and K. Watt, *Repeatability monitoring during marine 4D streamer acquisition*, in *67th EAGE Conference and Exhibition 2016* (Eur. Ass. of Geosc. and Eng., Expanded abstracts, 2005).
- [12] T. Watanabe, S. Shimizu, E. Asakawa, and T. Matsuoka, *Differential waveform tomography for time-lapse crosswell seismic data with application to gas hydrate production monitoring*, in *SEG Technical Program Expanded Abstracts 2004* (Society of Exploration Geophysicists, 2004) pp. 2323–2326.
- [13] D. Yang, M. Meadows, P. Inderwiesen, J. Landa, A. Malcolm, and M. Fehler, *Double-difference waveform inversion: Feasibility and robustness study with pressure data*, *Geophysics* **80** (2015), pp. M129–M141.
- [14] M. Maharramov, B. Biondi, and M. A. Meadows, *Time-lapse inverse theory with applications*, *Geophysics* **81** (2016), pp. R485–R501.
- [15] G. Ayeni and B. Biondi, *Target-oriented joint least-squares migration/inversion of time-lapse seismic data sets*, *Geophysics* **75** (2010), pp. R61–R73.
- [16] M. Maharramov and B. Biondi, *Joint full-waveform inversion of time-lapse seismic data sets*, in *SEG Technical Program Expanded Abstracts 2014* (Society of Exploration Geophysicists, 2014) pp. 954–959.
- [17] M. Maharramov and B. Biondi, *Robust simultaneous time-lapse full-waveform inversion with total-variation regularization of model difference*, in *77th EAGE Conference and Exhibition 2016* (Eur. Ass. of Geosc. and Eng., Expanded abstracts, 2015).
- [18] F. Oghenekohwo, H. Wason, E. Esser, and F. J. Herrmann, *Low-cost time-lapse seismic with distributed compressive sensing—part 1: Exploiting common information among the vintages*, *Geophysics* **82** (2017), pp. P1–P13.
- [19] H. Wason, F. Oghenekohwo, and F. J. Herrmann, *Low-cost time-lapse seismic with distributed compressive sensing—part 2: Impact on repeatability*, *Geophysics* **82** (2017), pp. P15–P30.
- [20] D. Verschuur and X. Staal, *Using primaries and multiples in time-lapse imaging and velocity estimation*, in *SEG Technical Program Expanded Abstracts 2014* (Society of Exploration Geophysicists, 2014) pp. 4955–4959.
- [21] S. Masaya and D. J. Verschuur, *Joint-migration inversion based on reflectivity-constrained velocity estimation*, in *SEG Technical Program Expanded Abstracts 2016* (2016).
- [22] S. Qu, E. Verschuur, and Y. Chen, *Full waveform inversion and joint migration inversion with an automatic directional total variation constraint*, *Geophysics* **84** (2018), pp. 1–37.
- [23] T. Goldstein and S. Osher, *The split Bregman method for L1-regularized problems*, *SIAM journal on imaging sciences* **2** (2009), pp. 323–343.

4

A REALISTIC SYNTHETIC EXAMPLE AND A FIELD DATA EXAMPLE

In this chapter, we demonstrate the effectiveness of high-resolution Simultaneous Joint Migration Inversion (HR-S-JMI) as a tool for reservoir monitoring with a highly realistic synthetic model based on the Grane field, offshore Norway, and a time-lapse field dataset from the Troll Field.

In the Grane field numerical example, we first investigate whether various time-lapse effects in this model, i.e. the reservoir time-lapse changes, the effects due to injection in the overburden, the weak stress-induced effects over the reservoir, and small water velocity perturbation, can be detected with S-JMI. Then, we compare the inverted results using S-JMI with those using a conventional time-lapse method based on creating a time-shift map and results from a sequential strategy based on JMI. Furthermore, we show that making a link between reflectivity and velocity update can help to achieve a more localized velocity update when there are not enough strong reflections around the target area helping the inversion of the velocity.

In the field data example based on a set of marine time-lapse data from the Troll Field, we show the effectiveness of HR-S-JMI in a real case where the repeatability of the time-lapse datasets is not very good.

4.1. SYNTHETIC DATA EXAMPLE BASED ON A REALISTIC TIME-LAPSE MODEL FROM THE GRANE FIELD

4.1.1. AN INTRODUCTION TO THE TIME-LAPSE MODEL

To investigate the feasibility of potential time-lapse inversion methods, [1] designed realistic time-lapse models based on the Grane field, offshore Norway provided by Equinor. In this work, we choose one 2D slice and the chosen time-lapse models are shown in Figures 4.1. The reflectivity and reflectivity-difference in Figures 4.1(e) and 4.1(f) are calculated from the density and velocity models. To make the model more realistic, the V_p model is roughened by adding relative velocity variations obtained from impedance contrasts from the seismic images. All the time-lapse effects are based on existing models and observations, including: production-related changes in the reservoir (gas-oil replacement), a small change in the shallow part of the water column, a local change in the overburden caused by waste injection, and a small stress-induced effect ($< 5m/s$) over the reservoir. [1] and [2] have already done investigations based on this model. They showed that full waveform inversion is capable of recovering production-related changes and local changes caused by waste injection with reasonable accuracy (although with lower resolution and amplitude than the true one). However, the changes in the water column and the small stress-induced effects are too small to be reliably recovered.

4.1.2. S-JMI AS AN EFFECTIVE TIME-LAPSE PROCESSING TOOL

The time-lapse datasets are generated via acoustic finite difference (FD) modeling using both the density and velocity model in Figure 4.1. The middle shot profile from the baseline and monitor datasets and their corresponding differences are shown in Figure 4.2. As we have mentioned before, current version of JMI cannot easily handle large-offset data due to the AVO effects. Therefore, a subset of the datasets with offsets from $-2500m$ to $2500m$ is used in this example. According to Ocean Bottom Node (OBN) acquisition, the source spacing is set to $25m$ and the receiver spacing to $100m$, although all the acquisitions were done at the surface. We use a Ricker wavelet with $20Hz$ peak frequency. Initial reflectivities are zero and the initial velocity model is a very simple vertical gradient with water-layer information (shown in Figures 4.3). The band-width of frequency during JMI is $5Hz - 40Hz$. In addition, 20% random noise energy is added to the datasets. Table 4.1 shows a list of acquisition and inversion parameters used in the Grane example.

Table 4.1: Grane example: a list of acquisition and inversion parameters.

Modeling method	Band-width	Surface/Internal multiples	Random noise	Wavelet	Source arrangement	Receiver arrangement	Other
Acoustic FD	5 – 40Hz	No/Yes	20%	Ricker, 20Hz peak freq.	0 – 9000m with 25m spacing at $z = 0m$	0 – 9000m with 100m spacing at $z = 0m$	Only use offsets upto $\pm 2500m$

In this subsection, we compare three strategies: (1) sequential JMI, (2) S-JMI, (3) a conventional time-lapse strategy based on a time-shift map.

For the first strategy — sequential JMI, the inverted baseline reflectivity and velocity using JMI are shown in Figures 4.4(a) and 4.4(b). Because of the inversion process in-

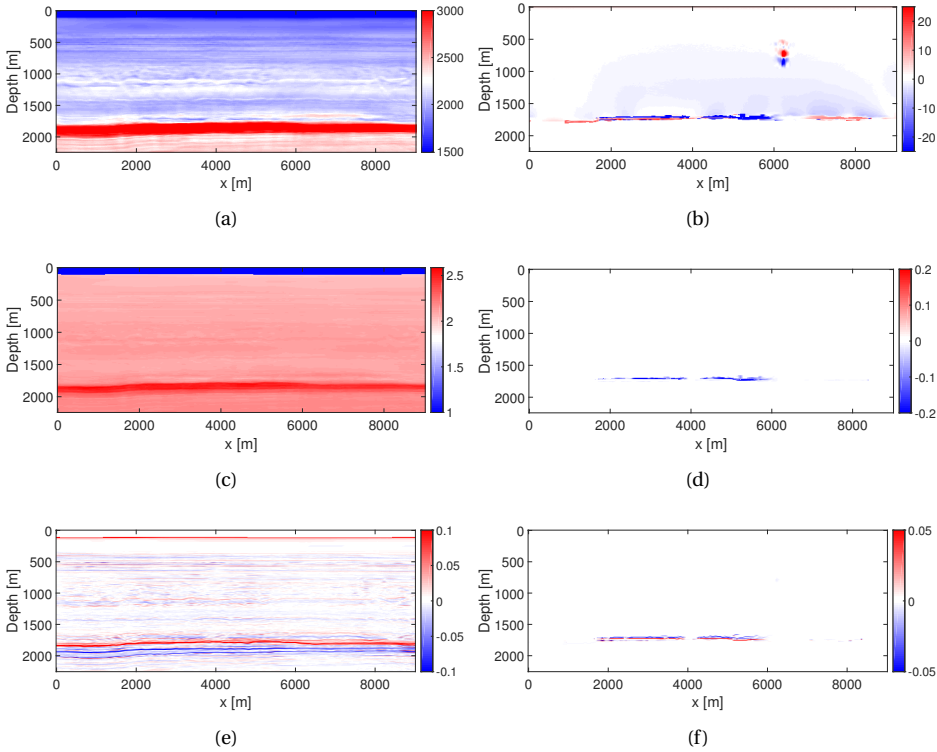


Figure 4.1: Grane example: (a) and (b) true baseline velocity and time-lapse velocity-difference; (c) and (d) true baseline density and time-lapse density-difference; (e) and (f) true baseline reflectivity and time-lapse reflectivity-difference.

cluded in JMI, all the inverted images are quite accurate and the estimated velocity models also exhibit some details. The red-blobs in Figure 4.4(a) are due to the edge effects. In terms of time-lapse differences, the inverted velocity in Figure 4.4(c) can provide some time-lapse information, but they are quite noisy. The inverted reflectivity model 4.4(d) also shows noisy time-lapse effects. For the latter comparison purpose, during this sequential JMI process, illumination preconditioning and smoothing of the gradients are included (results are shown in Figures 4.4(c) and 4.4(d)). As was mentioned before, this independent strategy is sensitive to various processing "tricks", which increase the uncertainties during process. We show an extra scenario where illumination preconditioning and smoothing of gradients are excluded during sequential JMI. The results are shown in Figures 4.4(e) and 4.4(f). It can be seen that more clear time-lapse differences are achieved.

For the second strategy — S-JMI, the baseline results are shown in Figures 4.5(a) and 4.5(b). Afterwards, from the inverted baseline results and some information about injection wells, we get to know the approximate position of the reservoir and injection point,

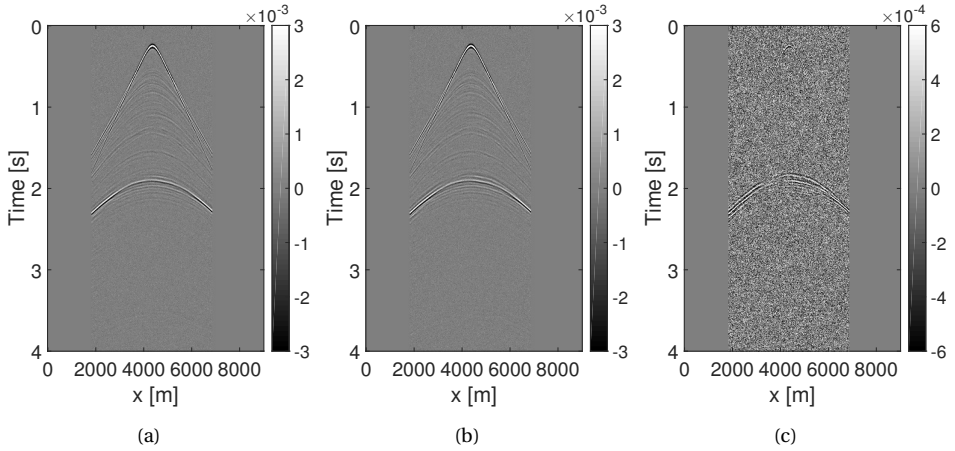


Figure 4.2: Grane example: the middle shot profile at $X = 4500\text{m}$ from the baseline data (a), from the monitor data (b), and (c) the difference between (a) and (b), displayed with a different amplitude scale.

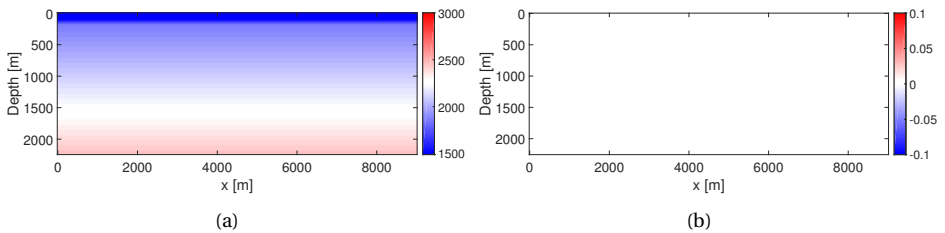


Figure 4.3: Grane example: (a) and (b) initial velocity and reflectivity model.

based on which the spatial weighting operators used in S-JMI are designed and shown in Figures 4.5(c) and 4.5(d). Despite reservoir changes, we also consider changes due to pressure perturbation and injection for the velocity spatial weighting operator design. For the reflectivity model, we use a more strict spatial weight by ignoring them. Regarding the time-lapse differences, by using S-JMI instead of inverting each dataset independently, much better results are achieved for both reflectivity and velocity model, shown in Figures 4.5(e) and 4.5(f). Note that the processing 'tricks', e.g. illumination preconditioning and smoothing of the gradients, are included in S-JMI. The image-difference in the reservoir is very clear with reliable amplitudes located at the correct position, which means the travel-time (propagation) has been well explained via the velocity update. The production-related velocity changes in the reservoir, local changes in the overburden due to injection, and water-layer changes are all reasonably recovered, albeit not with as good resolution and amplitude as the true time-lapse effects. They look somewhat smeared, because there are no strong reflections helping to make the velocity update localized, while

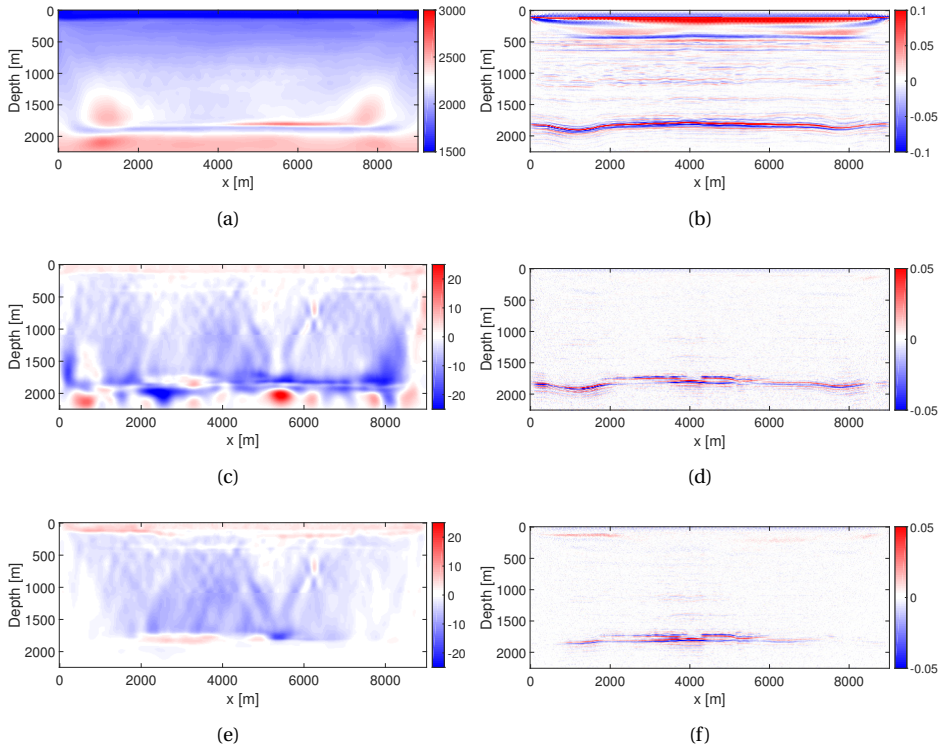


Figure 4.4: Grane example: (a) and (b) the inverted baseline velocity and reflectivity using sequential JMI; (c) and (d) the inverted time-lapse velocity- and reflectivity-difference using sequential JMI including illumination preconditioning and smoothing of gradients; (e) and (f) the inverted time-lapse velocity- and reflectivity-difference using sequential JMI excluding illumination preconditioning and smoothing of gradients.

the velocity parameter can only explain propagation effects in the data. The current inverted velocity model is good enough to explain the propagation effects, which means the vertical integral of this smooth velocity difference is almost equal to the integral of the true one. Besides, the small stress-induced effect over the reservoir is mixed with the unlocalized reservoir-related time-lapse changes and cannot be distinguished.

Now, we show the third strategy — the conventional time-lapse strategy based on a time-shift map. The monitor image is inverted using FWM with the same baseline velocity model inverted using JMI shown in Figure 4.4(a). This inverted monitor image in Figure 4.6(a) and the inverted baseline image in Figure 4.4(b) are then used to calculate the time-shift map, which is shown in Figure 4.6(b). Finally, the velocity difference can be calculated from this time-shift map and is shown in Figure 4.6(c). It can be seen that this velocity-difference is a very coarse indicator of the actual velocity changes with low resolution and accuracy. The shifted image difference realigned with the time-shift map is

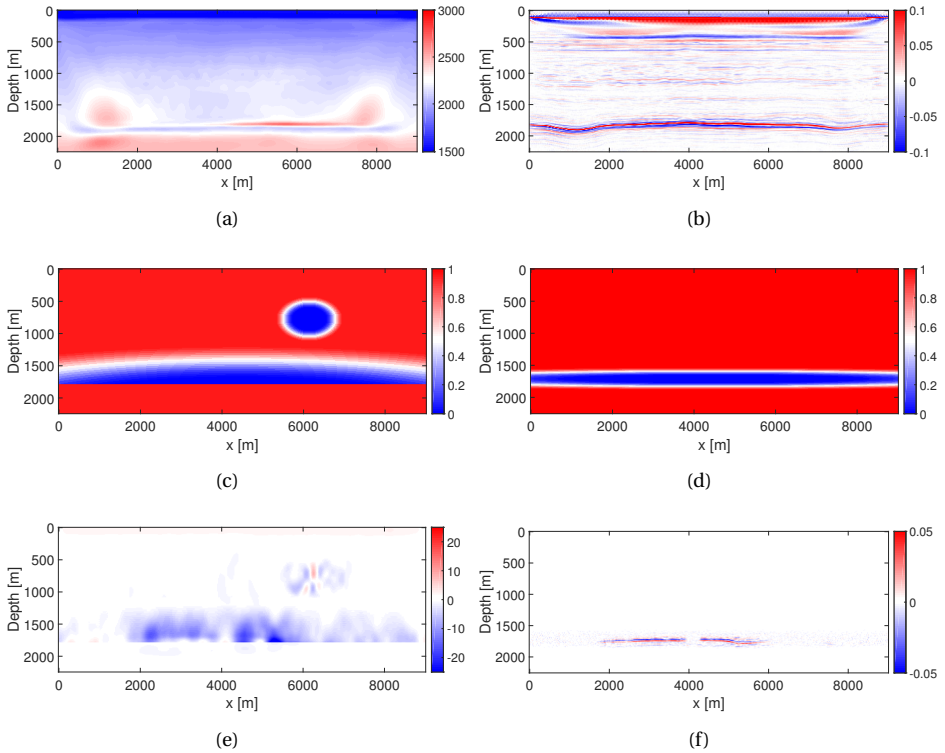


Figure 4.5: Grane example: (a) and (b) the inverted baseline velocity and reflectivity using S-JMI; (c) and (d) the spatial weighting operators for velocity and reflectivity; (e) and (f) the inverted time-lapse velocity- and reflectivity-difference using S-JMI.

shown in Figure 4.6(d). We can see that the shifted time-lapse image difference is of quite good quality, because this time-lapse model satisfies the "1D assumption" requirement of this conventional method based on the time-shift map. To some extent, the conventional method serves its purpose, as it is able to indicate the time-lapse reflectivity difference as well as S-JMI. However, it fails to indicate the time-lapse velocity change accurately. Therefore, S-JMI is a more effective tool for reservoir monitoring compared to the conventional time-shift strategy.

4.1.3. MORE LOCALIZED TIME-LAPSE CHANGES BROUGHT BY HIGH-RESOLUTION S-JMI

As we have seen from the previous subsection, in S-JMI, the velocity can only explain propagation effects in the data and look somehow smeared, the high-frequency components of velocity are hidden in the reflectivities. However, for time-lapse processing workflow, high-resolution time-lapse velocity difference is usually a demand.

Therefore, in this subsection, we will show that HR-S-JMI, which connects the reflectivity-

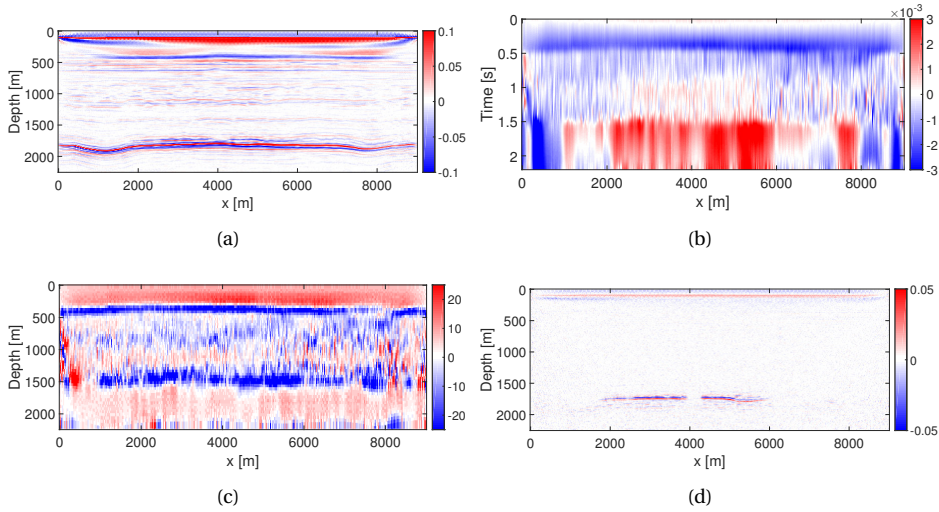


Figure 4.6: Grane example: results using the conventional time-shift-based method: (a) the inverted monitor reflectivity model using FWM with the baseline velocity model in Figure 4.4(a); (b) the estimated time-shift map from the inverted images in Figures 4.6(a) and 4.4(b); (c) and (d) the calculated time-lapse velocity-difference and shifted reflectivity-difference based on the time-shift map.

and velocity-difference by exploiting the relationship between them, can lead to a high-resolution time-lapse velocity. In the Grane model, there are insufficient strong reflections around the target area so it is difficult to obtain a localized velocity-difference using the regular S-JMI.

The inverted baseline results by using HR-S-JMI are shown in Figures 4.7(a) and 4.7(b). More fine details can be seen in Figure 4.7(a) due to the link between the velocity and reflectivity updates together with the directional Total Variation regularization in HR-S-JMI. Regarding the inverted reflectivity, since the inverted velocity using regular S-JMI is already able to explain the propagation effects very well, an inverted velocity model with fine details does not obviously improve the reflectivity result. The inverted time-lapse differences obtained by using HR-S-JMI are shown in Figures 4.7(c) and 4.7(d). The inverted velocity-difference has higher resolution compared to Figure 4.5(e). Figures 4.8 shows a comparison of velocity-difference using different methods at two different lateral locations, $X = 3100m$ and $X = 4700m$. We can see that the inverted velocity-difference using regular S-JMI (red line) looks smeared compared to the true differences (blue line). By linking the baseline reflectivity and velocity, reflectivity- and velocity-difference, HR-S-JMI leads to higher-resolution results (yellow line). However, as was mentioned before, a more localized velocity-difference does not make much difference for the inverted reflectivity-difference.

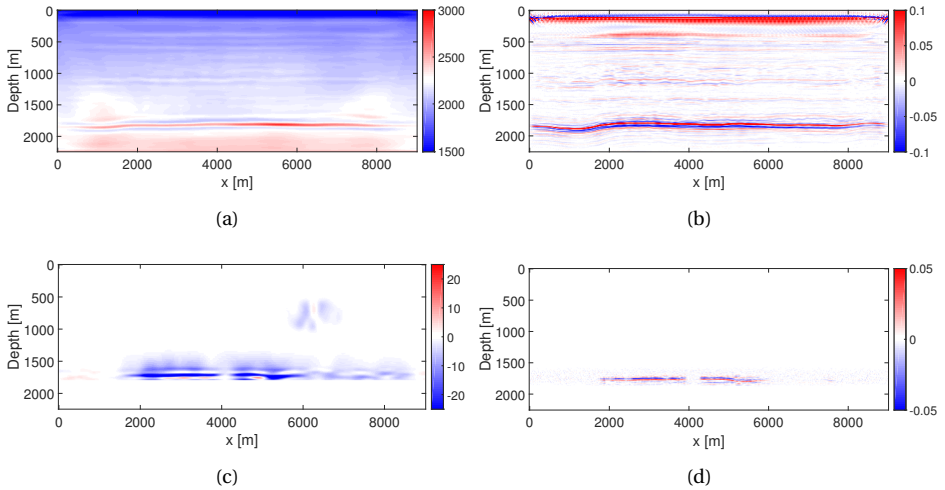


Figure 4.7: Grane example: (a) and (b) the inverted baseline velocity and reflectivity using HR-S-JMI; (c) and (d) the inverted time-lapse velocity- and reflectivity-difference using HR-S-JMI.

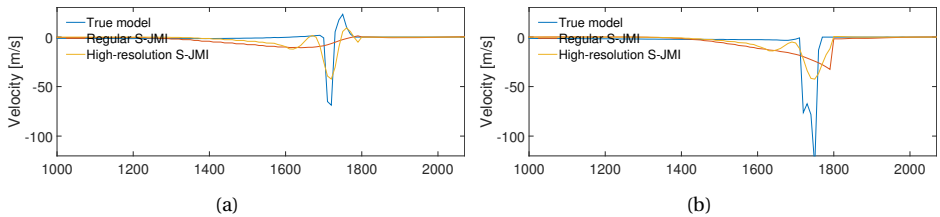


Figure 4.8: Grane example: comparison of the inverted velocity-difference using different methods at (a) $X = 3100m$ and (b) $X = 4700m$.

4.2. FIELD DATA EXAMPLE BASED ON THE MARINE TIME-LAPSE DATASETS OF THE TROLL FIELD

In this section, with one field data example based on a set of marine time-lapse datasets from the Troll Field provided by Equinor, we will show the feasibility of the proposed method in a real case, where the repeatability of the time-lapse datasets is not very good.

The offshore Troll Field is located west of Norway. In this example, only a part from the available seismic survey is selected. A 2D baseline streamer survey was acquired in 1997 (Figure 4.9(a)) and its response is compared to a 2D monitor streamer survey acquired in 2002 (Figure 4.9(b)). The difference of seismic records between the two surveys is displayed in Figure 4.9(c). First of all, several preprocessing steps are applied to both datasets. One of these steps is near-trace interpolation using the parabolic Radon transformation [3]. The near-offset gap to be interpolated was approximately 85m. Another

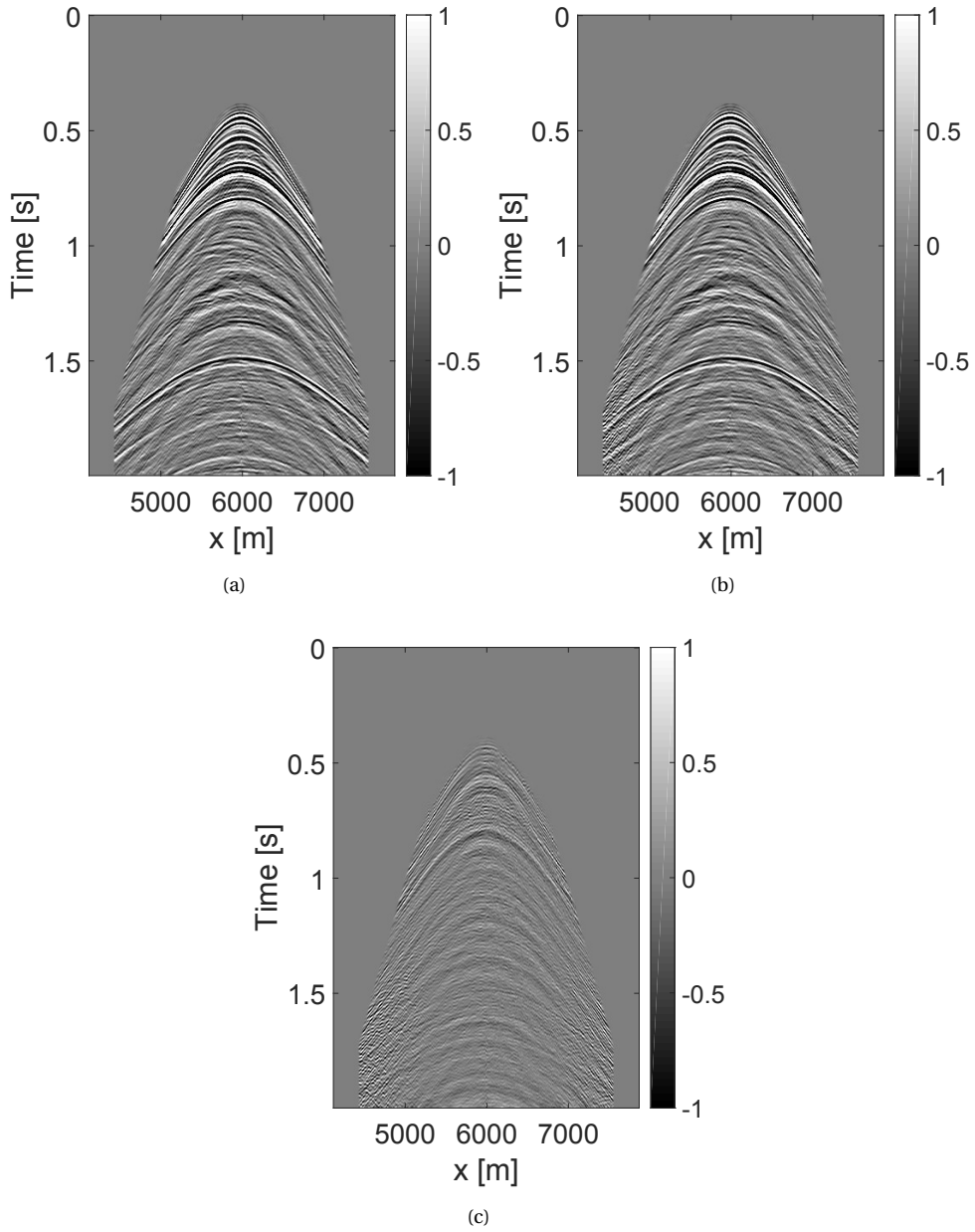


Figure 4.9: Troll example: a seismic record from the baseline data (a), same seismic record from the monitor data (b), and (c) the data difference between (a) and (b).

preprocessing step is pre-stack surface-related multiple elimination to reduce interfering multiples with reservoir reflections [4]. In addition, both source and receiver spacing is regularized to 12.5m for the streamer surveys, such that split-spread shot records can be constructed. In this example, however, only the sub-datasets with a source spacing of 50m are used for the inversion in order to accelerate the calculation. Note that we can see that there are high values almost everywhere in the data difference in Figure 4.9(c), and it is hard to distinguish where the time-lapse effects from the reservoir-related region, which means that the non-repeatability introduced by acquisition or preprocessing is quite an issue.

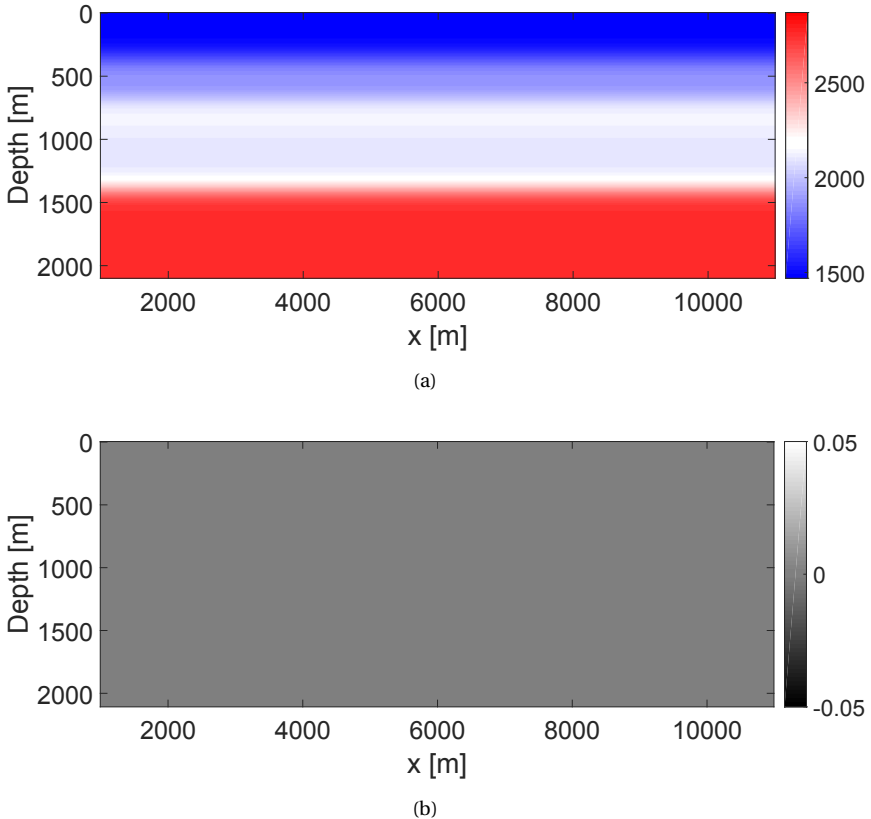


Figure 4.10: Troll example: (a) and (b) the initial velocity and reflectivity model.

The initial velocity model is estimated using NMO analysis (Figure 4.10(a)) and the initial reflectivities are zero (Figure 4.10(b)). The stack image in time from the baseline data based on the initial velocity is shown in Figure 4.11(a) and its corresponding difference with the monitor stack image is shown in Figure 4.11(b). The time-lapse changes on the stack image-difference are also not very obvious due to the non-repeatability issue. According to [5], there is one hydrocarbon and water contact around 1.7s, which is pointed by a black arrow in Figure 4.11(b). This hydrocarbon is gas with an underlying oil leg vary-

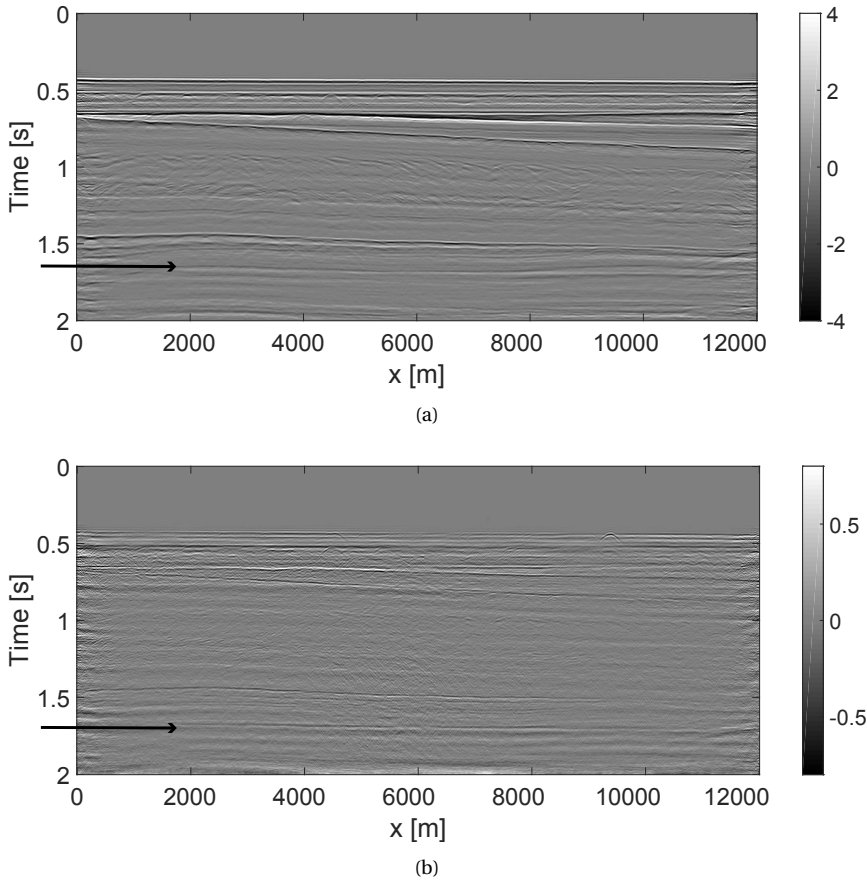


Figure 4.11: Troll example: (a) the baseline stack image in time and (b) its corresponding time-lapse difference. The arrow indicates the reservoir.

ing in thickness from 0 to 28m. The wavelet spectrum used in the inversion is estimated by summing together all the shot gathers at $k = 0$ in the f-k domain. The band-width of frequency during S-JMI is 5Hz – 40Hz.

The inverted baseline velocity and reflectivities are shown in Figures 4.12(a) and 4.12(b). Because of the inversion process included in JMI, the inverted image is quite accurate, even though there are some distortions near the boundaries because of the aperture effect. Due to making a link between the reflectivity and velocity update, the estimated velocity models also exhibit some details. From the inverted baseline results and some prior information, we get to know the approximate position of the reservoir, based on which the spatial weighting operators used in S-JMI are designed and shown in Figures 4.13(a) and 4.13(b). The final inverted time-lapse differences are shown in Figures 4.14(a) and 4.14(b). Both the time-lapse reflectivity and velocity are reasonably recovered. The reflectivity difference is very clear and the velocity time-lapse effect can also be clearly distinguished.

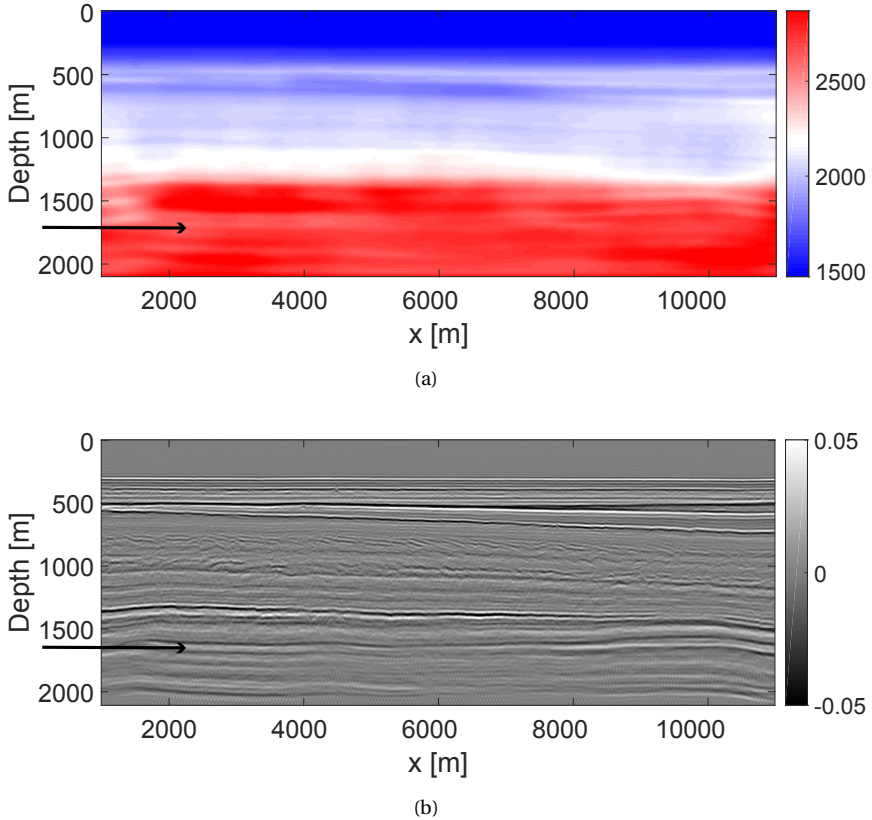


Figure 4.12: Troll example: (a) and (b) the inverted baseline velocity and reflectivities. The arrow indicates the reservoir.

Note that the conventional time-lapse strategy based on a time-shift map, such as demonstrated in Figure 2.13, was also applied to these data, however, it was not working due to the severe acquisition and pre-processing discrepancy.

4.3. CONCLUSION

We show one realistic synthetic example and one field data example to demonstrate the effectiveness of HR-S-JMI as a tool for reservoir monitoring. Regarding the realistic synthetic example, we use a synthetic time-lapse model based on the Grane field offshore Norway. HR-S-JMI is able to reliably recover the time-lapse effects in the reflectivity model and also get a high-resolution inverted time-lapse velocity-difference. Regarding the field data example, a set of marine field data from the Troll Field in the North Sea is used. Both the time-lapse reflectivity- and velocity-difference are reasonably recovered via HR-S-JMI, even though the repeatability of these time-lapse datasets is not good.

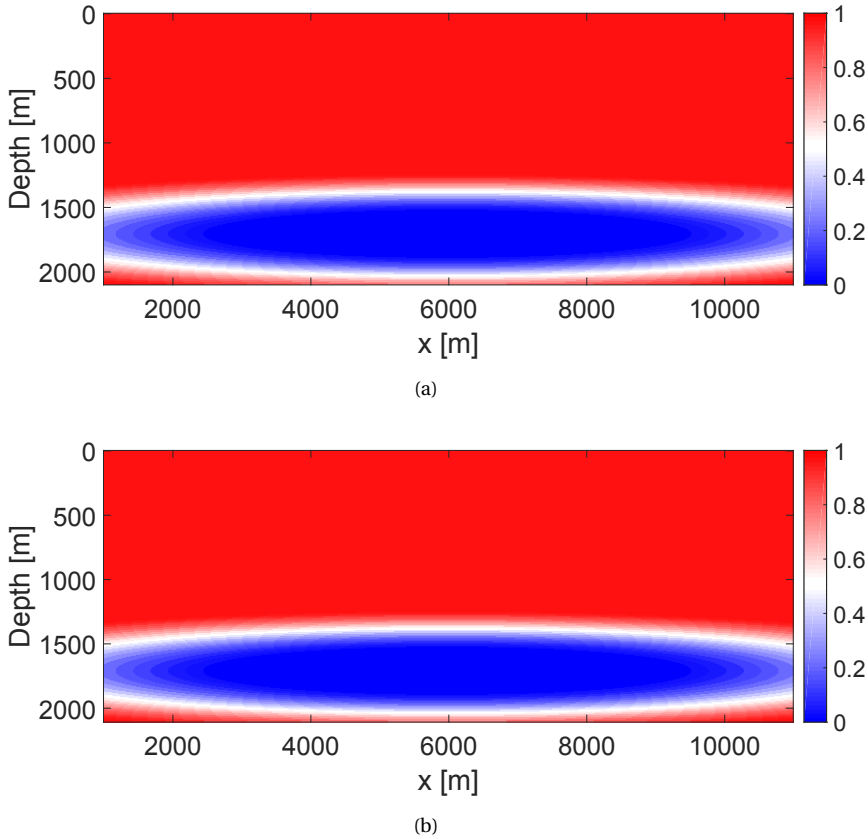


Figure 4.13: Troll example: (a) and (b) the spatial weighting functions for velocity and reflectivities during S-JMI.

4.4. ACKNOWLEDGMENT

We thank Equinor, CGG, and the Grane license partners Petoro AS, ExxonMobil E&P Norway AS and ConocoPhillips Skandinavia AS, for the release of the Grane synthetic velocity model. The views and opinions expressed in this work are those of the authors and not necessarily shared by Equinor ASA, CGG, and the Grane license partners. We thank Equinor for providing the marine time-lapse datasets of the Troll Field.

REFERENCES

- [1] S. P. Lescoffit, M. Houbiers, C. Henstock, E. Hicks, K. M. Nilsen, H. Hoerber, A. Ratcliffe, and V. Vinje, *Time-lapse full-waveform inversion applied to permanent reservoir monitoring data from Grane, a Norwegian North Sea field*, in *SEG Technical Program Expanded Abstracts 2016* (Society of Exploration Geophysicists, 2016) pp. 1304–1308.

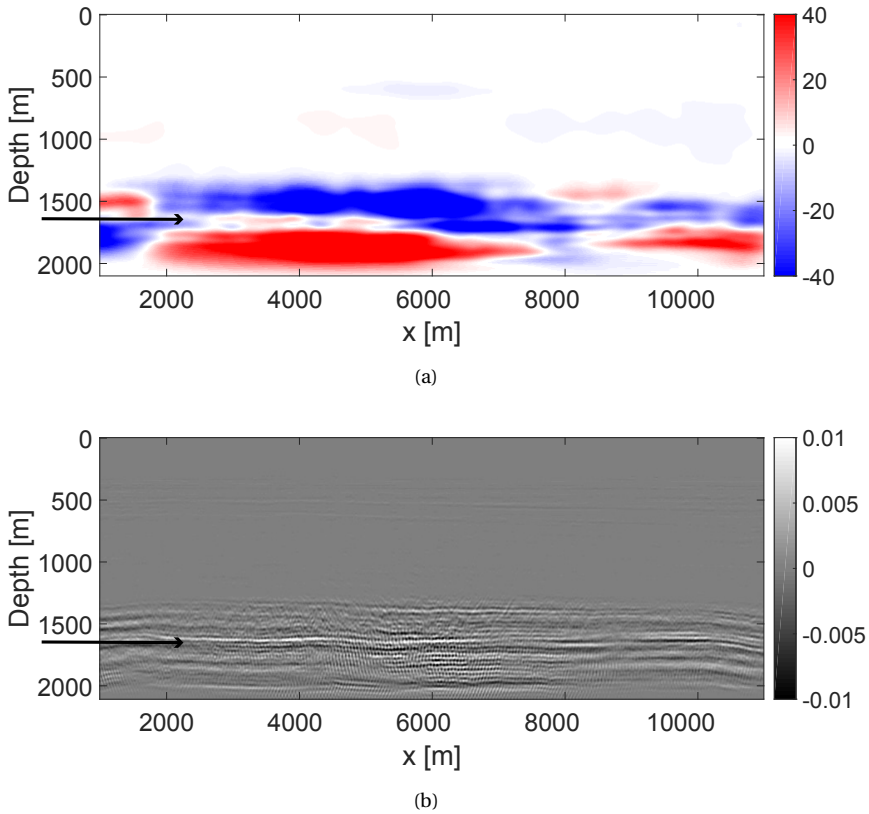


Figure 4.14: Troll example: (a) and (b) the inverted velocity and reflectivity differences. The arrow indicates the reservoir.

- [2] E. Hicks, H. Hoerber, M. Houbiers, S. P. Lescoffit, A. Ratcliffe, and V. Vinje, *Time-lapse full-waveform inversion as a reservoir-monitoring tool - North Sea case study*, *The Leading Edge* **35** (2016), pp. 850–858.
- [3] M. M. N. Kabir and D. J. Verschuur, *Restoration of missing offsets by parabolic Radon transform*, *Geophysical Prospecting* **43** (1995), pp. 347–368.
- [4] D. J. Verschuur, A. J. Berkhou, and C. P. A. Wapenaar, *Adaptive surface-related multiple elimination*, *Geophysics* **57** (1992), pp. 1166–1177.
- [5] J. R. Johnsen, H. Rutledal, and D. E. Nilsen, *Jurassic reservoirs; field examples from the Oseberg and Troll fields: Horda Platform area*, in *Norwegian Petroleum Society Special Publications*, Vol. 4 (Elsevier, 1995) pp. 199–234.

5

FEASIBILITY AND ROBUSTNESS STUDY

In the previous chapters, high-resolution Simultaneous Joint Migration Inversion (HR-S-JMI), which combines a simultaneous time-lapse data processing strategy with the Joint Migration Inversion method, has been proposed as an effective time-lapse processing tool for reservoir monitoring. In order to investigate the feasibility of using HR-S-JMI in practice, some numerical experiments are conducted to test the dependence of HR-S-JMI on the quality of the time-lapse datasets including the following aspects: noise, including random noise and coherent noise caused by the acoustic assumption; the quality of time-lapse surveys, including sparse surveys, non-repeated surveys, and Ocean Bottom Node (OBN) vs streamer (sparse and non-repeated time-lapse surveys); non-repeated sources, including source positioning errors and non-repeated source wavelets. Moreover, its robustness to the L2-norm constraints based on spatial weighting operators and sensitivity to weak time-lapse effects are also tested.

All the experiments are carried on with a highly realistic synthetic time-lapse model based on the Grane field offshore Norway described in Section 4.1.

5.1. NOISE

In this section, two experiments are employed to investigate whether HR-S-JMI is robust enough to handle two types of noise: random noise and coherent noise caused by the acoustic assumption in JMI.

5.1.1. RANDOM NOISE

The time-lapse datasets are generated via acoustic finite difference (FD) modeling using both the density and velocity model shown in Figure 4.1. The associated acquisition and inversion settings are listed in Table 5.1 and the initial models were already shown in Figure 4.3. Random noise is added with random amplitude and phase in the frequency domain. The noise level can be expressed as the overall energy ratio between the noise and signals of the entire shot gather:

$$\text{Noiselevel} = \frac{\sum_{i=0}^{N-1} \sum_{j=0}^{M-1} n_{i,j}^2}{\sum_{i=0}^{N-1} \sum_{j=0}^{M-1} d_{i,j}^2} \cdot 100\%, \quad (5.1)$$

where M and N are the numbers of traces and shots respectively, and $n_{i,j}^2$ and $d_{i,j}^2$ are the noise energy and signal energy of i^{th} shot and j^{th} trace. The following noise levels are considered in this experiment: 20%, 60%, 100%, and 200%. Figure 5.1 displays a near-offset trace of baseline and monitor data difference with different random noise energy. Figure 5.2 shows the final inverted baseline results using HR-S-JMI. Because of the inver-

Table 5.1: Random noise: a list of acquisition and inversion parameters.

Modeling method	Bandwidth	Surface/Internal multiples	Random noise	Wavelet	Source arrangement	Receiver arrangement	Other
Acoustic FD	5 – 40Hz	No/Yes	20%, 60%, 100%, 200%	Ricker, 20Hz peak freq.	0 – 9000m with 25m spacing at $z = 0m$	0 – 9000m with 100m spacing at $z = 0m$	Only use offsets upto $\pm 2500m$

sion process included in JMI, all the inverted results capture the main geological features and the artifacts introduced by the random noise are barely visible. The time-lapse reflectivity and velocity changes are shown in Figure 5.3. It can be seen that HR-S-JMI is very robust to random noise, although the resulting differences are contaminated by the noise in proportion to its energy level. In particular, HR-S-JMI is able to give reasonable time-lapse differences, even when the random noise energy is twice as the signal energy (200%) being shown in Figures 5.3(g) and 5.3(h). Its robustness to the random noise can be attributed to both the inversion process in JMI and the simultaneous strategy, which gets use of all the datasets during inversion.

5.1.2. COHERENT NOISE CAUSED BY THE ACOUSTIC ASSUMPTION

In this experiment, the impact of coherent noise caused by the acoustic assumption on the effectiveness of HR-S-JMI is tested. The time-lapse datasets are generated via elastic finite difference modeling using both the density, P-wave velocity, and S-wave velocity. The density and P-wave velocity models were already shown in Figures 4.1(a)-4.1(d). The

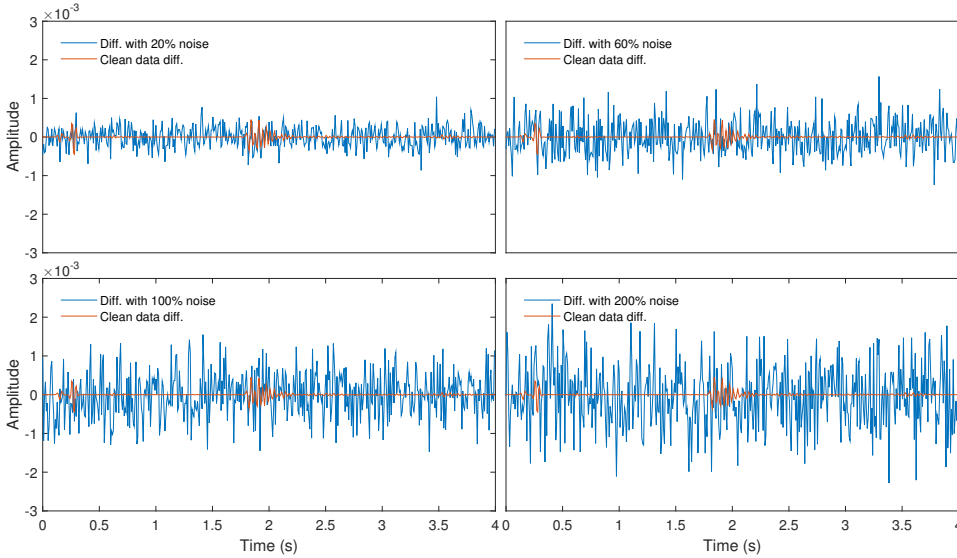


Figure 5.1: Random noise: a near-offset trace of the difference between baseline and monitor datasets, with 0%, 20%, 60%, 100%, and 200% random noise energy.

S-wave velocity and S-wave velocity-difference are shown in Figure 5.4. Figure 5.5 displays a near-offset trace of clean elastic and acoustic modeled data difference, and elastic data difference with 20% random noise energy. We can see a small amplitude misfit between acoustic and elastic data difference and this small misfit is overwhelmed by the 20% random noise. The related acquisition and inversion settings are listed in Table 5.2. The time-lapse reflectivity and velocity changes inverted using HR-S-JMI with the acoustic assumption are shown in Figure 5.6, which are almost as good as the results from acoustic data in Figures 5.3(a) and 5.3(b). Therefore, HR-S-JMI is robust to the mild coherent noise caused by the acoustic assumption in this example.

Table 5.2: Coherent noise: a list of acquisition and inversion parameters.

Modeling method	Band-width	Surface/Internal multiples	Random noise	Wavelet	Source arrangement	Receiver arrangement	Other
Elastic FD	5 – 40 Hz	No/Yes	20%	Ricker, 20 Hz peak freq.	0–9000 m with 25 m spacing at $z = 0$ m	0–9000 m with 100 m spacing at $z = 0$ m	Only use offsets upto ± 2500 m

5.2. QUALITY OF TIME-LAPSE SURVEYS

In this section, three experiments regarding the quality of the time-lapse monitoring surveys are conducted to investigate the ability of HR-S-JMI to handle sparse surveys, non-repeated surveys (interleaved surveys), and different types of surveys — OBN vs streamer, which is sparse and at the same time non-repeated monitoring.

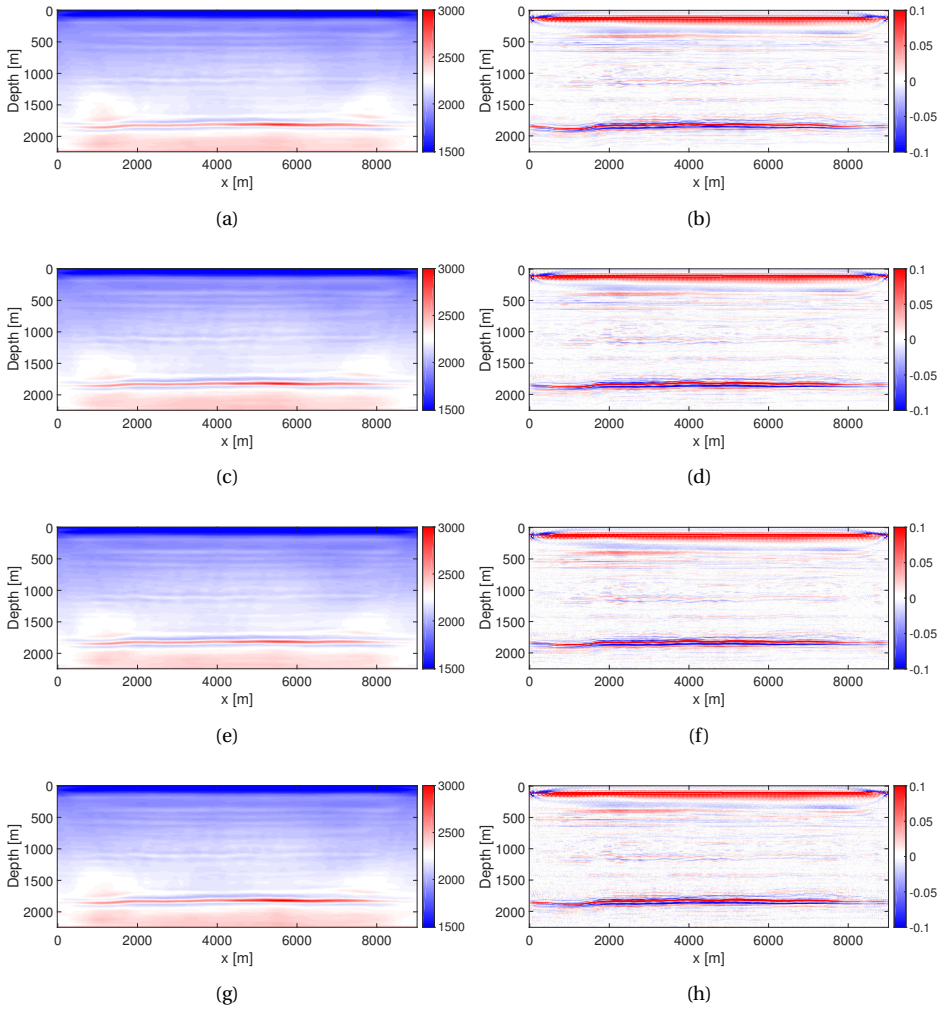


Figure 5.2: Random noise: the inverted baseline velocity and reflectivity model from the datasets with 20% (a) and (b), 60% (c) and (d), 100% (e) and (f), 200% (g) and (h) random noise energy level.

5.2.1. SPARSE SURVEYS

Sparse spatial survey design is usually desired in the context of frequent monitoring due to its cost-effectiveness. In this experiment, we assume both baseline and monitor datasets are generated with a source spacing as $50m$ and receiver spacing as $200m$. Compared to the previous experiments, only one fourth of the datasets remains used. The related acquisition and inversion settings are shown in Table 5.3.

The baseline inverted results using HR-S-JMI starting from the initial models in Fig-

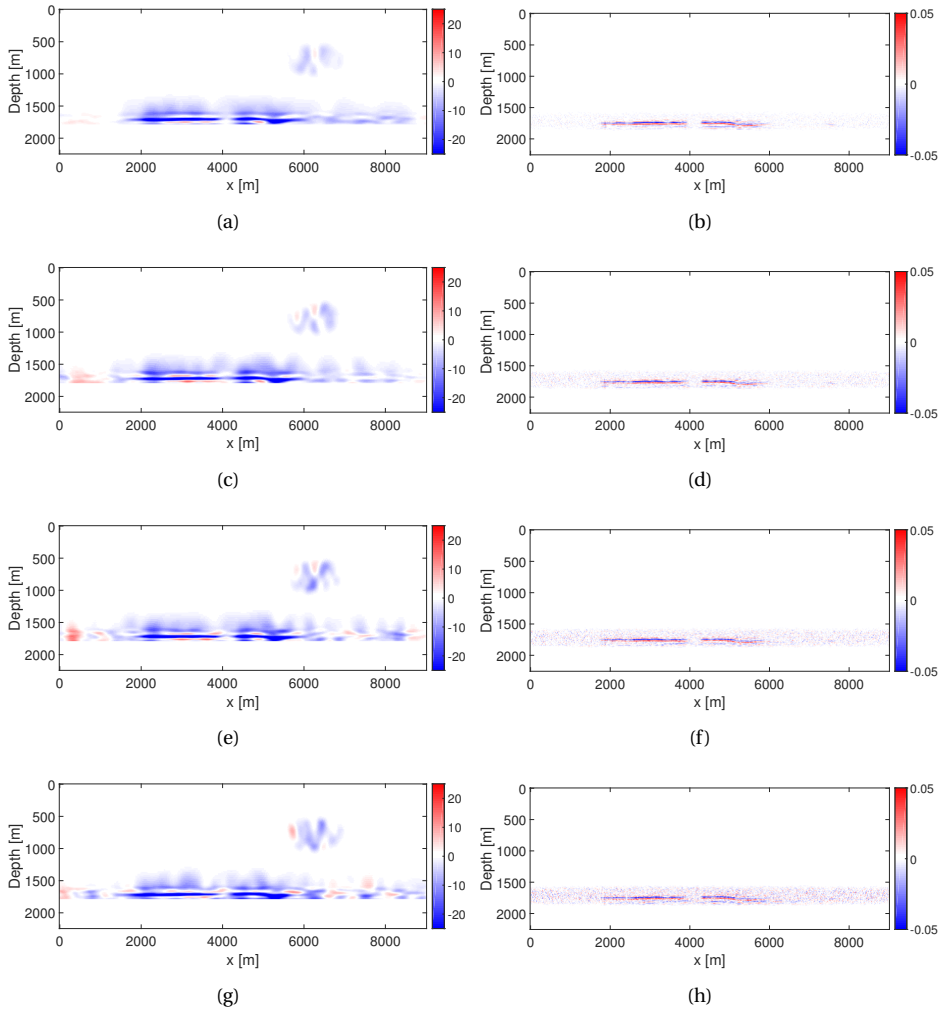


Figure 5.3: Random noise: the inverted time-lapse velocity- and reflectivity-differences from the datasets with 20% (a) and (b), 60% (c) and (d), 100% (e) and (f), 200% (g) and (h) random noise energy level.

ures 4.3 are shown in Figures 5.7(a) and 5.7(b). Most geological features are reasonably captured. Compared to the results using dense data in Figures 5.2(a) and 5.2(b), the inverted velocity model is noisier and the inverted reflectivities have weaker amplitude and are less focusing due to insufficient illumination. The final time-lapse differences are shown in Figures 5.7(c) and 5.7(d). It can be seen that the reservoir-related time-lapse effects and the local change due to injection are all very well recovered. However, some artifacts due to the sparsity of data are visible, although they are not strong enough to cover

Table 5.3: Sparse surveys: a list of acquisition and inversion parameters.

Modeling method	Band-width	Surface/Internal multiples	Random noise	Wavelet	Source arrangement	Receiver arrangement	Other
Acoustic FD	5 – 40Hz	No/Yes	20%	Ricker, 20Hz peak freq.	0 – 9000m with 50m spacing at $z = 0m$	0 – 9000m with 200m spacing at $z = 0m$	Only use offsets upto $\pm 2500m$

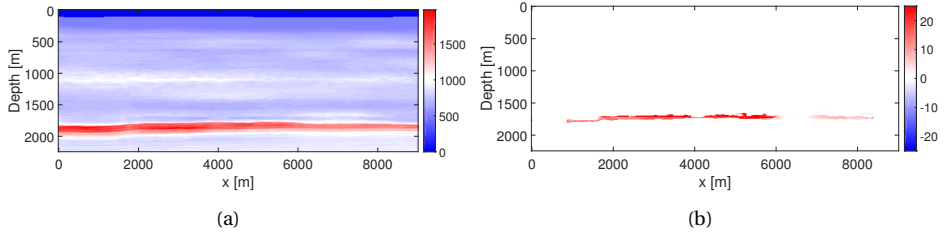


Figure 5.4: Coherent noise: (a) and (b) the true baseline S-wave velocity and S-wave velocity-difference.

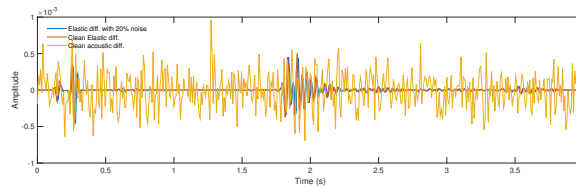


Figure 5.5: Coherent noise: a near-offset trace of clean elastic and acoustic modeled data difference and elastic data difference with 20% random noise energy.

up the actual time-lapse effects. Therefore, HR-S-JMI is very robust to sparse time-lapse acquisition surveys, which makes a valuable feature for frequent monitoring.

5.2.2. NON-REPEATED SURVEYS

In this subsection, the robustness of HR-S-JMI to mild non-repeatability issue of time-lapse surveys is tested. Both baseline and monitor datasets are generated with a source spacing as 25m and receiver spacing as 100m. However, the first receiver of the baseline starts at $x = 0m$, while the first receiver of the monitor starts at $x = 50m$. In this case, the illumination of both surveys are almost the same. This type of monitoring surveys is termed interleaved surveys. Please note that the interleaved surveys may not be realistic in this case, assuming that receivers are permanently deployed, however, it still helps to show the idea that HR-S-JMI is suitable to the case of non-repeated geometries. The related acquisition and inversion settings are shown in Table 5.4. Figure 5.8 shows the inverted time-lapse changes based on interleaved monitoring surveys, which are almost as good as using repeated surveys in Figures 5.3(a) and 5.3(b). Therefore, HR-S-JMI is able to handle the datasets from moderately changed monitoring geometries, in which the illuminations

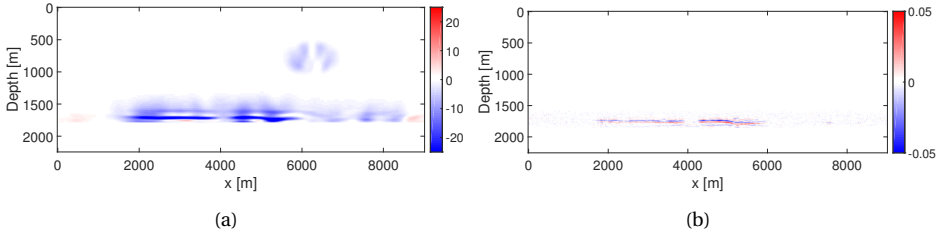


Figure 5.6: Coherent noise: (a) and (b) the inverted time-lapse velocity- and reflectivity-difference from data modeled with elastic finite difference modeling.

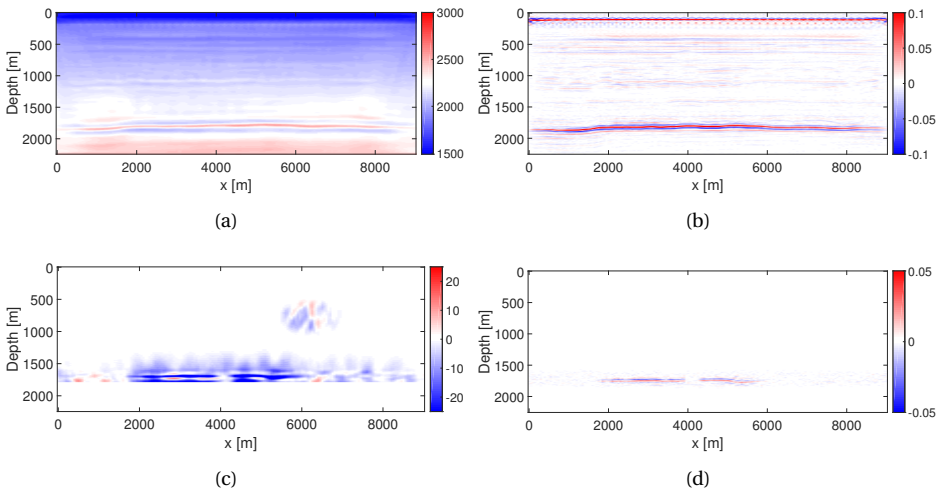


Figure 5.7: Sparse surveys: (a) and (b) the inverted baseline velocity and reflectivity model; (c) and (d) the inverted time-lapse velocity- and reflectivity-difference.

of both surveys are similar.

5.2.3. SPARSE AND NON-REPEATED SURVEYS — OBN VS STREAMER

In this experiment, we show a specific case of sparse and non-repeated surveys — Ocean Bottom Node (OBN) vs streamer acquisition. For the baseline survey, which is designed according to sparse OBN survey, the receivers are employed on the ocean-bottom ($z = 120m$) with a spacing of $200m$ and sources are on the surface ($z = 0m$) with a spacing of $50m$. For the monitor survey based on a streamer survey, both receivers and sources are located on the surface ($z = 0m$) with a spacing of $50m$. Note that, the sources are designed in the same way in both surveys.

In order to minimize the influence of acquisition geometry discrepancy during process, we first forward-propagate the sources to the ocean-bottom level (virtual sources are on the ocean-bottom level now) and back-propagate the measured wavefields from

Table 5.4: Interleaved surveys: a list of acquisition and inversion parameters.

Modeling method	Band-width	Surface/Internal multiples	Random noise	Wavelet	Source arrangement	Receiver arrangement	Other
Acoustic FD	5 – 40Hz	No/Yes	20%	Ricker, 20Hz peak freq.	0 – 9000m with 25m spacing at $z = 0m$	baseline: 0 – 8900m with 100m spacing at $z = 0m$; monitor: 50 – 8950m with 100m spacing at $z = 0m$	Only use offsets upto $\pm 2500m$

Table 5.5: OBN vs streamer: a list of acquisition and inversion parameters.

Modeling method	Band-width	Surface/Internal multiples	Random noise	Wavelet	Source arrangement	Receiver arrangement	Other
Acoustic FD	5 – 40Hz	No/Yes	20%	Ricker, 20Hz peak freq.	0 – 9000m with 50m spacing at $z = 0m$	baseline: 0 – 9000m with 200m spacing at $z = 120m$; monitor: 0 – 9000m with 50m spacing at $z = 0m$	Only use offsets upto $\pm 2500m$

the streamer survey to the ocean-bottom level as well (virtual receivers are on the ocean-bottom level now). Now, both (virtual) receivers and (virtual) sources are on the ocean-bottom level. Next, we extract a subset out of the dataset acquired from the streamer survey to make it have the same geometry as the OBN survey, in which receiver spacing is 200m. Note that it is not necessary for this subset to share exactly the same geometry as the sparse survey, since HR-S-JMI is able to handle the time-lapse datasets from moderately changed monitoring geometries, like the interleaved surveys discussed earlier. Meanwhile, in order to get use of the extra illumination provided by the denser streamer survey, we also input the full dataset acquired from streamer survey as a reference dataset during simultaneous inversion of HR-S-JMI. The final inverted baseline results and time-lapse differences are shown in Figure 5.9. Because of the sufficient illumination provided by the streamer survey, the inverted baseline results in Figures 5.9(a) and 5.9(b) are quite accurate. The velocity difference, being shown in Figure 5.9(c), is reasonably recovered. However, the local change due to injection is overwhelmed by the artifacts caused by non-repeatability of surveys. Regarding the time-lapse image difference in Figure 5.9(d), it is quite clear and focused. Thus, the inverted velocity-difference, though being noisy, is good enough to explain the travel-time difference between two surveys. Therefore, it can be expected that HR-S-JMI can deliver reliable time-lapse changes even when the baseline and monitor datasets are acquired from different types of surveys — OBN vs streamer.

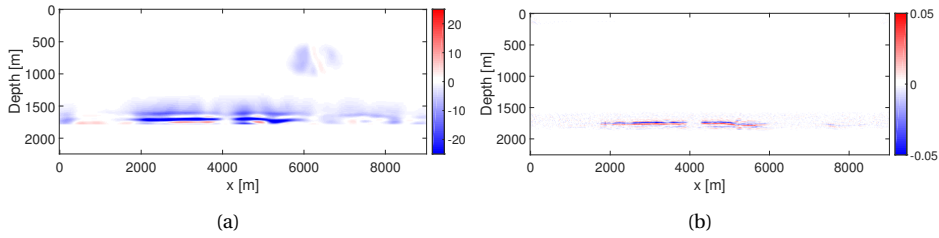


Figure 5.8: Interleaved surveys: (a) and (b) the inverted time-lapse velocity- and reflectivity-difference.

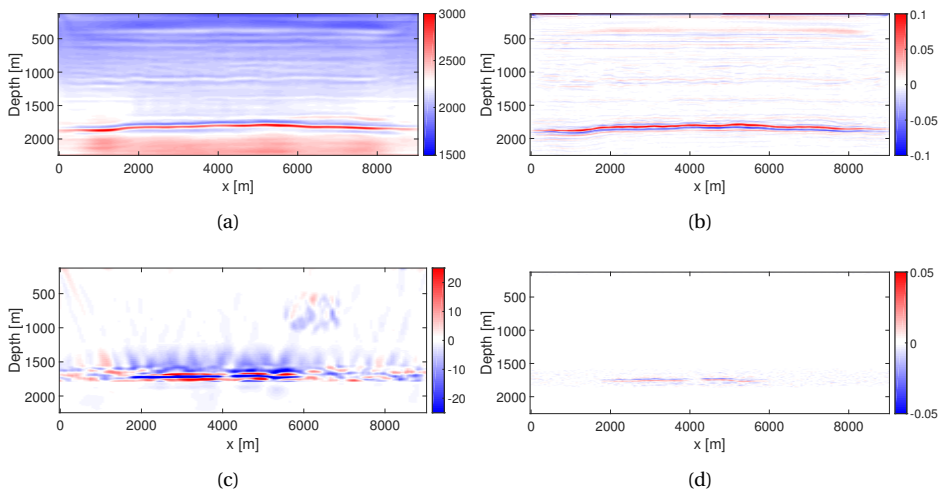


Figure 5.9: OBN vs streamer: (a) and (b) the inverted baseline velocity and reflectivity model; (c) and (d) the inverted time-lapse velocity- and reflectivity-difference.

5.3. NON-REPEATED SOURCES

In this section, we focus on the performance of HR-S-JMI in two scenarios when the sources are not fully repeated: source positioning errors and non-repeated source wavelets.

5.3.1. SOURCE POSITIONING ERRORS

In practice, the source/receiver positions are not always correctly measured during acquisition by GPS equipment. Small positioning deviations are expected during a typical time-lapse monitoring surveys [1]. In this experiment, the time-lapse surveys are designed based on OBN, in which the positions of receivers are fixed and well-measured. We assume the baseline survey positioning is well-done, however, the source positioning of the monitor survey is randomly perturbed by $x = -5m$, $5m$ or $0m$. The rest of the acquisition and inversion settings is the same as those in Section 4.1, which was already shown in Ta-

ble 4.1. Compared to the resulting differences without source positioning errors shown in Figures 5.3(a) and 5.3(b), the final inverted time-lapse differences, being shown in Figure 5.10, are almost of the same quality, only some weak artifacts introduced by the assumed unknown positioning errors can be seen. Therefore, HR-S-JMI is able to deliver good results when there exist small source positioning errors during monitoring.

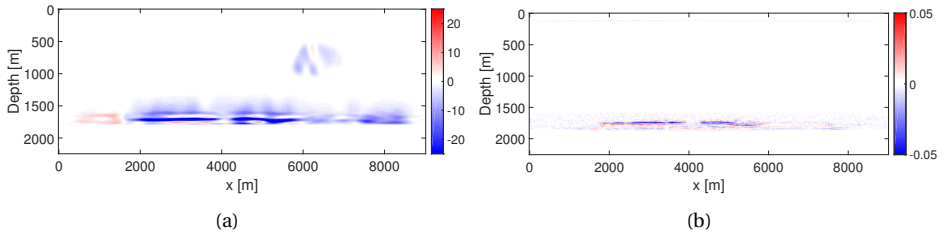


Figure 5.10: Source positioning error: (a) and (b) the inverted time-lapse velocity- and reflectivity-difference.

5

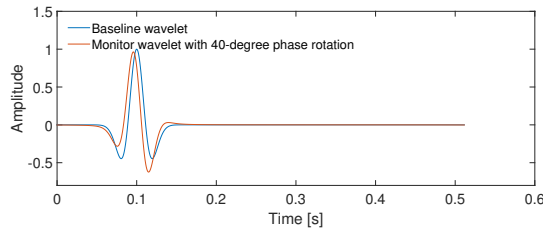


Figure 5.11: Non-repeated wavelets: the source wavelets for the baseline and monitor surveys.

5.3.2. NON-REPEATED SOURCE WAVELETS

During actual time-lapse monitoring, the source wavelet is possibly different from survey to survey. In this experiment, we focus on the impact of source wavelet discrepancy on the performance of HR-S-JMI. For both surveys, the source wavelets are a Ricker wavelet with a dominant frequency of 20 Hz . However, for the baseline, the wavelet has no phase rotation. For the monitor survey, the Ricker wavelet has 40° phase rotation. Both wavelets are shown in Figure 5.11. The related acquisition and inversion settings are listed in Table 5.6. Assuming both wavelets are known and correctly input into a HR-S-JMI process, the inverted time-lapse changes are shown in Figures 5.12(a) and 5.12(b). We can see that the source wavelet discrepancy does not affect the time-lapse results, as long as the correct wavelets are used in HR-S-JMI. However, when we assume baseline wavelet is correct, but a wrong monitor source wavelet (regular Ricker wavelet with no phase rotation) is used, HR-S-JMI fails to detect the time-lapse effects properly and the artifacts caused by incorrect source wavelet are fixed up with the actual time-lapse changes, being shown in

Figures 5.12(c) and 5.12(d). Therefore, the source wavelet discrepancy does not affect the effectiveness of HR-S-JMI, as long as the correct source wavelet is used for each survey.

Table 5.6: Non-repeated wavelets: a list of acquisition and inversion parameters.

Modeling method	Bandwidth	Surface/Internal multiples	Random noise	Wavelet	Source arrangement	Receiver arrangement	Other
Acoustic FD	5 – 40Hz	No/Yes	20%	Ricker, 20Hz peak freq. with baseline: 0° phase rotation; monitor: 40° phase rotation	0–9000m with 25m spacing at $z = 0m$	0–9000m with 100m spacing at $z = 0m$	Only use offsets upto $\pm 2500m$

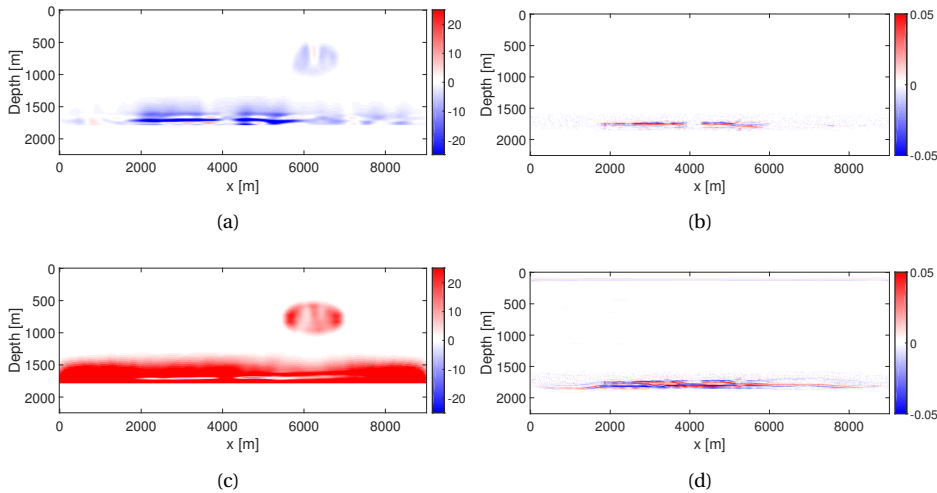


Figure 5.12: Non-repeated wavelets: (a) and (b) the inverted time-lapse velocity- and reflectivity-difference, assuming both wavelets are known and correctly input into a HR-S-JMI process; (c) and (d) the inverted time-lapse velocity- and reflectivity-difference, assuming the baseline wavelet is correct, although a wrong monitor source wavelet is used.

5.4. ROBUSTNESS TO THE L2-NORM CONSTRAINTS BASED ON SPATIAL WEIGHTING OPERATORS

In this section, we investigate the impact of different spatial weighting operators in the L2-norm constraints of HR-S-JMI (the third term in Equation 3.2) on the final time-lapse results. The operators used in Section 4.1 were already shown in Figures 4.5(c) and 4.5(d).

We then design a bank of spatial weighting operators with higher level of relaxation for velocity-/reflectivity-difference, which are shown in Figure 5.13. It can be seen that the level of relaxation increases from Figures 5.13(a),5.13(b) to Figures 5.13(g),5.13(h). In particular, for the spatial weighting operators in Figures 5.13(g),5.13(h), both operators are unity, which means there is no prior information provided in this case. 20% random noise is included in both datasets. The final time-lapse differences corresponding to these spatial weighting operators are shown in Figure 5.14. We can see that the L2-norm constraints based on the spatial weighting operators do help the imaging/inversion and result in less noisy time-lapse differences by importing prior information via the L2-norm constraints. Because they allow the baseline and monitor parameters to communicate with each other by imposing that the parameters should be similar outside the target area influenced by production or injection. When the spatial weighting operators are relaxed, HR-S-JMI remains effective. In particular, even when there is no prior information available, which is shown in Figures 5.14(g) and 5.14(h), HR-S-JMI still provides much better results compared to the results based on the sequential JMI (in Figures 4.4(c)-4.4(f)). Therefore, the effectiveness of HR-S-JMI does not depend on the spatial weighting operators used in the L2-norm constraints, however, a relaxed version of the L2-norm constraints based on prior information is recommended in order to achieve less noisy time-lapse changes, especially for the velocity change estimation.

5.5. SENSITIVITY TO WEAK TIME-LAPSE EFFECTS

In some real-life time-lapse situations, time-lapse effects could be much weaker than the ones in the Grane model being shown in Figure 4.1. In this section, we will demonstrate to what extent HR-S-JMI is able to detect weak time-lapse differences. In order to do so, based on the Grane model in Figure 4.1, we define four weaker velocity and density differences, in which the values are 80%, 60%, 40%, and 20% of the original differences, respectively. The associated reflectivity differences are calculated from the new velocity and density differences. One near-offset trace of the set of new velocity differences is shown in Figure 5.15. For the last scenario (20% of the original differences), the highest absolute value is only 35.18m/s . 20% random noise is included in both datasets. By using HR-S-JMI, the final time-lapse differences are shown in Figure 5.16. Note that the clipping of the figures is also adjusted proportionally. When the model difference is 80%, 60%, and 40% of the original one, both velocity and reflectivity differences are reliably detected, shown in Figures 5.16(a)-5.16(e). In the case when the difference is only 20% of the original one, the velocity difference in Figure 5.16(g) is quite noisy, though it is good enough to explain the small travel-time difference because the inverted image difference is very well recovered, being shown in Figure 5.16(h). Therefore, HR-S-JMI has good sensitivity to weak time-lapse effects. It functions reliably even in the case when the maximum value of velocity change is around $\pm 35\text{m/s}$.

5.6. CONCLUSION

In this chapter, several numerical experiments based on the Grane field, offshore Norway are carried on to investigate the feasibility of using HR-S-JMI in some scenarios, where the quality of the time-lapse surveys or datasets is not perfect. The experiments take the

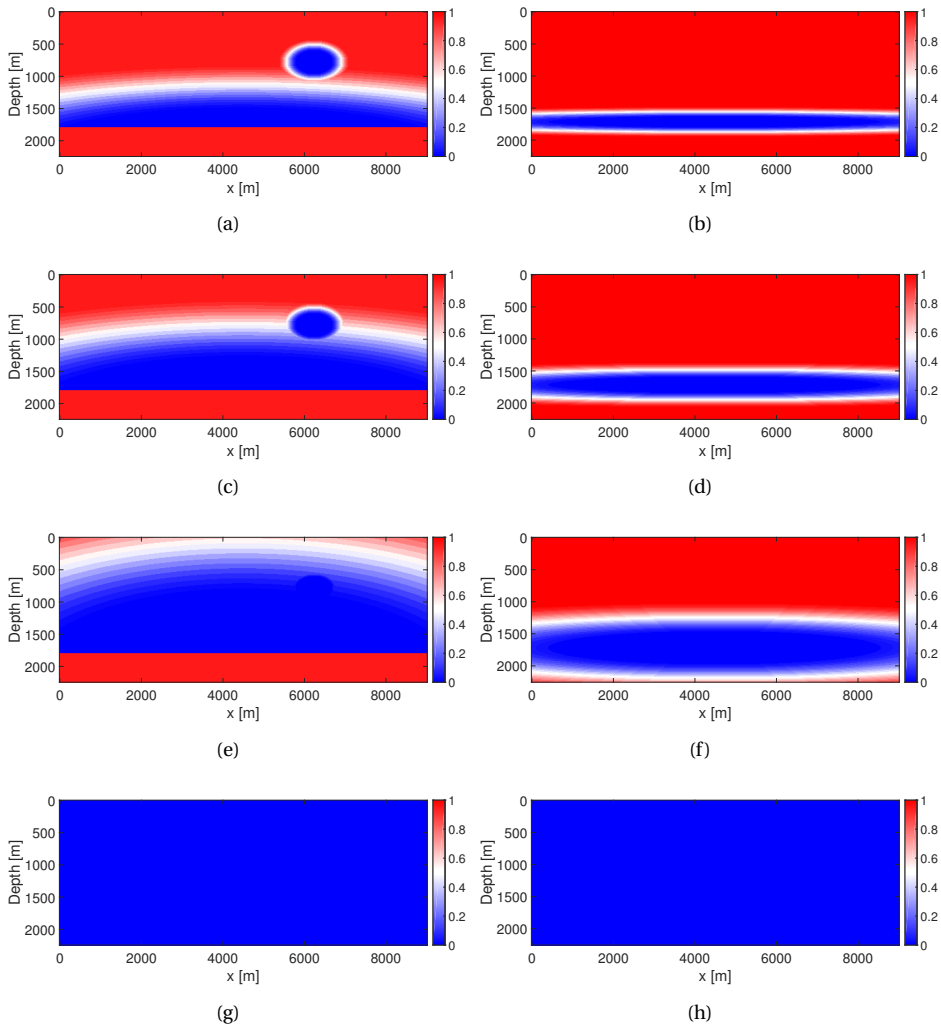


Figure 5.13: Robustness to spatial weighting operators: a bank of spatial weighting operators with different level of relaxation, which are designed based on prior information. The level of relaxation increases from (a),(b) to (g),(h); in particular, in (g) and (h), both spatial weighting operators are unity, which means there is no prior information provided.

following aspects into account:

- Random noise;
- Coherent noise caused by the acoustic assumption;
- Sparse surveys;

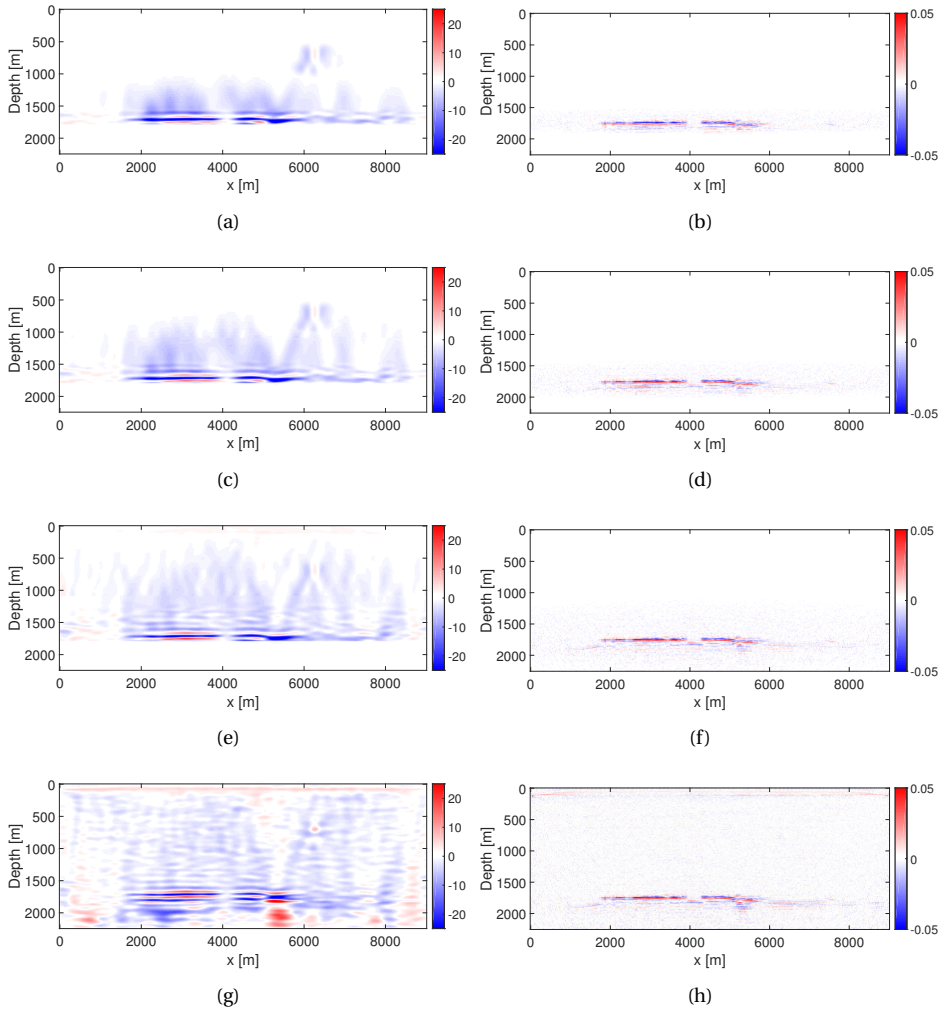


Figure 5.14: Robustness to the choice of the spatial weighting operators: the inverted time-lapse velocity- and reflectivity-differences corresponding to the spatial weighting operators shown in Figure 5.13.

- Non-repeated surveys;
- Different types of surveys: OBN vs streamer;
- Source positioning errors;
- Non-repeated source wavelets;
- Robustness to the L2-norm constraints;

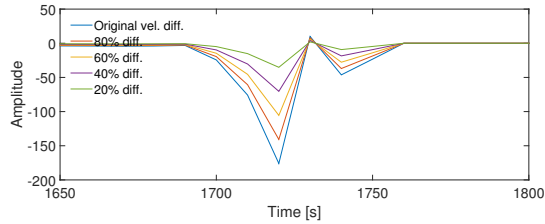


Figure 5.15: Sensitivity to weak time-lapse effects: one near-offset trace of the velocity difference, in which the values are 80%, 60%, 40%, and 20% of the original one.

- Sensitivity to weak time-lapse effects.

HR-S-JMI is very robust to random noise and coherent noise caused by acoustic assumption. Regarding the time-lapse survey design, HR-S-JMI is able to deliver reliable time-lapse differences when the surveys are sparse or mildly changed during monitoring. Moreover, it can be expected that HR-S-JMI inverts reasonably accurate time-lapse changes even when the baseline and monitor datasets are acquired from different types of surveys — OBN vs streamer. When there exist small errors during source position measurements, the inverted results by using HR-S-JMI are almost as good as the error-free case. The source wavelet discrepancy between surveys does not affect the effectiveness of the method, as long as the correct source wavelet is used for each survey. Furthermore, the method remains effective when the spatial weighting operators in the L2-norm constraints are largely relaxed, however, a relaxed version of the L2-norm constraints based on prior information is recommended in order to achieve less noisy time-lapse changes. In the end, HR-S-JMI has the ability to detect weak time-lapse changes. It provides reliable results even in the case when the maximum value of time-lapse velocity-difference is around $\pm 35\text{m/s}$.

5.7. ACKNOWLEDGMENT

We thank Equinor, CGG, and the Grane license partners Petoro AS, ExxonMobil E&P Norway AS and ConocoPhillips Skandinavia AS, for the release of the Grane synthetic velocity model. The views and opinions expressed in this work are those of the authors and not necessarily shared by Equinor ASA, CGG, and the Grane license partners.

REFERENCES

- [1] C. J. Beasley, R. E. Chambers, R. L. Workman, K. L. Craft, and L. J. Meister, *Repeatability of 3-D ocean-bottom cable seismic surveys*, *The Leading Edge* **16** (1997), pp. 1281–1286.

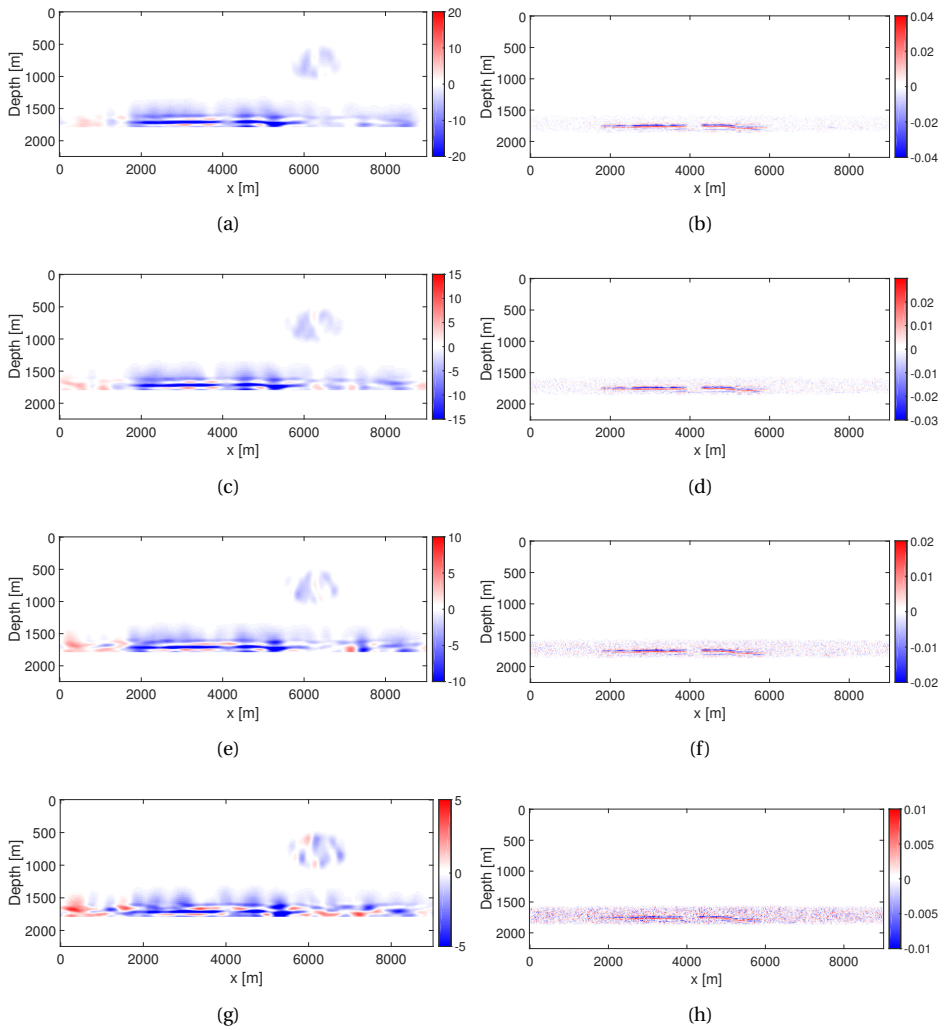


Figure 5.16: Sensitivity to weak time-lapse effects: the inverted time-lapse velocity- and reflectivity-differences, in which the values are 80% (a) and (b), 60% (c) and (d), 40% (e) and (f), and 20% (g) and (h) of the original one. Note that the clipping of the figures is also adjusted proportionally.

6

S-JMI WITH CALENDER-TIME CONSTRAINTS AS A PROCESSING TOOL FOR SEMI-CONTINUOUS SURVEYS

Nowadays, in order to get a better understanding of the dynamic time-lapse changes, frequent seismic monitoring is necessary, although it will generate a considerable cost increase. Therefore, low-cost frequent monitoring, e.g. sparse and/or non-repeated surveys, is desired. However, most imaging/inversion methodologies are based on repeated and dense monitoring acquisition geometries. As was discussed in the previous Chapters, Simultaneous Joint Migration Inversion (S-JMI), as an effective time-lapse tool for reservoir monitoring, combines a simultaneous time-lapse processing strategy with the Joint Migration Inversion (JMI) method. It is largely independent of the utilized acquisition geometry, e.g. sparse and non-repeated monitoring surveys. This feature makes it suitable for inexpensive frequent monitoring surveys. Therefore, we propose to use S-JMI for the datasets acquired from inexpensive semi-continuous time-lapse monitoring surveys, which are based on a so-called instantaneous 4D (i4D) survey technology. In the i4D technology, inexpensive localized and sparse surveys, termed i4D surveys, are employed between the conventional full-field surveys. This technology can be treated as a special case of changing geometries during monitoring. In this case, the simultaneous strategy of S-JMI allows the full-field survey information to compensate the poor illumination of the sparse i4D surveys during process. Furthermore, we propose to apply extra constraints on the reflectivity- and velocity-differences between the baseline and monitors along the calendar-time axis, termed calendar-time constraints. These constraints take advantage of the feature that time-lapse effects develop almost continuously along the calendar-time axis during semi-continuous monitoring. With a complex synthetic example based on the Marmousi model, we demonstrate that S-JMI is a promising tool to process datasets from the semi-continuous monitoring surveys based on

the i4D survey technology. We also show that the extra calender-time constraints significantly improve the quality of time-lapse effects. Finally, we compare the time-lapse results assuming all the monitor datasets are available to those results where only the datasets up to the current one are used.

6.1. INTRODUCTION

In order to get a better understanding of the dynamic time-lapse changes, frequent seismic monitoring is necessary [1]. Most time-lapse processing methodologies, e.g. the conventional method based on a time-shift map and sequential JMI described in Chapter 2, are based on repeated and dense monitoring acquisition geometries. However, such sufficient monitoring surveys are normally unaffordable. Therefore, two important questions are: "Do we need to reacquire seismic data in exactly the same way in order to address time-lapse differences?", and "Do we require the time-lapse acquisitions with dense receiver/source sampling?"

For the first question, we propose to reverse the argument: by changing the acquisition geometry during the monitoring, we obtain more information on the subsurface. [2, 3] and [4] demonstrated that if time-lapse acquisitions are done with designed non-repeatable acquisition, a better time-lapse response will be provided. Some researchers have already done investigations on the non-repeatability issue. [5–7] addressed it by using a joint time-lapse processing strategy. [8] proved that, because JMI is an inversion process, the actual locations of the seismic measurements — providing a sufficient illumination of the subsurface with primaries and multiples is achieved — is not so important, such that the method becomes largely independent of geometry. They show that small time-lapse effects are successfully recovered from a strongly scattering overburden when there exists a non-repeatability issue, based on a sequential time-lapse strategy. Furthermore, in Chapter 3, simultaneous JMI (S-JMI) was proposed, which combines the joint time-lapse strategy with the benefit of JMI, to relax the rigid requirements of monitoring surveys. The experiments in Chapter 5 have shown that S-JMI does not require dense geometry sampling or exactly repeated geometries during monitoring. This leads to the answer of the second question: S-JMI is able to handle time-lapse datasets generated from sparse surveys. Therefore, the capability of handling sparse and non-repeated surveys makes S-JMI a promising processing tool for inexpensive frequent seismic monitoring scenarios.

Regarding the cost-effective frequent seismic monitoring acquisition design, [9], [10], and [11] proposed to shoot inexpensive localized and/or sparse surveys, termed i4D surveys, between conventional full-field surveys. Most time-lapse processing methodologies are based on dense monitoring surveys and only compare the differences between the same type of surveys (between full-field surveys, or between sparse i4D surveys). Therefore, in this chapter, we propose to use S-JMI as the processing tool for the datasets acquired from inexpensive semi-continuous time-lapse monitoring surveys based on the i4D survey technology. S-JMI allows the full-field survey information to compensate the poor illumination of the sparse i4D surveys during process and also compares the differences between different types of surveys. Moreover, during the processing workflow, we

propose to add extra calendar-time constraints on the image- and velocity-differences between the monitors and baseline surveys along the calendar-time axis, termed calendar-time constraints, to further improve the time-lapse results.

The chapter is organized as follows: we begin with the review of the previously proposed i4D seismic monitoring technology [9–11]. After that, we introduce the theory of S-JMI with the extra calendar-time constraints, which take advantage of the feature that time-lapse effects develop almost continuously along the calendar-time axis during semi-continuous monitoring. Finally, with one complex synthetic example based on the Marmousi model, we demonstrate that S-JMI is an effective tool to process datasets acquired from the semi-continuous monitoring surveys, which are designed according to the i4D technology. We also show that the proposed calendar-time constraints significantly improve the quality of the time-lapse results. In addition, we compare the time-lapse results assuming all the monitoring datasets are available to those results where only the datasets up to the current one are used.

6.2. REVIEW OF A SEMI-CONTINUOUS FREQUENT MONITORING CONCEPT — I4D TECHNOLOGY

Time-lapse seismic typically requires multiple surveys over time to optimize development decisions. Some time-lapse changes, such as compaction and aquifer drive, happen at relatively slow time scales. Therefore, proper monitoring surveys are usually employed every 3-5 years. Time-lapse changes, which are usually associated with water injection, are taking place relatively rapidly [9, 10, 12, 13]. In this case, typical monitoring surveys with a repeat frequency of 3-5 years may miss important effects. In order to get a better understanding of the latter scenario, frequent seismic monitoring is necessary, although it will generate a proportionate cost increase. [9], [10], and [11] proposed a new frequent monitoring method, the so-called instantaneous 4D (i4D) technology. They addressed this dilemma by shooting inexpensive localized and/or sparse surveys, termed i4D surveys, every 6 months to 1 year, between conventional full-field surveys employed every 3-5 years. The cost level of i4D surveys is low enough to make it affordable to be carried on frequently. The schematic representation of this i4D concept is shown in Figure 6.1. In this work, we also refer to this kind of frequent monitoring concept as semi-continuous monitoring. However, most imaging/inversion methods are based on repeated and dense monitoring acquisition geometries and only compare the differences between the same type of surveys. Therefore, a more powerful processing tool is desirable to fit this new semi-continuous monitoring technology.

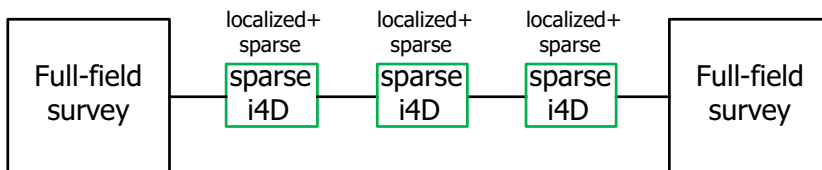


Figure 6.1: Schematic representation of the i4D acquisition technology.

6.3. THEORY OF S-JMI WITH CALENDER-TIME CONSTRAINTS FOR SEMI-CONTINUOUS DATASETS

As was discussed in the previous chapters, Simultaneous Joint Migration Inversion (S-JMI) is an effective time-lapse tool for reservoir monitoring, which combines a joint time-lapse data processing strategy with the Joint Migration Inversion (JMI) method. S-JMI is largely independent of the utilized acquisition geometry, e.g. sparse and/or changed surveys. This feature makes it suitable for the inexpensive semi-continuous i4D technology, which can be treated as a special case of changing geometries during monitoring. The simultaneous strategy of S-JMI can help compensate the poor illumination of the sparse surveys with full-field survey information during process. The schematic representation of S-JMI was already shown in Figure 1.7.

The S-JMI algorithm is parameterized with the baseline reflectivity/velocity and the time-lapse reflectivity-/velocity-difference. Its objective function was already shown in equation 3.2. For the i4D monitoring scenario, we assume that the baseline survey ($[T_0]$) is a full-field survey providing sufficient illumination. Therefore, the L2-norm constraints can help to compensate the poor illumination of the i4D sparse surveys with the full-field baseline survey information during inversion.

When the monitoring surveys are employed almost continuously over calendar-time, the time-lapse parameter changes between baseline and monitors ($\Delta\mathbf{r}[T_n]$ and $\Delta\mathbf{v}[T_n]$) also evolve semi-continuously over calendar-time T . In this case, by taking advantage of this feature, two extra constraints are proposed and added to the objective function 3.2:

$$\begin{aligned}
 J_{S\text{-JMI-i4D}} = J_{S\text{-JMI}} & \\
 & + \sum_{n=0}^{N_x-1} \lambda_4 \|\mathbf{C}_{(z,T)}^{-1} \Delta\mathbf{r}(x_n)\|_1 \\
 & + \sum_{n=0}^{N_x-1} \lambda_5 \|\mathbf{S}_{(z,T)}^{-1} \Delta\mathbf{v}(x_n)\|_2^2.
 \end{aligned} \tag{6.1}$$

The first constraint is an L1 denoising constraint on the reflectivity-differences between the baseline and monitors along the calendar-time axis. N_x is the number of samples along the x-axis of the model and x_n is the n^{th} point of x . $\mathbf{C}_{(z,T)}^{-1}$ is a sparsity-promoting transform from the (z, T) domain. λ_4 is a weighting parameter. We solve this L1 denoising problem by a soft-thresholding process in the curvelet domain [14]. The second constraint is a smoothing regularization on the velocity-differences along the calendar-time axis and $\mathbf{S}_{(z,T)}^{-1}$ is a smoothing operator. λ_5 denotes the weight of this penalty term. In the current implementation, both constraints are evaluated independently for each spatial location x .

The schematic representation of the proposed S-JMI with calendar-time constraints for semi-continuous frequent monitoring is shown in Figure 6.2.

6.4. EXAMPLE

In this section, with a Marmousi-based example we will demonstrate that S-JMI is a suitable tool to process the datasets acquired from the semi-continuous frequent monitoring

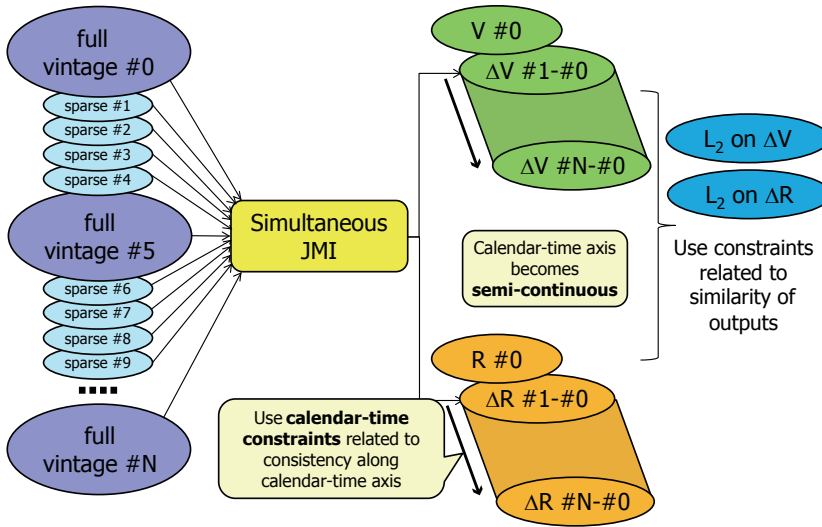


Figure 6.2: Schematic representation of S-JMI with the extra calendar-time constraints for semi-continuous monitoring based on the i4D technology.

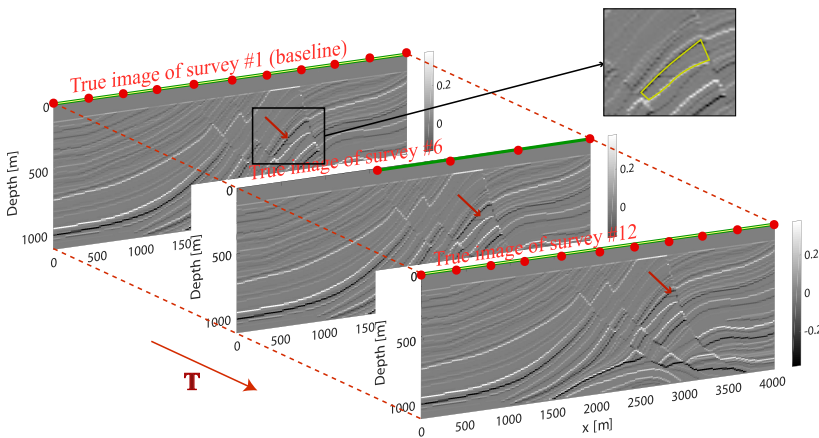


Figure 6.3: The true reflectivity models for the semi-continuous monitoring based on i4D, considering 12 datasets in total. The area enclosed with the yellow curve is the gas-sand trap. The red arrows point to the time-lapse changes, where the water-gas replacement gradually happens over time. The receivers and sources are shown as red dots and green line, respectively.

surveys based on the i4D technology proposed by [9], and also show the effectiveness of the extra calendar-time constraints.

We consider a Marmousi-based model with a gas-sand trap highlighted in Figure 6.3.

For the sake of this initial analysis, we assume that water-gas replacement gradually happens over time during the monitoring, pointed out with red arrows in Figure 6.3. The time-lapse changes due to pressure perturbations in the reservoir and overburden/underburden area are also considered. There are 12 surveys in total. Based on an OBN-type acquisition, the receiver and source sampling is 400m and 20m, respectively, for the full-field surveys. For the sparse i4D surveys, the receiver sampling is 800m and the source sampling remains the same. Moreover, the receivers and sources are only placed locally to illuminate the target area, shown as red dots and green line, respectively, in Figure 6.3. We set the 1st and 12th surveys to be full-field surveys and the surveys between them to be sparse i4D surveys. In this acquisition design, the setting of the i4D surveys is part of the setting of the full-field survey. To minimize the side effects of changing geometries during monitoring, we extract the subsets out of the datasets acquired from full-field surveys to make it have the same geometry as the i4D surveys. We call these two subsets together with the datasets from i4D surveys as the main datasets. Please note that it is not necessary to design the setting of the sparse i4D surveys exactly as part of the full-field survey, since S-JMI is able to handle the time-lapse datasets from moderately changed monitoring geometries, like interleaved geometries discussed in Chapter 5. Meanwhile, in order to get use of the extra illumination provided by the full-field surveys, we also input the full-field datasets acquired from full-field surveys as two reference datasets during simultaneous inversion. The initial reflectivities are zero and the initial velocity model is a very simple vertical gradient (shown in Figures 6.4(a) and 6.4(b)). Both primaries and multiples are considered, and 20% random noise is added to all the datasets. After applying regular JMI to the baseline dataset (1st full-field dataset), we get the inverted baseline reflectivity and velocity models being shown in Figures 6.4(c) and 6.4(d). This inverted baseline velocity model then serves as the initial velocity for the following time-lapse process.

Table 6.1: i4D example: a list of acquisition and inversion parameters.

Modeling method	Band-width	Surface/Internal multiples	Random noise	Wavelet	Source arrangement	Receiver arrangement	other
FWMOD	5 – 40Hz	Yes/Yes	20%	Ricker, 20Hz peak freq.	full surveys: 0 – 4000m with 20m spacing i4D surveys: 1600 – 4000m with 20m spacing	full surveys: 0 – 4000m with 400m spacing i4D surveys: 1600 – 4000m with 800m spacing	

We compare four scenarios: ① sequential JMI, ② S-JMI, ③ S-JMI with the calendar-time constraints, and in the end, ④ S-JMI applied to the currently acquired datasets, which means the time-lapse differences are calculated using only the datasets that have already been acquired by the current calendar-time. For example, the 1st, 2nd, 3rd datasets are the input data when calculating the difference between the 3rd and the 2nd survey. In addition, the calendar-time constraints are switched on after the 7th survey in scenario 4.

The inverted final images on the target area from the 3rd, 5th, 7th, 9th i4D surveys for scenario 1 and 2 are shown in Figure 6.5 and 6.6, respectively. Compared to the inverted results using sequential JMI (scenario 1), the images in Figure 6.6 inverted by using S-

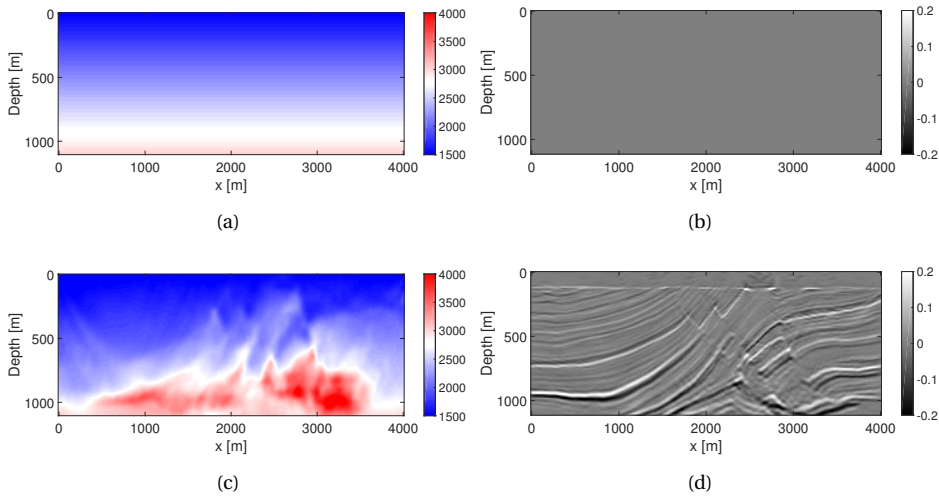


Figure 6.4: *i4D* example: (a) and (b) initial reflectivity and velocity model for JMI; (c) and (d) the inverted baseline reflectivity and velocity model.

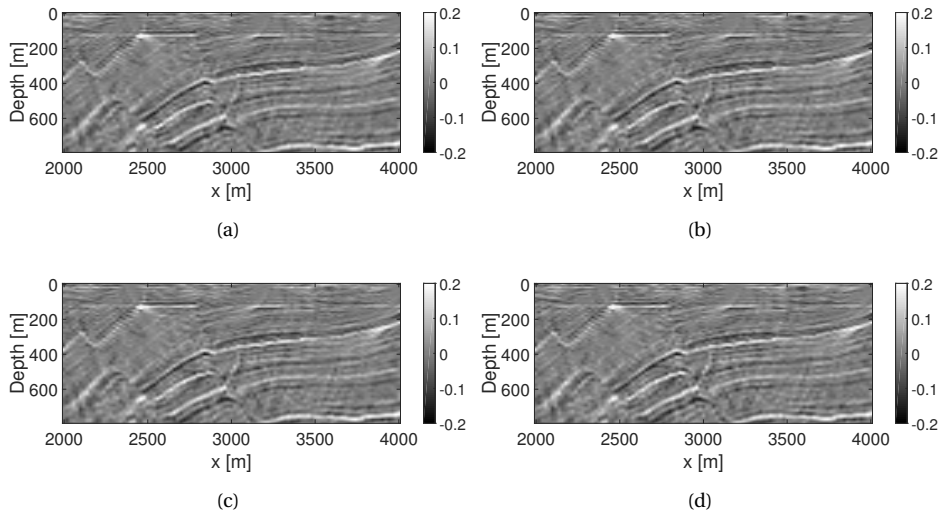


Figure 6.5: *i4D* example: the inverted reflectivity models using sequential JMI for the: 3rd (a), 5th (b), 7th (c), 9th (d) sparse *i4D* survey.

JMI (scenario 2) reveal more complete subsurface information by making use of all the datasets and multiples to compensate the poor illumination. We can see that several imprints and artifacts using sequential JMI (scenario 1) in Figure 6.5 are now suppressed in the S-JMI (scenario 2) results in Figures 6.6.

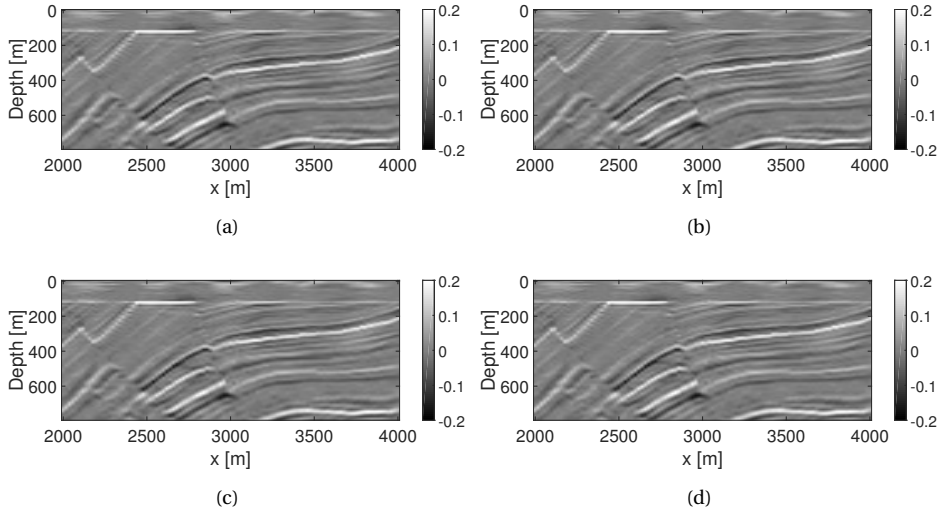


Figure 6.6: *i4D* example: the inverted reflectivity models using S-JMI for the: 3rd (a), 5th (b), 7th (c), 9th (d) sparse *i4D* survey.

6

In terms of the time-lapse differences, we demonstrate 6 sets of the reflectivity differences: $2^{nd} - 1^{st}$, $4^{th} - 3^{rd}$, $6^{th} - 5^{th}$, $8^{th} - 7^{th}$, $10^{th} - 9^{th}$, and $12^{th} - 11^{th}$. In Figure 6.7 (scenario 1), the final reflectivity differences inverted using sequential JMI can provide some time-lapse information, but they are quite noisy due to the poor illumination of the sparse *i4D* surveys and the additive random noise in the data. The inverted time-lapse effects using S-JMI shown in Figure 6.8 (scenario 2) are much more clear, because S-JMI allows us to make use of all the datasets to compensate with each other. However, they are still somewhat noisy. Furthermore, by taking advantage of the feature that the time-lapse changes evolve almost continuously over calendar-time in this case of frequent monitoring, S-JMI with the extra calendar-time constraints along the monitoring time, as visible in Figure 6.9 (scenario 3), achieves much better results. Now the time-lapse effects are almost completely isolated from artifacts related to the sparse geometries.

In the end, we test a more realistic scenario, scenario 4, where S-JMI is applied only to the currently acquired datasets. The corresponding time-lapse differences are shown in Figure 6.10. We can see that the inverted differences in scenario 4, even at the early stage of monitoring, show much better quality compared to the sequential JMI in Figure 6.7 (scenario 1), by making use of the 1st full-field survey as the reference full-field dataset to compensate the poor illumination. This also indicates that S-JMI can do a pretty good job even with very few datasets being inverted simultaneously, as long as at least one high-quality dataset from full-field survey is included as the reference full-field dataset during inversion. As can be expected, the inverted differences in scenario 4 are noisier compared to Figure 6.9 (scenario 3) for the earlier surveys, because of the effectiveness of the calendar-time constraints in scenario 3. However, surprisingly enough, these differences seem less noisy than the ones in Figure 6.8 (scenario 2). In this case, assuming one high-quality

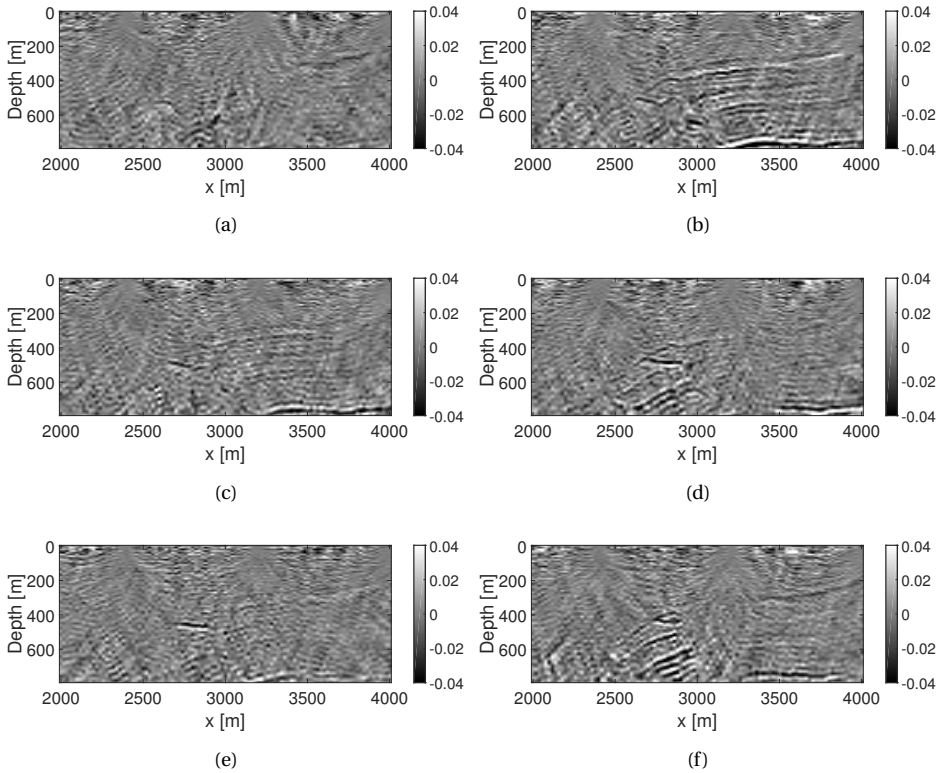


Figure 6.7: *i4D* example: the inverted reflectivity differences using sequential JMI: 2nd survey – 1st survey (a), 4th survey – 3rd survey (b), 6th survey – 5th survey (c), 8th survey – 7th survey (d), 10th survey – 9th survey (e), 12th survey – 11th survey (f).

full-field dataset is already included in S-JMI, adding more worse-quality datasets (from sparse *i4D* surveys) to invert simultaneously apparently introduces more noise (scenario 4 vs scenario 2).

6.5. DISCUSSION

6.5.1. COMPUTATIONAL ASPECTS

In the case of (semi-)continuous monitoring, assuming that the amount of computation efforts of JMI applied to one full-field vintage is K and to one sparse *i4D* vintage is M ($M \ll K$) and there are N_T^{full} full-field vintages and N_T^{i4D} sparse *i4D* vintages, the computation time of S-JMI is around $N_T^{i4D} * M + N_T^{full} * K + N_T^{full} * M$ if all the datasets are inverted simultaneously. Note that, in order to minimize the side effects of using different types of surveys during monitoring, we also include the subsets of the full-field datasets as the extra input to make it have similar illumination as the sparse *i4D* surveys (corresponds

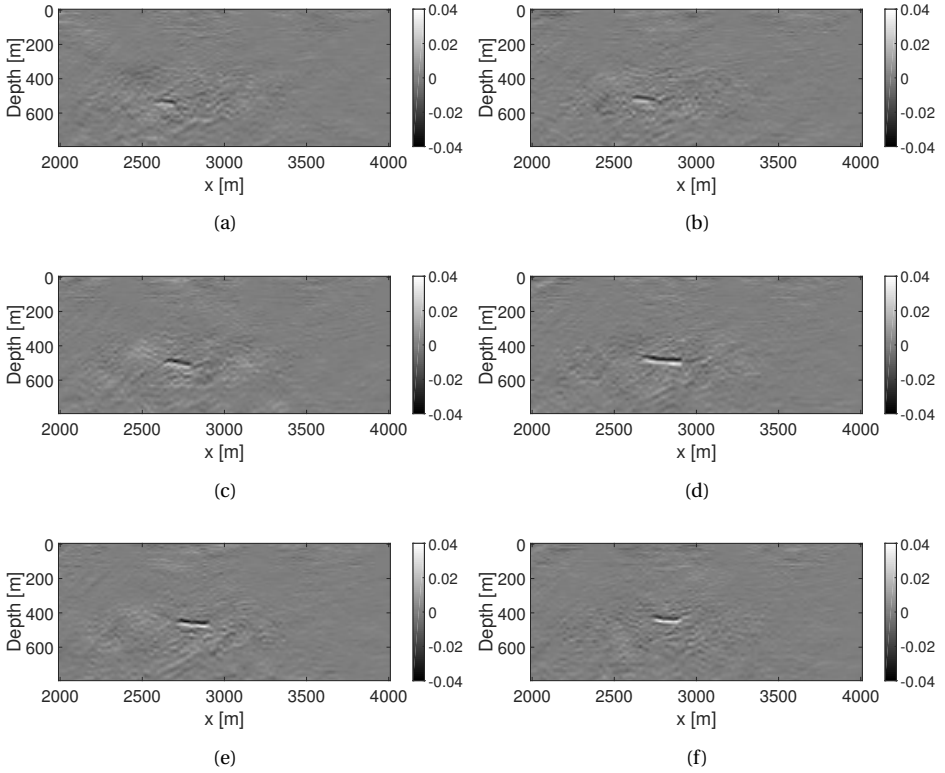


Figure 6.8: *i4D* example: the inverted reflectivity differences using S-JMI, assuming all the datasets are available: 2nd survey – 1st survey (a), 4th survey – 3rd survey (b), 6th survey – 5th survey (c), 8th survey – 7th survey (d), 10th survey – 9th survey (e), 12th survey – 11th survey (f).

to $N_T^{full} * M$ in computation time).

However, as was mentioned in the previous section, there is no need to invert all the datasets together. Instead, one high-quality dataset from a full-field survey can be chosen as the reference dataset for S-JMI to invert simultaneously together with the target seismic vintages, yielding the inverted time-lapse results as good as the scenario where all the datasets are inverted simultaneously. Therefore, to calculate the time-lapse difference of any two surveys, the computation time of S-JMI is around $2 * M + K$.

6.5.2. THE FEASIBILITY OF THE CALENDER-TIME CONSTRAINTS

One requirement of applying the proposed calendar-time constraints during the time-lapse process is the smoothness and consistency of the time-lapse changes over calendar-time during semi-continuous monitoring. However, one important goal of frequent monitoring is to better understand unexpected events especially around the injectors. In this

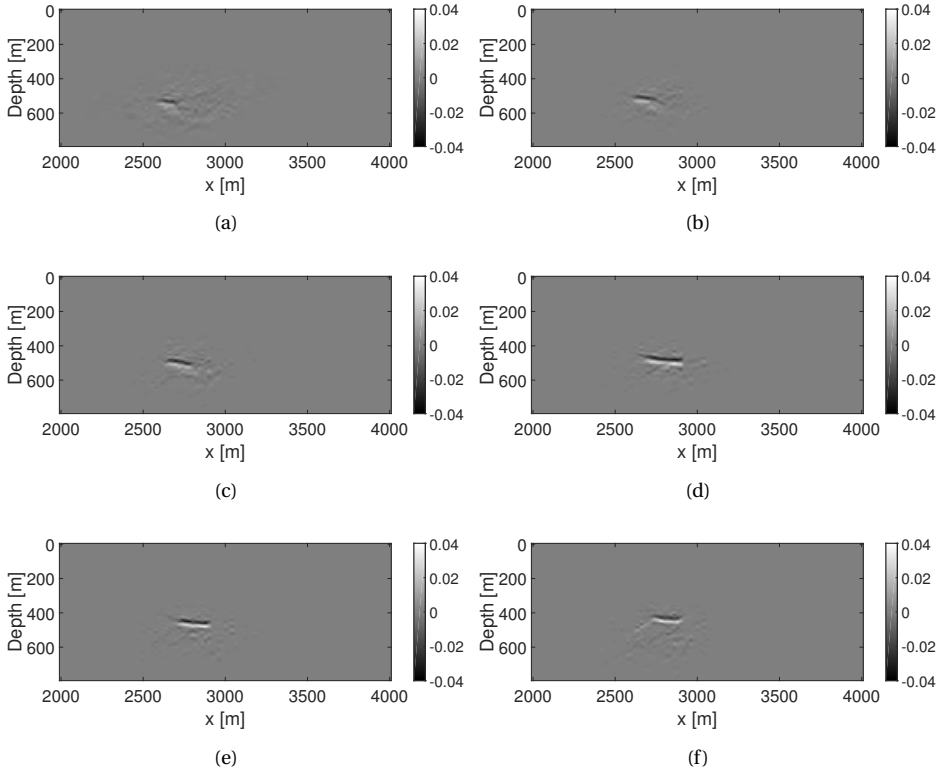


Figure 6.9: *i4D* example: the inverted reflectivity differences using S-JMI with the extra L1 calender-time constraints, assuming all the datasets are available: 2nd survey – 1st survey (a), 4th survey – 3rd survey (b), 6th survey – 5th survey (c), 8th survey – 7th survey (d), 10th survey – 9th survey (e), 12th survey – 11th survey (f).

case, one solution is to use spatial weighting operators for the calender-time constraints, which put less strong constraints on the area close to the injection point and stronger constraints outside this target area, instead of the constant weighting parameters λ_2 and λ_3 used in the objective function 6.1. Another solution is to use a better constraint which is less sensitive to the impulsive changes, like total variation regularization discussed in Appendix B.

6.6. CONCLUSION

In order to get a better understanding of the dynamic time-lapse changes, low-cost frequent seismic monitoring is desired. When using a simultaneous inversion approach, we can allow the monitoring surveys to be much sparser sampled than the baseline survey and still get good time-lapse imaging results. Therefore, we propose simultaneous Joint Migration Inversion (S-JMI) as a suitable tool for accurate time-lapse imaging for

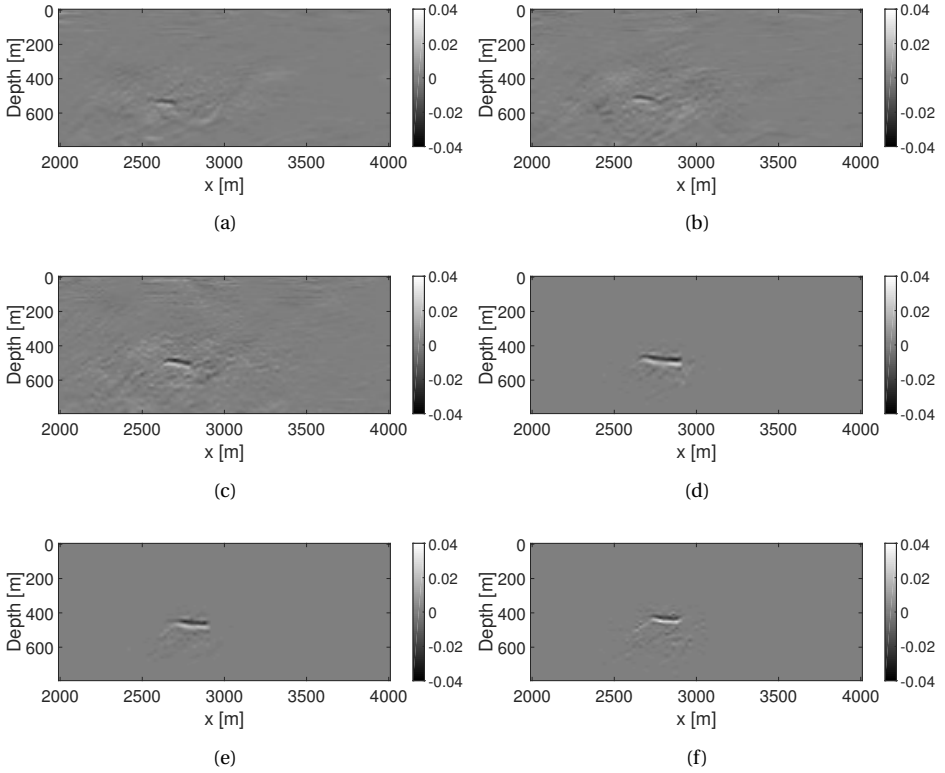


Figure 6.10: *i4D* example: the inverted reflectivity differences using S-JMI applied to the datasets up to the current one and the calendar-time constraints are switched on after 7th survey: 2nd survey – 1st survey (a), 4th survey – 3rd survey (b), 6th survey – 5th survey (c), 8th survey – 7th survey (d), 10th survey – 9th survey (e), 12th survey – 11th survey (f).

such sparse-data monitoring scenario. To further enhance the time-lapse quality, assuming semi-continuous monitoring, we augment this with calendar-time constraints on the reflectivity- and velocity-differences between the baseline and monitors along the calendar-time axis. These constraints take advantage of the feature that time-lapse effects develop almost continuously along the calendar-time axis, when the monitoring surveys are employed almost continuously over calendar-time. This is demonstrated on a synthetic dataset based on the Marmousi model. Finally, we show that S-JMI can perform well even when only the datasets up to the current one are used, as long as at least one high-quality dataset from full-field survey is included as the reference full-field dataset during inversion.

REFERENCES

- [1] J.-P. Van Gestel, J. H. Kommedal, O. I. Barkved, I. Mundal, R. Bakke, and K. D. Best, *Continuous seismic surveillance of valhall field*, [The Leading Edge](#) **27** (2008), pp. 1616–1621.
- [2] F. Oghenekohwo, H. Wason, E. Esser, and F. J. Herrmann, *Low-cost time-lapse seismic with distributed compressive sensing—part 1: Exploiting common information among the vintages*, [Geophysics](#) **82** (2017), pp. P1–P13.
- [3] H. Wason, F. Oghenekohwo, and F. J. Herrmann, *Low-cost time-lapse seismic with distributed compressive sensing—part 2: Impact on repeatability*, [Geophysics](#) **82** (2017), pp. P15–P30.
- [4] S. Qu and D. J. Verschuur, *Simultaneous time-lapse imaging via joint migration and inversion*, in [78th EAGE Conference and Exhibition 2016](#) (Eur. Ass. of Geosc. and Eng., Expanded abstracts, 2016).
- [5] G. Ayeni and B. Biondi, *Target-oriented joint least-squares migration/inversion of time-lapse seismic data sets*, [Geophysics](#) **75** (2010), pp. R61–R73.
- [6] M. Maharramov and B. Biondi, *Joint full-waveform inversion of time-lapse seismic data sets*, in [SEG Technical Program Expanded Abstracts 2014](#) (Society of Exploration Geophysicists, 2014) pp. 954–959.
- [7] M. Maharramov and B. Biondi, *Robust simultaneous time-lapse full-waveform inversion with total-variation regularization of model difference*, in [77th EAGE Conference and Exhibition 2016](#) (Eur. Ass. of Geosc. and Eng., Expanded abstracts, 2015).
- [8] D. Verschuur and X. Staal, *Using primaries and multiples in time-lapse imaging and velocity estimation*, in [SEG Technical Program Expanded Abstracts 2014](#) (Society of Exploration Geophysicists, 2014) pp. 4955–4959.
- [9] P. J. Hatchell, K. wang, J. L. Lopez, J. G. F. Stammeijer, and M. Davidson, *Instantaneous 4D seismic (i4D) for water injection monitoring*, in [EAGE incorporating SPE EUROPEC 2013](#) (Eur. Ass. of Geosc. and Eng., Expanded abstracts, 2013).
- [10] J. Stammeijer, M. Davidson, P. Hatchell, and J. Lopez, *Instantaneous 4D seismic (i4D)—an innovative concept to monitor offshore water injector wells*, in [IPTC 2013: International Petroleum Technology Conference](#) (2013).
- [11] T. Barker, D. Chalenski, G. Wainright, W. Reid, J. Stammeijer, D. Kiyashchenko, and P. Hatchell, *Subsalt time-lapse seismic for reservoir monitoring using i4D in deepwater*, in [77th EAGE Conference and Exhibition 2015](#) (Eur. Ass. of Geosc. and Eng., Expanded abstracts, 2015).
- [12] T. Alsos, B. Osdal, and A. Hoiås, *The many faces of pressure changes in 4D seismic at the svale field and its implication on reservoir management*, in [71st EAGE Conference and Exhibition incorporating SPE EUROPEC 2009](#) (Eur. Ass. of Geosc. and Eng., Expanded abstracts, 2009).

- [13] K. Wang, P. Hatchell, A. Mateeva, D. Kiyashchenko, Y. Duan, and J. Lopez, *Practical frequent reservoir monitoring*, in *Second EAGE Workshop Practical Reservoir Monitoring 2019* (Eur. Ass. of Geosc. and Eng., Expanded abstracts, 2019).
- [14] J.-L. Starck, E. J. Candès, and D. L. Donoho, *The curvelet transform for image denoising*, *IEEE Transactions on image processing* **11** (2002), pp. 670–684.

7

CONCLUSION AND RECOMMENDATIONS

7.1. CONCLUSION

The conventional time-lapse processing workflow is usually sensitive to the non-repeatable uncertainties between different vintages caused by noise, acquisition designs, and independent processing. Therefore, in order to reduce these non-repeatable uncertainties, all the datasets are usually acquired from well-sampled and well-repeated acquisition surveys and the independent processing is always carefully tailored to maximally reduce the non-repeatable uncertainties during processing. Moreover, the conventional method, based on a time-shift map, is not always a good indicator of the actual velocity differences due to its local 1D subsurface assumption. Therefore, a time-lapse processing tool, which is less demanding on acquisition and has a better velocity change indicator, is desirable.

In this thesis, we proposed Simultaneous Joint Migration Inversion (S-JMI) as an effective time-lapse tool for reservoir monitoring. The method combines a simultaneous data processing strategy with the Joint Migration Inversion (JMI) method. JMI is a full wavefield inversion method with a parameterization in terms of reflectivity and propagation velocity. JMI is able to make use of multiples and at the same time takes velocity variations between different monitoring surveys into account. The simultaneous strategy allows the baseline and monitor parameters to communicate and compensate with each other dynamically during inversion via L2-norm constraints, thus, suppressing the non-repeatable uncertainties during the time-lapse processing. Moreover, in order to get higher resolution time-lapse velocity-differences, we further extended the regular S-JMI to a robust high-resolution S-JMI (HR-S-JMI) process by exploiting the relationship between the reflectivity- and velocity-difference during inversion.

We demonstrated that the performance of time-shift-map-based method, sequential JMI, the regular S-JMI and HR-S-JMI is improving in this particular order, with a complex synthetic example based on the Marmousi model, a highly realistic synthetic model based on the Grane field offshore Norway and a time-lapse field dataset from the Troll Field.

We then investigated the robustness of HR-S-JMI in practice by conducting several numerical experiments based on the realistic Grane model, regarding the following aspects: noise, including random noise and coherent noise caused by the acoustic assumption; the quality of time-lapse surveys, including sparse surveys, non-repeated surveys, and Ocean Bottom Node (OBN) vs Streamer (different types of surveys during monitoring); non-repeated sources, including source positioning error and non-repeated source wavelet; spatial weighting operators in the L2-norm constraint; and sensitivity to weak time-lapse effects. These experiments show that HR-S-JMI is very robust to random noise and coherent noise. It is able to deliver reliable time-lapse differences when the surveys are sparse or mildly changed during monitoring, even when the baseline and monitor datasets are acquired from different types of surveys. Small source positioning errors and source wavelet discrepancy between vintages do not affect the effectiveness of the method, as long as the correct source wavelet is used for each survey. Moreover, the method remains effective when L2-norm constraints are largely relaxed, however, a relaxed version of the L2-norm constraints based on reliable prior information is recommended to achieve less noisy time-lapse changes. Furthermore, HR-S-JMI has the ability to detect weak time-lapse changes. It provides reliable results even in the case when the maximum value of the time-lapse velocity-difference is down to $\pm 35\text{m/s}$. These features make S-JMI a promising solution for inexpensive frequent monitoring.

Therefore, in the end, we proposed S-JMI as an effective processing tool for a cost-effective semi-continuous monitoring survey design, termed i4D survey technology. To further improve the results, calendar-time constraints were proposed and applied to the parameter differences between the baseline and monitors along the calendar-time axis by imposing that time-lapse effects usually develop gradually over time. With a complex synthetic example based on the Marmousi model, we demonstrated that S-JMI is a suitable tool for processing the datasets acquired from semi-continuous monitoring based on such i4D technology.

7.2. RECOMMENDATIONS FOR FURTHER RESEARCH

7.2.1. 3D EXTENSION

Current work is still limited to a 2D assumption, which will limit its application to field data, as the correct physics cannot be described under this 2D assumption. Therefore, a 3D extension is desirable to realize the full potential of the method. The use of multiples can make a more obvious improvement on mitigating 3D acquisition footprints because of the extended illumination provided by multiples. The FWMod, FWM and JMI process can straightforwardly be extended to a full 3D situation [1, 2]. Its implementation in the time-lapse context, however, is left for further research.

7.2.2. INCLUDING AVO EFFECTS

Due to the danger of over-parametrization, the current version of JMI cannot easily handle the angle-versus-offset (AVO) effects in the data when automatic velocity updating is included. Thus, in the time-lapse context, the artifacts in the final model differences brought by the amplitude misfits due to AVO might disguise weak time-lapse effects. In Appendix A, we try to solve this challenge by using a local attribute – local orthogonaliza-

tion – between the modeled and measured data during inversion. However, this strategy is only able to relieve the AVO issue in JMI to some extent and will not provide the final solution. One possible solution is to use another criterion for velocity updating in JMI, e.g. a velocity analysis in the image-domain [3]. However, this image-domain JMI is more expensive, although more robust, and results in a lower resolution in the final velocity update compared to the data-domain JMI. Another possible approach is to scale the amplitudes of the data to remove the AVO effects via deep learning as a pre-processing step. More research on this topic is desired in the future.

7.2.3. INCLUDING ANISOTROPIC EFFECTS

Current work is still based on the assumption that the Earth is isotropic. However, in many real-life time-lapse cases, overburden anisotropy will affect travel-time changes, thus cover up some weak time-lapse effects. Incorporating the anisotropic effects into JMI process has already been discussed in [4]. Applying it to (HR-)S-JMI is desired in order to get reliable results on field data.

7.2.4. TOWARDS TARGET-ORIENTED TIME-LAPSE INVERSION

Current work allows the inversion to only focus on the time-lapse effects on areas of interest via L2-norm constraints based on spatial weighting operators on the model differences. In some situations, e.g. CO_2 sequestration, sudden time-lapse changes are expected through the whole solution space. In this case, the spatial weighting operators should be largely relaxed. There are also many situations where only local time-lapse changes are expected. Therefore, doing inversion in the whole solution space could be a waste during processing. Instead, a target-oriented (HR-)S-JMI for the redatumed datasets on the target region is a much more cost-effective choice.

7.2.5. TOWARDS AMPLITUDE INVERSION AND ELASTIC INVERSION

As was mentioned in the previous chapters, the inverted velocity differences using S-JMI are still smeared. More accurate velocity changes can be acquired using HR-S-JMI by exploiting an approximate relationship between reflectivities and velocity. However, this strategy is an approximate and implicit way to update velocity using amplitude information in the data. Amplitude inversion is a more accurate and explicit way to use amplitude information for the velocity updating. However, it is inapplicable in the whole solution space due to its heavy calculation requirement. Therefore, in order to get more reliable high-resolution time-lapse velocity changes, a target-oriented amplitude inversion is one possible solution [5]. In this case, JMI can be an optimal full-wavefield redatuming tool, which takes all the multiples into account [6].

Moreover, a target-oriented elastic amplitude inversion, which inverts for compressibility and shear compliance, can be an even better solution, because its parameters are more closely related to the final interpretable parameters, e.g. pore pressure and fluid saturation [7].

7.2.6. AUTOMATIC WAY TO CHOOSE THE SPATIAL WEIGHTING OPERATORS

We have investigated the impact of different spatial weighting operators on the time-lapse results in Chapter 5 and came to a conclusion that (HR-)S-JMI remains effective even

when there is no prior information available. However, less noisy velocity- and reflectivity-differences can be obtained by importing prior information via the spatial weighting operators, therefore, a relaxed version of the L2-norm constraints based on prior information is recommended. Sometimes, there is no explicit prior knowledge of the 'truth' available, however, some information is contained implicitly in the data itself. For example, a similarity map between the calculated parameter gradients of different vintages could be used to make a relaxed and flexible weighting operators. A robust and automatic way to decide the spatial weighting operators can be an interesting topic in the further research.

REFERENCES

- [1] M. Davydenko and D. J. Verschuur, *Full wavefield migration in three dimensions*, SEG (Soc. Expl. Geophys., Expanded abstracts, Denver, 2014) pp. 3935–3940.
- [2] B. El-Marhfoul and D. J. Verschuur, *3D joint full wavefield migration of surface and vsp data*, in *SEG Technical Program Expanded Abstracts 2014* (Society of Exploration Geophysicists, 2014) pp. 5070–5074.
- [3] M. Davydenko and D. Verschuur, *Joint imaging of angle-dependent reflectivity and estimation of the migration velocity model using multiple scattering*, *Geophysics* **84** (2019), pp. 1–37.
- [4] A. A. Alshuhail and D. J. Verschuur, *Robust estimation of vertical symmetry axis models via joint migration inversion: Including multiples in anisotropic parameter estimation*, *Geophysics* **84** (2019), pp. C57–C74.
- [5] D. Yang, Y. Zheng, M. Fehler, and A. Malcolm, *Target-oriented time-lapse waveform inversion using virtual survey*, in *SEG Technical Program Expanded Abstracts 2012* (Society of Exploration Geophysicists, 2012) pp. 1–5.
- [6] A. Garg, S. Sharma, and D. J. Verschuur, *Reservoir elastic parameters estimation from surface seismic data using JMI-res: A full-wavefield approach*, in *80th EAGE Conference and Exhibition 2018* (Eur. Ass. of Geosc. and Eng., Expanded abstracts, 2018).
- [7] P. Haffinger, F. J. Eyvazi, P. Doulgeris, P. Steeghs, D. Gisolf, and E. Verschuur, *Quantitative prediction of injected CO2 at sleipner using wave-equation based AVO*, *First Break* **35** (2017), pp. 65–70.

A

APPENDIX A: MITIGATING AVO EFFECTS IN JMI USING LOCAL ORTHOGONALIZATION

Joint migration inversion (JMI) is a recently proposed full wavefield inversion method, which tries to minimize the mismatch between observed reflection data and forward modeled data. Transmission effects and surface/internal multiples are included in the forward modeling process using a multi-dimensional version of the Bremmer series. However, since the current implementation of JMI uses an angle-independent reflectivity model, it cannot easily handle large-offset data due to the angle-versus-offset (AVO) effects. In this work, we propose to mitigate this AVO challenge in JMI using a local attribute – local orthogonalization – between the modeled and recorded data during inversion. The local orthogonalization weight indicates those areas of modeled data that do not correlate with the recorded data. Afterwards, the high orthogonalization part containing strong AVO effects is subtracted from the residual adaptively based on the orthogonalization weight. We demonstrate the effectiveness of our proposed method with a complex synthetic example based on the Marmousi model.

A.1. INTRODUCTION

As was discussed in the previous chapters in this thesis, Joint Migration Inversion (JMI) is an inversion algorithm that automatically derives both a reflectivity model (i.e. the image) and a propagation velocity model in the least-squares sense based on full wave-field modeling (FWMod) [1]. This modeling takes into account transmission effects and surface/internal multiples [2]. The forward modeling of JMI simulates the data in a way that amplitudes are defined by the estimated reflectivities, whereas travel-times are separately controlled by the velocity model. This separation should help to reduce the non-linearity in the inversion process [3]. Currently in JMI, velocity and reflectivity models are estimated in a flip-flop manner. However, due to the angle-independent reflectivity model, JMI cannot correctly match the part of the recorded data where includes strong AVO effects, e.g. the large offset parts, so for the time being JMI is only capable of handling limited-offsets. In order to physically describe the AVO characteristics in the data, angle-dependent reflectivities should be considered [4], but in JMI this will result in over-parametrization in the inversion, i.e. it may lead to a wrong velocity update which can still help to minimize the data misfit. In order to mitigate AVO issue of JMI, [5] proposed to do the velocity update in the image-domain, so that angle-dependent reflectivity model can be estimated while avoiding over-parametrization. However, this image-domain JMI is more expensive, although more robust, and results in lower resolution in the final velocity update compared to the data-domain JMI. [6] proposed to use a new objective function, called zero-lag cross-correlation objective function of normalized redatumed wave-fields, to help relax the requirement for the strong amplitude matching in the least-squares sense. Numerically, they normalized the redatumed residual, instead of surface residual, to mitigate the AVO mismatch adaptively at different depth levels, because the AVO effects vary for different events. However, because the normalization is still done linearly in a trace-by-trace manner, when it comes to very complex model generating strong AVO effects, this method fails. Therefore, using a local seismic attribute map to detect and scale the AVO mismatch area in the residual might be a solution.

Local seismic attributes measure seismic signal characteristics locally in the neighbourhood of each point [7]. One of the most useful local attributes is local similarity, which has found successful applications in different areas of seismic data processing: image registration [8, 9], velocity analysis [10, 11], time-frequency analysis [12], structure-enhancing filtering [13–15], etc. Another local attribute is called local orthogonalization [16], which has been successfully applied to random noise removal [16] and ground-roll noise attenuation [17].

In this work, we propose a robust AVO-preserving JMI based on scalar reflectivities with the help of a local attribute – local orthogonalization weight – between the modeled and recorded data during inversion. The local orthogonalization weight is calculated in a least-squares sense with the help of shaping regularization and it is able to indicate the part of modeled data that does not correlate with the recorded data. The high orthogonalization part mostly contains the strong AVO effects, which cannot be explained by JMI with scalar reflectivities. This mismatch due to AVO effects is then subtracted from the residual adaptively based on the local orthogonalization weight. We demonstrate the effectiveness of our proposed method using a complex synthetic example based on the Marmousi model.

A.2. AVO-PRESERVING JMI WITH LOCAL ORTHOGONALIZATION

[16] proposed a local orthogonalization approach for retrieving useful signals from the noise section based on the assumption that the final estimated signal and noise should be orthogonal to each other. In this work, we calculate the local orthogonalization weight between the modeled and recorded data shot by shot during inversion. We then subtract the AVO amplitude mismatch from the residual wavefield adaptively based on the local orthogonalization weight.

The local orthogonalization weights imply which part of modeled data does not correlate well with the recorded data, e.g. high AVO effects and random noise. We define one shot profile, which is collapsed into one dimension, of the modeled and recorded data in the time-domain as \mathbf{p}_0^- and \mathbf{d}_0^- , respectively. The local orthogonalization weight \mathbf{w} is calculated in a least-squares sense as follows [16]:

$$\mathbf{w} = \arg \min_{\mathbf{w}} \|\mathbf{d}_0^- - \text{diag}(\mathbf{p}_0^- \mathbf{w})\|_2^2. \quad (\text{A.1})$$

Here, $\text{diag}(\mathbf{p}_0^-)$ is a diagonal matrix composed of \mathbf{p}_0^- . Then the least-squares problem A.1 is solved with the help of shaping regularization [18] using a local-smoothness constraint:

$$\mathbf{w} = [\lambda^2 \mathbf{I} + \mathcal{T}(\text{diag}(\mathbf{p}_0^-)^T \text{diag}(\mathbf{p}_0^-) - \lambda^2 \mathbf{I})]^{-1} \mathcal{T} \text{diag}(\mathbf{p}_0^-)^T \mathbf{d}_0^-, \quad (\text{A.2})$$

where \mathcal{T} is a triangle smoothing operator and λ is a scaling parameter set as

$$\lambda = \|\text{diag}(\mathbf{p}_0^-)^T \text{diag}(\mathbf{p}_0^-)\|_2.$$

By assuming that the high local orthogonalization weight, which is windowed by a threshold, indicates the part of residual with strong AVO amplitude mismatch and random noise. We can obtain the new residual wavefields $\mathbf{e}_{0,new}^-$:

$$\mathbf{e}_{0,new}^- = \begin{cases} \mathbf{d}_0^- - \text{diag}(\mathbf{p}_0^-) \mathbf{w} & \mathbf{w} \geq \epsilon \max(\mathbf{w}) \\ \mathbf{d}_0^- - \mathbf{p}_0^- & \text{otherwise,} \end{cases} \quad (\text{A.3})$$

where $*$ denotes element-wise multiplication and ϵ is a pre-set threshold and usually set to 0.2. This threshold is used to detect the relatively high local orthogonalization weights. It can be observed that the part of the new residual, where the local orthogonalization weight is relatively low, remains the same as the original residual, because low weight means a good match between the modeled and measured data. While the rest of the residual, where the weight is relatively high, is scaled adaptively based on this local weight.

The controlling parameter for calculating the local weight is the smoothing radius of the triangle smoother. As the smoothing radius increases, the temporal and spatial resolutions of the weight decrease, but it indicates the AVO amplitude mismatch more robustly. In order to relieve the calculation efforts, local orthogonalization weights are only updated around every 25 iterations.

A.3. EXAMPLE

In order to demonstrate the effectiveness of the proposed method, we consider the models shown in Figures A.1(a) and A.1(b), which are scaled from the top half of the Marmousi model. The dataset in this section is generated via acoustic finite difference modelling

using both the density and velocity model. The source spacing is set to $100m$, and the receiver spacing to $20m$. We use a Ricker wavelet with $20Hz$ peak frequency. 20% random noise energy is added to the generated dataset. The band-width of frequency during JMI is $5Hz - 40Hz$. Surface multiples are excluded in the modelling, but internal multiples are included. Initially, reflectivities are shown in Figure A.1(d) and the velocity is shown in figure A.1(c), which is a strongly smoothed version of figure A.1(d).

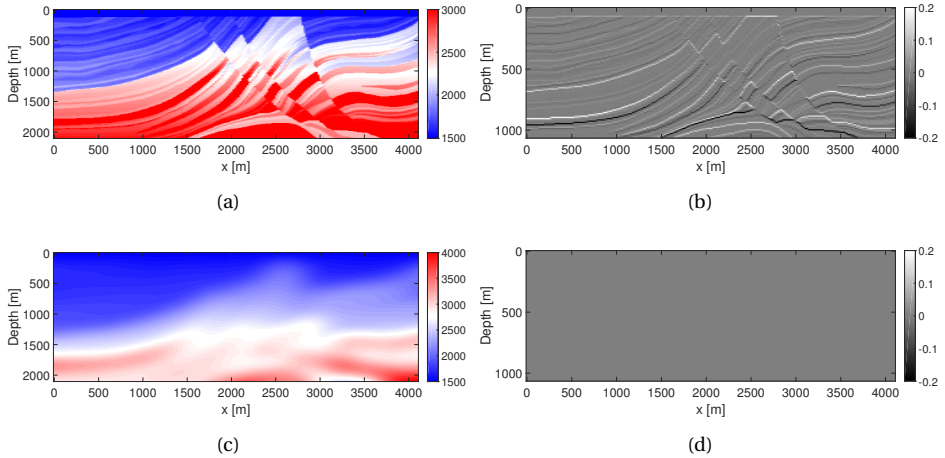


Figure A.1: AVO-preserving JMI: (a) and (b) the true velocity and reflectivity model; (c) and (d) initial velocity and reflectivity model.

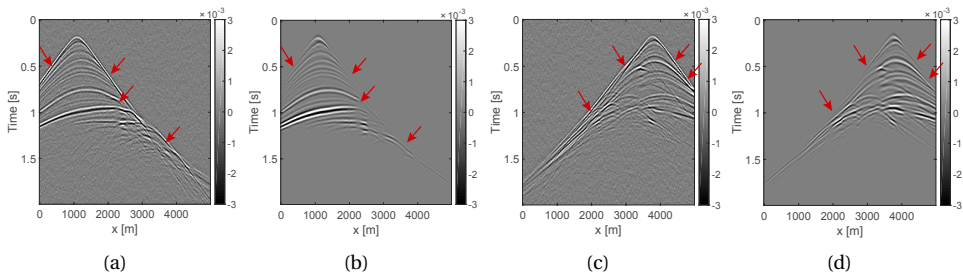


Figure A.2: AVO-preserving JMI: the recorded data \mathbf{d}_0^- generated using the finite-difference modeling and the modeled data \mathbf{p}_0^- using FWMod with the scalar reflectivity assumption at a late iteration during JMI: (a) and (b) at $X = 1000m$; (c) and (d) at $X = 3200m$.

We compare two strategies: the conventional JMI and the proposed AVO-preserving JMI with the help of local orthogonalization. Two recorded shot profiles \mathbf{d}_0^- (generated using the finite-difference modeling at the beginning) and modeled shot profiles \mathbf{p}_0^- (modeled with FWMod in JMI with the scalar reflectivity assumption) at a late iteration are

shown in Figures A.2 ($X = 1000m$ and $X = 3200m$). We can clearly observe high amplitudes at larger offsets (pointed with red arrows) in the recorded data, whereas, FWMod is not able to generate these AVO effects due to the scalar reflectivity assumption. Moreover, the AVO effects in the data are different for different events and shallower events normally have stronger AVO effects at smaller offsets compared to the deeper events.

Due to the inversion process included in JMI, the inverted image using the conventional JMI is quite accurate and the estimated velocity model also shows some details (shown in Figure A.3). However, because the AVO amplitude effects cannot be modeled in JMI, there are clearly visible low-frequency artifacts in the inverted reflectivity. Note that, as was mentioned in Chapter 2, the reflectivity model in JMI explains the amplitude mismatch in the residual, meanwhile, the phase mismatch is explained by the velocity model. Therefore, there are some artifacts pointed out by the black arrows in the velocity model due to the AVO effects, but they are not as obvious as those in the reflectivity model.

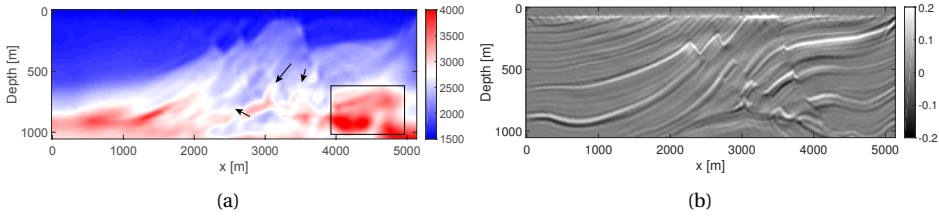


Figure A.3: AVO-preserving JMI: (a) and (b) the inverted velocity and reflectivity model using conventional JMI.

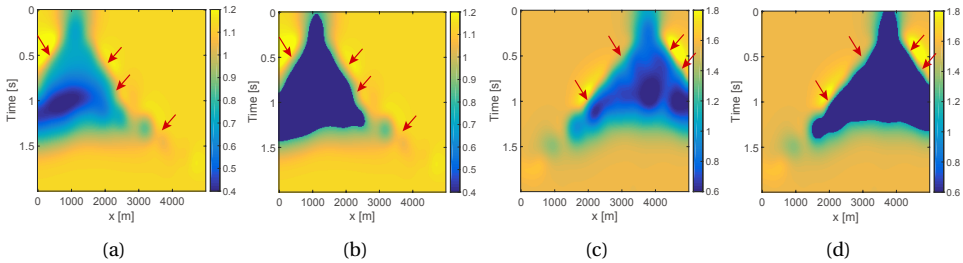


Figure A.4: AVO-preserving JMI: the estimated local orthogonalization weight \mathbf{w} and the windowed version $\Lambda * \mathbf{w}$: (a) and (b) between Figures A.2(a) and A.2(b); (c) and (d) between Figures A.2(c) and A.2(d).

The estimated local orthogonalization weights \mathbf{w} between the recorded and the modeled data are shown in Figures A.4(a) and A.4(c) and the windowed ones $\Lambda * \mathbf{w}$ are shown in Figures A.4(b) and A.4(d). We can see that the local orthogonalization map is able to detect the area with high AVO amplitude mismatch. The corresponding conventional residual \mathbf{e}_0^- and the new residual $\mathbf{e}_{0,new}^-$ are shown in Figures A.5. The AVO mismatch is nicely

suppressed in Figures A.5(b) and A.5(d) compared to Figures A.5(a) and A.5(c). They are highlighted by red arrows. In addition, the random noise in the new residual, which also has high orthogonalization weight, is attenuated.

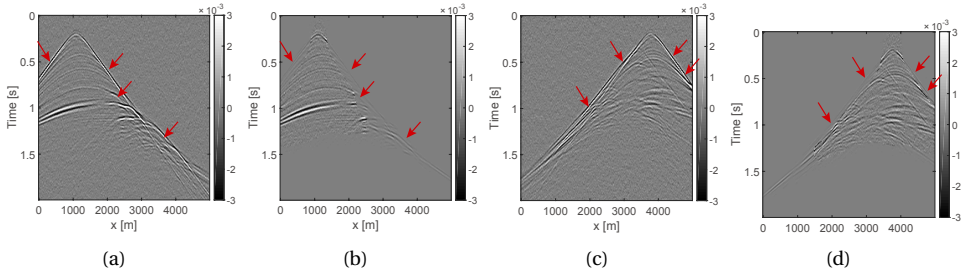


Figure A.5: AVO-preserving JMI: the conventional residual \mathbf{e}_0^- and the new residual $\mathbf{e}_{0,new}^-$ using the proposed method: (a) and (b) between Figures A.2(a) and A.2(b); (c) and (d) between Figures A.2(c) and A.2(d).

Based on the new residual calculated with the high local orthogonalization weight, the proposed AVO-preserving JMI achieves much better results, which are shown in Figures A.6. The inverted reflectivity model in Figure A.6(a) is significantly improved with barely no low-frequency artifacts and much better resolution, compared to figure A.3(a). Moreover, in the inverted velocity model in Figure A.6(b), some of the artifacts are suppressed and more details (highlighted by black arrows and square) are recovered, especially in the deeper part.

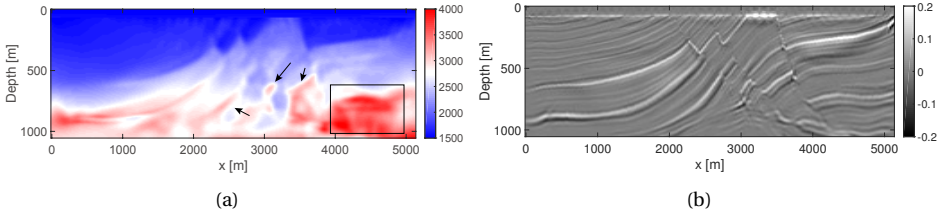


Figure A.6: AVO-preserving JMI: (a) and (b) the inverted velocity and reflectivity model using the proposed AVO-preserving JMI.

A.4. CONCLUSION

In order to mitigate the AVO challenge in JMI, we propose AVO-preserving JMI using the local orthogonalization between the modeled and recorded data during inversion. The local orthogonalization weight is able to indicate the part of modeled data that does not correlate with the recorded data. The high orthogonalization part usually contains the strong AVO effects and are then subtracted from the residual based on the orthogonalization weight, thereby, reducing its negative impacts on the updating process. Thus, the

inverted model has a higher resolution than that from the traditional JMI framework without considering the AVO effect. Our synthetic test based on the Marmousi model demonstrates the effectiveness of the proposed method.

REFERENCES

- [1] A. J. Berkhout, *Review paper: An outlook on the future of seismic imaging, Part I: forward and reverse modelling*, *Geophysical Prospecting* **62** (2014), pp. 911–930.
- [2] A. J. Berkhout, *Review paper: An outlook on the future of seismic imaging, Part II: Full-wavefield migration*, *Geophysical Prospecting* **62** (2014), pp. 931–949.
- [3] D. J. Verschuur, X. R. Staal, and A. J. Berkhout, *Joint migration inversion: Simultaneous determination of velocity fields and depth images using all orders of scattering*, *The Leading Edge* **35** (2016), pp. 1037–1046.
- [4] M. Davydenko and D. J. Verschuur, *Full-wavefield migration: using surface and internal multiples in imaging*, *Geophysical Prospecting* **65** (2017), pp. 7–21.
- [5] M. Davydenko and D. J. Verschuur, *Full-wavefield estimation of angle-dependent reflectivity and migration velocity*, in *SEG Technical Program Expanded Abstracts 2017* (Society of Exploration Geophysicists, 2017) pp. 5631–5635.
- [6] S. Qu, Y. Sun, and E. Verschuur, *Mitigating amplitude versus ray-parameter effect in joint migration inversion using a zero-lag crosscorrelation objective function of redatumed wavefields*, in *SEG Technical Program Expanded Abstracts 2018* (Society of Exploration Geophysicists, 2018) pp. 1133–1137.
- [7] S. Fomel, *Local seismic attributes*, *Geophysics* **72** (2007), pp. A29–A33.
- [8] S. Fomel, M. Backus, K. Fouad, B. Hardage, and G. Winters, *A multistep approach to multicomponent seismic image registration with application to a West Texas carbonate reservoir study*, *75th Annual International Meeting, SEG, Expanded Abstracts* (2005), pp. 1018–1021.
- [9] S. Fomel and L. Jin, *Time-lapse image registration using the local similarity attribute*, *Geophysics* **74** (2009), pp. A7–A11.
- [10] Y. Chen, T. Liu, and X. Chen, *Velocity analysis using similarity-weighted semblance*, *Geophysics* **80** (2015), pp. A75–A82.
- [11] S. Gan, S. Wang, Y. Chen, S. Qu, and S. Zu, *Velocity analysis of simultaneous-source data using high-resolution semblance-coping with the strong noise*, *Geophysical Journal International* **204** (2016), pp. 768–779.
- [12] G. Liu, S. Fomel, and X. Chen, *Time-frequency analysis of seismic data using local attributes*, *Geophysics* **76** (2011), pp. P23–P34.
- [13] Y. Liu, S. Fomel, and G. Liu, *Nonlinear structure-enhancing filtering using plane-wave prediction*, *Geophysical Prospecting* **58** (2010), pp. 415–427.

- [14] S. Gan, S. Wang, Y. Chen, X. Chen, and K. Xiang, *Separation of simultaneous sources using a structural-oriented median filter in the flattened dimension*, *Computers & Geosciences* **86** (2016), pp. 46–54.
- [15] Y. Chen, S. Zu, Y. Wang, and X. Chen, *Deblending of simultaneous-source data using a structure-oriented space-varying median filter*, *Geophysical Journal International* **216** (2019), pp. 1214–1232.
- [16] Y. Chen and S. Fomel, *Random noise attenuation using local signal-and-noise orthogonalization*, *Geophysics* **80** (2015), pp. WD1–WD9.
- [17] Y. Chen, S. Jiao, J. Ma, H. Chen, Y. Zhou, and S. Gan, *Ground-roll noise attenuation using a simple and effective approach based on local band-limited orthogonalization*, *IEEE Geoscience and Remote Sensing Letters* **12** (2015), pp. 2316–2320.
- [18] S. Fomel, *Shaping regularization in geophysical-estimation problems*, *Geophysics* **72** (2007), pp. R29–R36.
- [19] C. Bunks, F. M. Saleck, S. Zaleski, and G. Chavent, *Multiscale seismic waveform inversion*, *Geophysics* **60** (1995), pp. 1457–1473.

B

APPENDIX B: JMI WITH AN AUTOMATIC DIRECTIONAL TOTAL VARIATION CONSTRAINT

Joint migration inversion (JMI) is a recently proposed full wavefield inversion method, explaining the reflection data with decoupled velocity and reflectivity parameters. This assumption of scale separation helps to reduce the non-linearity of inversion problem. However, the velocity update may still suffer from being trapped in local minima. To optimally include geologic information, we propose JMI with directional total variation as an L1-norm regularization on the velocity. We design the directional total variation operator based on the local dip field, instead of ignoring the local structural direction of the subsurface and only using horizontal- and vertical-gradients in the traditional TV. The local dip field is estimated using plane-wave destruction based on a raw reflectivity model, which is usually calculated from the initial velocity model. With a complex synthetic example based on the Marmousi model, we demonstrate that the proposed method is much more effective compared to JMI without regularization, JMI with the conventional TV regularization, and JMI with L2 directional Laplacian smoothing.

B.1. INTRODUCTION

Seismic full waveform inversion (FWI) is a powerful method for providing a quantitative description of the subsurface properties by iteratively minimizing an objective function that measures the misfit between observed and predicted data in the least-squares sense [1]. However, FWI is a non-linear and ill-posed inverse problem and its objective function may suffer from local minima that are not informative about the true parameters [2]. Using regularization methods is an effective way to mitigate this ill-posedness and non-uniqueness of FWI.

Joint Migration Inversion (JMI) was proposed as one of the methods to overcome the above-mentioned limitations in FWI [3–5]. It is an inverse algorithm to automatically derive both velocity and reflectivity based on the full wavefield modeling (FWMoD) process [6] that takes transmission effects and surface/internal multiples into account. In the FWMoD procedure, the velocity only affects the kinematics without any scattering effect in the modeling operators and the reflectivities only deal with scattering effects. These characteristics lead to a reduced non-linearity in the inversion process. Even though not as severe as FWI, the velocity update may still suffer from being trapped in local minima. With the help of regularization, JMI can get a more accurate inverted velocity, and thus achieve a better inverted reflectivity [7, 8].

The popular regularization methods include: quadratic L2-norm-based regularization, such as Tikhonov regularization [9], and laplacian smoothing [10–12], which tend to produce models with blurred discontinuities; non-quadratic L1-norm-based regularization, such as total variation (TV) [7, 13], smooths the model by enhancing the sparsity of the spatial gradient of the velocity, thereby preserving its edges. However, regular TV regularization only tends to reduce the horizontal and vertical gradients of each gridpoint in the model regardless of their structural direction. Thus, TV is not suitable where the local geologic structure has a dominant structural direction. Unlike general digital images, the spatial changes of the seismic model always have some specific geological structures, like tilted layers, faults, or edges of a salt body. [14] proposed a directional TV method and applied it to digital image denoising. However, they only consider one single dominant direction for all pixels, which is obviously ineffective for complex-textured geologies. Therefore, we propose a directional TV constraint based on a rough estimate of the subsurface image.

This appendix is organized as follows: we first formulate the conventional TV and the proposed directional TV. Finally, with a complex Marmousi-model-based example, we show that the proposed method is more effective than the alternative methods, when the model contains tilted layers and steep faults. In the end, we also show that the L1 directional TV works better than the L2 directional Laplacian smoothing regarding the preservation of edges and the steering of the update away from the local minimum. Note that this work is published in [15], where also FWI with (directional) TV was described.

B.2. JMI WITH TV AND DIRECTIONAL TV

In this work, we consider anisotropic TV as the basic regularization method, since TV can smooth the model and at the same time preserve edges by enhancing the sparsity of the spatial gradient of the velocity difference. In addition, the anisotropic version is easier

to minimize compared to the isotropic one. Furthermore, we restrict ourselves to the 2D case, although extension to the full 3D situation is relatively straightforward.

The extended objective function of JMI with a TV constraint can be expressed as

$$J_{tot} = \mu J_{JMI} + \lambda C_{TV}(\mathbf{v}) = \mu J_{JMI} + \lambda \|\nabla_x \mathbf{v}\|_1 + \lambda \|\nabla_z \mathbf{v}\|_1. \quad (\text{B.1})$$

Here, J_{JMI} the objective function of JMI in a least-squares sense, which was described in equation 2.9 in Chapter 2. \mathbf{v} is the propagation velocity constrained by TV. ∇_x and ∇_z represent horizontal- and vertical-gradient operator, respectively. For one gridpoint (i, j) in a cartesian coordinate (x, z) , $\nabla_x \mathbf{v}(i, j) = v_{i+1, j} - v_{i, j}$ and $\nabla_z \mathbf{v}(i, j) = v_{i, j+1} - v_{i, j}$ (illustrated in Figure B.1(a) with the black dashed arrows). μ is the weight parameter of the fidelity term. λ is the coefficient of the constraint term. The latter two together control the balance between the regularization and the misfit function.

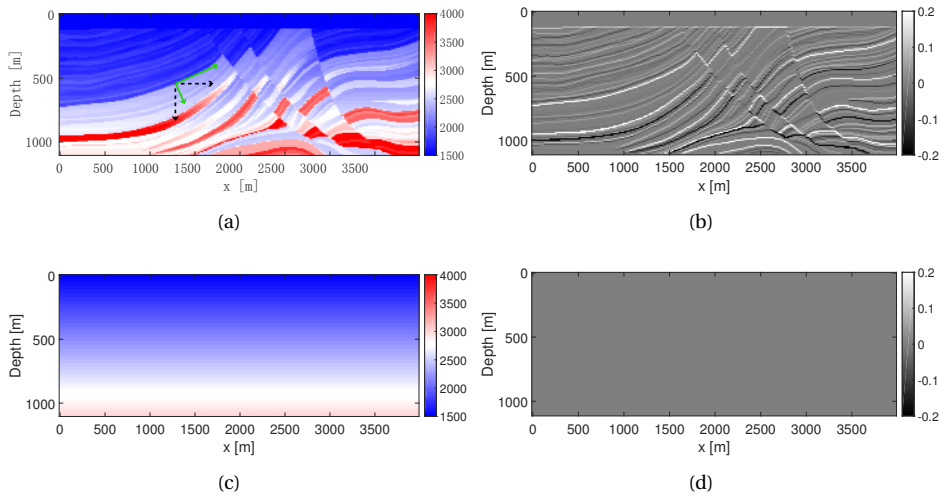


Figure B.1: DTW: (a) and (b) the true velocity and reflectivity model; (c) and (d) the initial velocity and reflectivity model. The black dash arrows illustrate $\nabla_x \mathbf{v}(i, j)$ and $\nabla_z \mathbf{v}(i, j)$, the green solid arrows illustrate $\nabla_1 \mathbf{v}(i, j)$ and $\nabla_2 \mathbf{v}(i, j)$, based on the structural dip at (i, j) .

However, this conventional TV regularization only tends to reduce the horizontal- and vertical-gradients of each gridpoint in the model, regardless of the geological direction of the model. Therefore, TV is not suitable where the local structure has a dominant direction. Unlike general digital images, the spatial changes in the subsurface always follow some specific geological structures, e.g., tilted layers, faults, and edges of a salt body. In this case, we propose JMI with directional TV and we design the directional TV based on the local dip estimated from a rough reflection image using the plane-wave destruction (PWD) algorithm [16].

The misfit function with directional TV can be formulated as

$$J_{tot} = \mu J_{JMI} + \lambda C_{DTV}(\mathbf{v}) = \mu J_{JMI} + \lambda \|\nabla_1 \mathbf{v}\|_1 + \lambda \|\nabla_2 \mathbf{v}\|_1, \quad (\text{B.2})$$

where ∇_1 and ∇_2 are the gradient operators of the dominant direction and the direction perpendicular to the dominant direction, respectively. From the viewpoint of physical meaning, ∇_1 and ∇_2 are the rotated and scaled version of ∇_x and ∇_z , according to the estimated local dip and a weighting parameter. Mathematically, for one point (i, j) , $\nabla_1 \mathbf{v}(i, j)$ and $\nabla_2 \mathbf{v}(i, j)$ can be represented as

$$\begin{aligned} \begin{pmatrix} \nabla_1 \mathbf{v}(i, j) \\ \nabla_2 \mathbf{v}(i, j) \end{pmatrix} &= \Lambda \mathcal{R} \begin{pmatrix} \nabla_x \mathbf{v}(i, j) \\ \nabla_z \mathbf{v}(i, j) \end{pmatrix} \\ \text{Here } \Lambda &= \begin{pmatrix} \alpha_1 & 0 \\ 0 & \alpha_2 \end{pmatrix}, \mathcal{R} = \begin{pmatrix} \cos \theta & -\sin \theta \\ \sin \theta & \cos \theta \end{pmatrix}, \end{aligned} \quad (\text{B.3})$$

where Λ and \mathcal{R} represent scaling matrix and rotation matrix, respectively. α_1 and α_2 represent the weights on the gradient of the dominant direction and its perpendicular direction, respectively, and θ is the dip of the local structure. An illustration of such a directional TV is shown in Figure B.1(a) with the green solid arrows.

Please note that if we assume $\alpha_1 = \alpha_2 = 1$ and $\theta = 0^\circ$, then Λ turns into an identity matrix, which means the same weights are put on both directions, and \mathcal{R} also becomes an identity matrix, indicating that the target directions are horizontal and vertical. Therefore, we can see that the conventional TV is actually a special case of the directional TV, and in turn, the directional TV is a more general version of the conventional TV and more suitable to a model with complex geologic structures. In this work, we solve JMI with the conventional TV and directional TV effectively using the split-Bregman iterative algorithm [17].

B.3. EXAMPLE

In order to demonstrate the effectiveness of the proposed method, we consider the same synthetic model as the example in Appendix A being shown in Figures B.1(a) and B.1(b). Ricker wavelet with a dominant frequency of 20Hz is used as the source wavelet. The shot spacing is 200 m and the receiver spacing is 20 m. The horizontal and vertical grid size are 20 m and 10 m, respectively. Surface multiples are excluded in the modeling, but internal multiples and transmission effects are included. The direct wave is removed, as it cannot be explained by JMI. Initially, reflectivities are zero and the initial velocity is a very simple vertical gradient, which is even simpler than the initial velocity model used in Appendix A being shown in Figure B.1(d)). First, with the initial model, we apply 30 iterations of JMI with 5Hz – 25Hz frequency bandwidth to the dataset and then denoise the inverted image via a simple soft-thresholding in the curvelet domain [18]. Then, with this preprocessed inverted reflectivity shown in Figure B.2(b), we can estimate the dip field using plane-wave destruction algorithm proposed by [16], shown in Figure B.2(c). This estimated dip field is then used to build the directional TV operators for each gridpoint. Meanwhile, the inverted velocity in Figure B.2(a) can be used as an initial velocity model for the next step.

Next, we compare results from the regular JMI without any regularization, JMI with conventional TV, JMI with directional TV and JMI with L2 directional Laplacian smoothing. The frequency bandwidth during the second step of JMI is 5Hz – 40Hz. We use the same μ and λ for both the conventional TV and directional TV. μ is also increasing with

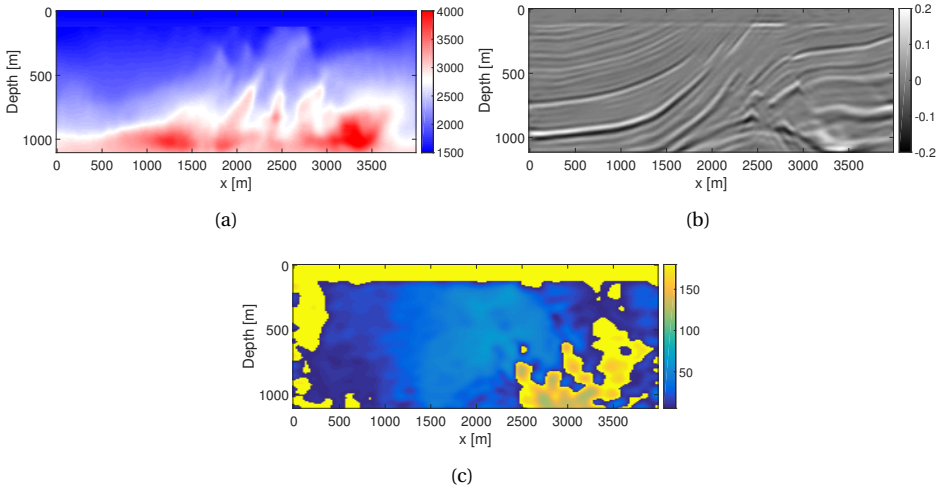


Figure B.2: DTV: the inverted velocity (a) and the denoised inverted reflectivity model (b) using JMI with 5 Hz – 25 Hz frequency bandwidth. (c) The estimated dip field (in degrees).

iteration and $\lambda = 1.2$. For directional TV, $\alpha_1 : \alpha_2 = 3 : 1$ and $\alpha_1 + \alpha_2 = 2$. For the conventional TV, Λ is an identity matrix. After 50 iterations for each method, the inverted results are shown in Figures B.3 and B.4. Because of the inversion process included in JMI, all the estimated velocity models in Figure B.4 are surprisingly stable and show some details. Moreover, all the images in Figure B.3 are quite accurate compared to the true reflectivity structures.

In Figure B.3(a), the regular JMI without any regularization is slightly trapped in a local minimum, e.g., in the lower right area pointed by the green arrow. With the help of TV regularization, JMI with conventional TV in Figure B.3(b) achieves a better result by smoothing the model via enhancing the sparsity of the spatial gradient of the velocity difference, which allows us to steer away from the local minimum. Instead of using the conventional TV, a much better inverted velocity with more clear edges of structures is obtained in Figure B.3(c) using JMI with directional TV. This is because we consider the structural directions of the spatial gradient and their weights according to the local dip from the associated image. Please note some obvious improvements pointed out by the black arrows. In addition, compared to L1 directional TV, L2 directional Laplacian smoothing results in a smoother velocity model being shown in Figure B.3(d); however, it intensifies the local minima issue and tends to produce models with blurred discontinuities. That is because the directional Laplacian smoothing may over-smooth the velocity and cannot preserve edges very well; it is also more sensitive to the accuracy of the estimated dip field, compared to L1 directional TV. As a result of the improvement of the inverted velocity result, the inverted reflectivity model also becomes more accurate (Figure B.4): the inverted reflectivities highlighted with white arrows in Figure B.4(c) have better focusing and less distortions than the other alternatives.

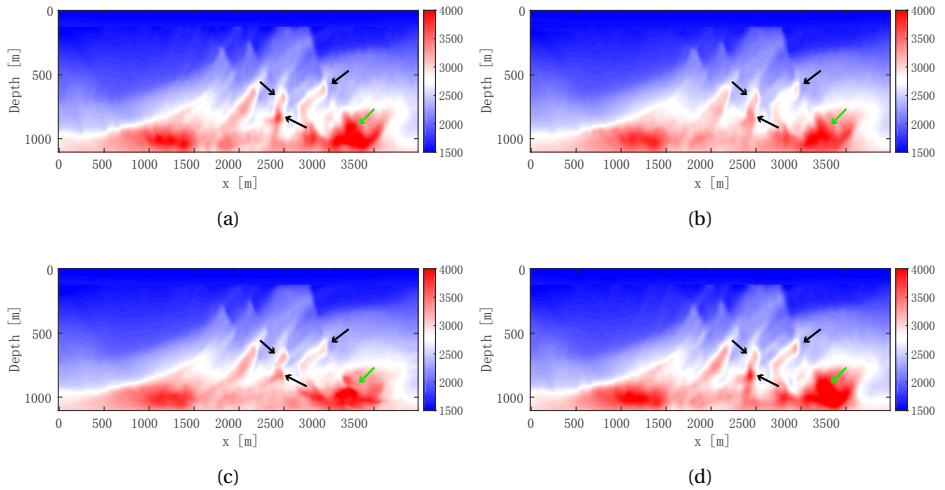


Figure B.3: DTV: The inverted velocity using (a) regular JMI without any regularization, (b) JMI with conventional TV, (c) JMI with directional TV, and (d) JMI with L2 directional laplacian smoothing.

B.4. DISCUSSION

JMI with directional TV has been demonstrated to be a more effective method than the alternatives. We design the directional TV based on the dip field calculated from an initial image. By considering the local structural directions of the spatial gradient and their weights according to the local dip, the proposed method achieves a better result compared to JMI without regularization or with conventional TV. In the case of complex subsurface structures, the local dip map cannot be estimated properly. However, directional TV regularization is not sensitive to the accuracy of the estimated dip, because even using an arbitrary dominant direction would not be worse than using horizontal- and vertical-gradients, which means using conventional TV in a complex area.

In terms of the parameter selection, we choose a relaxation strategy for μ , which is increasing exponentially. In this way, we relax the strength of the L1 constraint gradually to make the inversion converge. λ is a constant which depends on the scale of the data. We can set a proper λ to make sure around 60% – 70% of the energy is passed through the shrinkage step in the split-Bregman iterative algorithm, in order to improve the stability of the algorithm. Regarding the weights on the dominant direction and its perpendicular direction of gradients, it depends on the accuracy of the estimated dip field and the bias of the subsurface structures. Usually, $\alpha_1 : \alpha_2 = 2 : 1$ is a safe choice. In this work, we use $\alpha_1 : \alpha_2 = 3 : 1$ for both examples, which puts more weight on the dominant spatial direction of the velocity gradient, because the structures of the Marmousi model are quite tilted and biased.

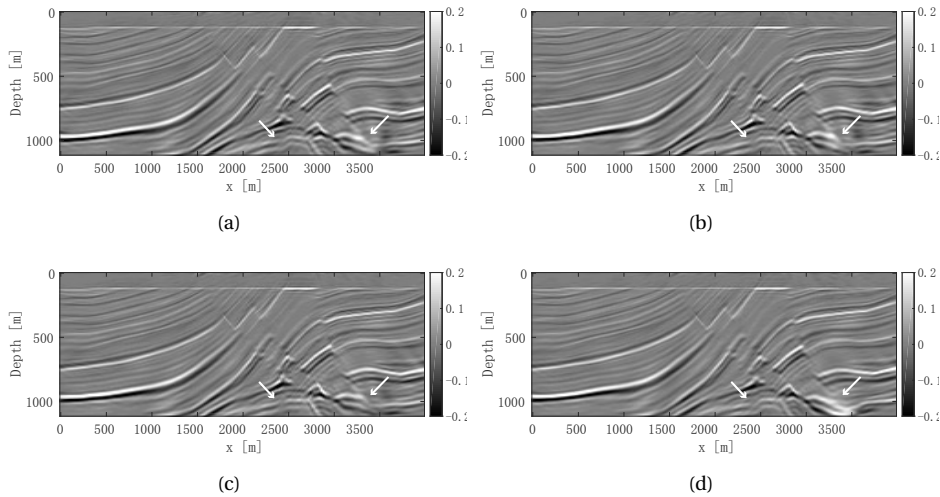


Figure B.4: DTV: The inverted reflectivity model using (a) regular JMI without any regularization, (b) JMI with conventional TV, (c) JMI with directional TV, and (d) JMI with L2 directional Laplacian smoothing.

B.5. CONCLUSION

Joint migration inversion (JMI) with the directional total variation (TV) has been demonstrated to be a more effective method than the alternatives (i.e., JMI without regularization, with the conventional TV, or L2 directional Laplacian smoothing). We designed the directional TV based on the dip field calculated from a raw image. By considering the local structural directions of the spatial gradient and their weights according to the local dip, the proposed method achieves a better result compared to JMI without regularization or with conventional TV.

REFERENCES

- [1] A. Tarantola, *Inversion of seismic reflection data in the acoustic approximation*, *Geophysics* **49** (1984), pp. 1259–1266.
- [2] J. Virieux and S. Operto, *An overview of full-waveform inversion in exploration geophysics*, *Geophysics* **74** (2009), pp. WCC127 – WCC152.
- [3] A. J. Berkhout, *Review paper: An outlook on the future of seismic imaging, Part II: Full-wavefield migration*, *Geophysical Prospecting* **62** (2014), pp. 931–949.
- [4] X. R. Staal, *Combined imaging and velocity estimation by Joint Migration Inversion*, *Ph.D. thesis*, Delft University of Technology (2015).
- [5] D. J. Verschuur, X. R. Staal, and A. J. Berkhout, *Joint migration inversion: Simulta-*

- neous determination of velocity fields and depth images using all orders of scattering*, *The Leading Edge* **35** (2016), pp. 1037–1046.
- [6] A. J. Berkhout, *Review paper: An outlook on the future of seismic imaging, Part I: forward and reverse modelling*, *Geophysical Prospecting* **62** (2014), pp. 911–930.
- [7] S. Qu and D. J. Verschuur, *Simultaneous time-lapse imaging via joint migration and inversion*, in *78th EAGE Conference and Exhibition 2016* (Eur. Ass. of Geosc. and Eng., Expanded abstracts, 2016).
- [8] S. Qu and D. Verschuur, *Simultaneous joint migration inversion for semicontinuous time-lapse seismic data*, in *SEG Technical Program Expanded Abstracts 2017* (Society of Exploration Geophysicists, 2017) pp. 5808–5813.
- [9] W. Hu, A. Abubakar, and T. M. Habashy, *Simultaneous multifrequency inversion of full-waveform seismic data*, *Geophysics* **74** (2009), pp. R1–R14.
- [10] A. Guitton, G. Ayeni, and E. Díaz, *Constrained full-waveform inversion by model reparameterization*, *Geophysics* **77** (2012), pp. R117–R127.
- [11] S. Qu and D. J. Verschuur, *Getting accurate time-lapse information using geology-constrained simultaneous joint migration-inversion*, in *SEG Technical Program Expanded Abstracts 2016* (Society of Exploration Geophysicists, 2016) pp. 5451–5456.
- [12] S. Qu and D. J. Verschuur, *Simultaneous joint migration inversion for accurate time-lapse analysis of sparse monitor surveys*, in *First EAGE Workshop on Practical Reservoir Monitoring* (Eur. Ass. of Geosc. and Eng., Expanded abstracts, 2017).
- [13] A. Y. Anagaw and M. D. Sacchi, *Full waveform inversion with total variation regularization*, in *Recovery-CSPG CSEG CWLS Convention* (2011).
- [14] I. Bayram and M. E. Kamasak, *Directional total variation*, *IEEE Signal Processing Letters* **19** (2012), pp. 781–784.
- [15] S. Qu, E. Verschuur, and Y. Chen, *Full waveform inversion and joint migration inversion with an automatic directional total variation constraint*, *Geophysics* **84** (2018), pp. 1–37.
- [16] S. Fomel, *Applications of plane-wave destruction filters*, *Geophysics* **67** (2002), pp. 1946–1960.
- [17] T. Goldstein and S. Osher, *The split Bregman method for L1-regularized problems*, *SIAM journal on imaging sciences* **2** (2009), pp. 323–343.
- [18] D. L. Donoho, *De-noising by soft-thresholding*, *IEEE transactions on information theory* **41** (1995), pp. 613–627.

ACKNOWLEDGEMENT

It is my greatest pleasure to thank those whose guidance and support have made this thesis possible. And I have heard that this is the only holy part of the thesis that would not get revised, so I will just start blabbing.

First of all, I would like to thank my supervisor **Dr. Eric Verschuur**, who have been influencing and inspiring me greatly. Regarding your supervision on my research, I have one sentence to summarize it: your office is a magic place. When entering your office → full of questions, doubts, anxieties; when getting out of your office → full of hope, confidence, joyfulness. Regarding your guidance on how to be a good researcher/person, I remember, before I met you, I had never dared to ask "potentially silly" questions or to express my own/oppose opinions to senior researchers. In the past several years, you have created such a comfortable research environment, where I feel being respected as a researcher whose words are worth listening to, I feel being regarded as a human who is allowed to not know something or make mistakes, and I feel being treated as a friend who can joke around and share life and feelings. I remember, in my first Delphi meeting in Houston, I was so nervous and armed with my broken English as well, I could not understand any of the questions sponsors asked, you helped me out. We met in the elevator later on, instead of scolding me, you told me: "Shan, you were doing all right, you will get better and better with it over time". And etc. You have never pushed me to work hard, somehow, I just keep trying to be a better version of me to live up to your kind words. Thanks for your trust. I am indeed Shan 2.0 now and will keep updated.

Additionally, I would like to thank my supervisor **Dr. Yimin Sun** during my internship in Aramco, from whom I have learned so much. Except for the project we have worked on, you also instructed me how to write better codes, most importantly, you are the one who taught me some philosophy of doing research, which has totally changed my research mindset: "Every method has its own downsides, do not be afraid of facing your methods', just keep trying to make them better.", "It is common that some of your ideas would not work in the end, but the efforts you have paid are still worthy because you have learned. Someday, after you have learned more, you might somehow make them work." Thank you very much for sharing your wisdom with me.

I am grateful to my committee members for reviewing my thesis. Especially, I thank **Dr. M. Houbiers** from Equinor for your remarkable comments on my project, abstracts, and papers throughout my whole Ph.D.. Many thanks to **Dr. A.K. Soni** from Shell for your helpful remarks on my thesis. I thank **Prof. C. MacBeth** for the fruitful discussions at various conferences and your inspiring course during your visit in Delft.

I would like to acknowledge all the sponsors of Delphi consortium for the useful and inspiring feedback at all the Delphi meetings. I also thank **Dr. Gerrit Blacquiere** and **Dr. Femke Vossepoel** for their inspiring presentations in the Delphi meetings.

I would like to thank my other promoter **Prof. Nico de Jong** for his help and support on my project. I would also like to thank **Prof. Kees Wapenaar**, **Dr. Guy Drijkoningen**, **Dr. Jan**

Thorbecke, Dr. Koen van Dongen, and Prof. Bernd Rieger for sharing wave-equation-related, seismic-geophysics-related, signal-processing-related, HPC-related knowledge with me. I also thank **Dr. Martin Verweij** for his inspiring remarks on my talks in seminars.

The staffs in the group have been most helpful. First thanks go to my department mom **Angela**, who has been not only patient and efficient in solving my problems but also has supported me when I felt down and shared happiness with us by inviting us over to her incredible farm house, and helped me out with my Dutch study. I would like to extend my gratefulness to my Delphi mom **Gerrie**, who has been not only a very good organizer but also such a big comfort when I was nervous and storming around outside presenting room before my talks. Many thanks to **Annelies** who has helped a lot during Angela's absence and will be bothered by me quite often in the future due to the department rearrangement. Thanks to **Margaret** for the tremendous help during the time before my Ph.D. and the early time of my Ph.D. journey. Thanks to **Henry, Ronald, and Edo** who have been frequently bothered by me with computer-related issues. Thanks to **Nicolette** for the relaxing conversations and good Chinese tea we have enjoyed together.

Special thanks go to my Delphi colleagues, we have shared so much happy time together, both in our daily life and during our traveling to conferences. You are the ones who make my Ph.D. journey less painful. I really enjoy the interesting conversations we have had, the moments we joked around and laughed hard and all the useful academic discussions we have had. I feel really lucky to have you guys to work with. I thank my Chinese mafia **Dong, Junhai, Tiexing, Lele, Runhai** and **Sixue**. What bonds us together beyond colleagues is not only the fact that we were born in the same country but also how sweet how supportive and most importantly how "Sao" you all are. I thank my dear friend **Aparajita**, I am really lucky to have you during my whole Ph.D., we have shared so many precious memories and laughter, and we have also gone through the tough periods with each other's company. I would like to thank **Matteo** and **Jan-Willem** for the great moments we have shared together in US and also for saving my life in Grand Canyon. Many thanks to **Leo** for helping me translate the summary of this thesis and also for playing board games and all the laughter we have had and will have together. I thank my previous officemates **Abdulrahman, Shogo, and Halah** and my current officemates **Mikhail** and **Siddarth**. I always feel delightful when I enter the office and see you guys in the office, thanks for your company. I also thank **Aayush, Ali, Apostolos, Billy, Shotaro, Özkan, Gabriel, Amarjeet, Bouchaib, Hussain, Nick, and Siamak**. I wish you all the best in your future and hopefully meet the guys in future conferences.

Special thanks go to my department colleagues, we are the luckiest ones in the whole TU Delft, because we own quite a lot fancy tables (table soccer table and table tennis table). What makes those tables fancy is mostly because of you guys who I have shared such a great time with in front of them. The happy moments we laughed and howled together in front of these tables are forever archived in my brain. Thanks to my lunch+tea+coffee+drink buddies **Boling, Tian, Wenxiu, Kefei**, together with **Tiexing, Junhai** and **Dong**, we are always able to get each other's "sao" jokes, I guess the frequency band of our minds is more or less the same. Those time I have spent with you is the most relaxing time during my Ph.D.. Thanks to my table tennis master **Jin** for teaching me how to play table tennis for several weeks, although I gave it up after I started dating, but one day master, forever master. Thanks to my special officemate **Yan** (me now is the office bird "Xiaoshan")

for the great time we have shared together. Thanks to **Leon** and his wife for their sinterklaas poem and gifts, which are the best gifts I have ever received in my life. Thanks to **Kerim** for the dinners we have shared together. I also thank **Gyllion the "mmp"**, **Jos the Chinese-speaker**, **Jos the table soccer king**, **Joost the great teacher**, **Verya**, **Moein**, **Jack**, **Elango**, **Fabian**, **Alberico**, **Boudewine**, and **Meysam** for the great conversations we have had and the inspiring medical-imaging presentations.


I would like to thank my Aramco oversea office colleagues during my internship **Janny**, **Paloma**, **Jewoo**, **Mikhail**, **Hannes**, **Rob** and **Roald** for the professional discussions and the relaxing lunch time we have shared together in Aula and in the office.

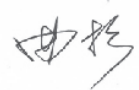
I want to thank my dear foreign friends, you are the ones who I believe it is really possible to make good friends across different cultures. I would like to thank **Divya** and **Anurag**, together with **Aparajita** for the great happiness we have shared together. It is always so much fun to hang out with you guys. I would like to thank **Joeri** and **Myrna** for the great trip in US we have shared together with **Matteo**, **Jan-Willem**, and **Paloma**. And I would never forget your worried faces when I was in the emergency room.

My dear Chinese friends in the Netherlands have made my life here full of love and laughter. I thank **Xinmin** and **Qian** for all the good memories we have shared. We have became friends at the beginning of our Ph.D. journey and we have witnessed and supported each other going through crests and troughs since then. I thank **Xue** for being great company in the first year of my Ph.D.. You have made my first year abroad much easier and full of happiness. Now you have a cute baby and live a good life in Dalian, wish you all the best. Before you left, you were afraid that I would be lonely, because it is not so good to be the bright bulb all the time between **Xinmin** and **Qian**. You then introduced **Hong** to me and told me you two can definitely make good friends. Since then, me and **Hong** really became good friends. Later on, **Bin** appeared in **Hong's** life, we then all became good friends. During our time together, there are always too strong exercises for my cheek muscles by laughing so hard. We feel happy for each other's happiness, we feel sad for each other's hard time. I thank **Jiao** and **Fei** for your delicious hand-made noodles and all the happy time we have shared. The only regretful thing is that how come we just started to become good friends around one year ago! It is never too late, I feel lucky that we eventually make friends and did not miss out each other. Hope we can spend the next spring festival together with your lovely baby as well. I would like to thank **Yifan**, it feels always so happy to spend time with you. You are telling the best jokes in Delft! Thanks to **Ding**, **Yun**, **Weichen**, **Bei**, **Xiujie Meng** and **Yin**, **Ze** and **Lu** for the great time and funny conversations we have had in different kinds of occasions.

My dear old friends all over the world, it is my luck to have you guys as friends in my life. Without your supports, though from distance, this thesis is not possible to exist. It turns out love force doesn't follow attenuation rule, how come the love from this long distance is still so strong! I thank my dear friends **Tian the Monster** and **Wolong**, when I have happy things, I want to share them with you immediately, when I have a hard time, I feel reassured to just know you guys will always be there for me, no matter how far away we are from each other. I thank **Miya the Xiaoru** for being a special guide of my life, your way of living a life full of wonders is always like a lighthouse for me. I have learned so much from seeing you growing up and from the conversations we have had every year I was back in China. I learned I should enjoy my life by staying curious and experiencing

different things, instead of just doing my research; I learned sometimes it is ok to say no to others. I thank **Zhiye** for all the interesting conversations we have had online, they helped me a lot to get through my tough first year abroad. I thank **Mo** for the wonderful time we have spent each year and also for your wisdom you have shared with me unreservedly. I have learned so much from you. You once told me "You shall not use your weak points to compete with other's strengths, you might be not excel at socializing, but you are so good at other things", etc. All these wise words affected me a lot and supported me to accomplish this thesis. I would like to thank **Qiang** for the wonderful moments we have spent together and all the supportive conversations we have had online during my whole Ph.D. journey. You are going to live a great life in UK and going to have a lovely baby. Wish you all the best. I thank **Mengqian the Tallest** and **Yang** for being supportive and contributing to my happiness these years. We have had such a happy time in Beijing each year. I would like to thank **Yangkang** for being my research lighthouse during my whole research life. Every time when I get spoiled by the leisure life in Delft and start to be too relaxed, I would receive your warnings via wechat. Your supportive words are one of the most important reasons of the existence of this thesis.

My family's consistent love and support have been my inner motive to finish the Ph.D. degree. My dear parents have always supported me. You are like the big ship with a spacious platform made of love in the ocean, when I am flying against the wind in the sky, I just feel so reassuring so lucky, because I know I always have a place to rest and totally relax. I would like to thank my dear **Glenn the Cat** for being such a lovely company during three quarters of my Ph.D. journey. My dear **Ulas**, I feel so blessed to have you appear in my life. I wish to have you stay aside in the rest of my life. You were such a big support when I was writing this thesis. The two cats on the cover  are a symbol of us.



Shan Qu
Delft, the Netherlands
January, 2020

CURRICULUM VITÆ

Shan Qu

12-Feb-1991 Born in Dandong, Liaoning, China.

EDUCATION

- 2014–2019 Ph.D candidate in Applied Physics
Delft University of Technology, Delft, The Netherlands
- 2011–2014 M.E in Geophysical Prospecting and Information Technology (cum laude)
China University of Petroleum, Beijing, China
- 2008–2012 B.S in Geophysics
China University of Petroleum, Qingdao, China

RESEARCH EXPERIENCE

- 2019–present Post-doc researcher
Delft University of Technology, Delft, The Netherlands
Research on Joint Migration Inversion
- 2017–2018 Research intern
EXPEC ARC GRC Delft, Aramco Overseas Company B.V., Delft, The Netherlands
Research on Joint Migration Inversion as an intern project
- 2015–2019 Ph.D. candidate
Delft University of Technology, Delft, The Netherlands
Research on Time-lapse Application in Joint Migration Inversion
- 2012–2015 Graduate student
China University of Petroleum, Beijing, China
Research on Simultaneous Source Acquisition and Blended Data Processing
- 2012–2015 Graduate student
China University of Petroleum, Beijing, China
Research on Vibroseis Acquisition and Harmonics Removal

LIST OF PUBLICATIONS

JOURNAL PAPERS

6. **S. Qu** and D.J. Verschuur, *Simultaneous Joint Migration Inversion with calendar-time constraints as a processing tool for semi-continuous surveys*, *Geophysics*, (under review).
5. **S. Qu** and D.J. Verschuur, *Simultaneous joint migration inversion for high-resolution imaging/inversion of time-lapse seismic datasets*, *Geophysical Prospecting* (2019), (online).
4. **S. Qu**, Z. Guan, D.J. Verschuur, and Y. Chen, *Automatic high-resolution microseismic event detection via supervised machine learning*, *Geophysical Journal International* **43** (2019), pp. 2106–2121.
3. **S. Qu**, D.J. Verschuur, and Y. Chen, *Full-waveform inversion and joint migration inversion with an automatic directional total variation constraint*, *Geophysics* **84** (2019), pp. R175–R183.
2. **S. Qu**, H. Zhou, R. Liu, Y. Chen, S. Zu, S. Yu, J. Yuan, and Y. Yang, *Deblending of Simultaneous-source Seismic Data using Fast Iterative Shrinkage-thresholding Algorithm with Firm-thresholding*, *Acta Geophysica* **64** (2016), pp. 1064–1092.
1. **S. Qu**, H. Zhou, Y. Chen, S. Yu, H. Zhang, J. Yuan, Y. Yang, and M. Qin, *An effective method for reducing harmonic distortion in correlated vibroseis data*, *Journal of Applied Geophysics* **115** (2015), pp. 120–128.

CONFERENCE PAPERS

14. **S. Qu** and D.J. Verschuur, *A robust high-resolution time-lapse Simultaneous Joint Migration Inversion process applied to synthetic data from Grane field*, in *81th EAGE Conference and Exhibition 2019* (Eur. Ass. of Geosc. and Eng., Expanded abstracts, 2019).
13. **S. Qu** and D.J. Verschuur, *A Robust High-resolution Time-lapse Simultaneous Joint Migration Inversion Process Applied to the Time-lapse Troll Field Datasets*, in *Second EAGE Workshop on Practical Reservoir Monitoring 2019* (Eur. Ass. of Geosc. and Eng., Expanded abstracts, 2019).
12. **S. Qu** and D.J. Verschuur, *Simultaneous Joint Migration Inversion applied to the time-lapse field datasets from the Troll field*, in *EAGE Workshop on 4D Seismic and Reservoir Monitoring: Bridge from Known to Unknown* (Eur. Ass. of Geosc. and Eng., Expanded abstracts, 2018).
11. **S. Qu**, D.J. Verschuur, and Y. Chen, *Automatic microseismic-event detection via supervised machine learning*, in *SEG Technical Program Expanded Abstracts 2018* (Society of Exploration Geophysicists, 2018) pp. 2287–2291.
10. **S. Qu**, Y. Sun, and D.J. Verschuur, *Mitigating amplitude versus ray-parameter effect in joint migration inversion using a zero-lag crosscorrelation objective function of redatumed wavefields*, in *SEG Technical Program Expanded Abstracts 2018* (Society of Exploration Geophysicists, 2018) pp. 1133–1137.

9. **S. Qu** and D.J. Verschuur, *Time-lapse Simultaneous Joint Migration Inversion for high-resolution imaging/inversion based on a realistic synthetic model from the Grane field*, in [SEG Technical Program Expanded Abstracts 2018](#) (Society of Exploration Geophysicists, 2018) pp. 5362-5366.
8. **S. Qu** and D.J. Verschuur, *Simultaneous Joint Migration Inversion applied to the time-lapse field datasets from the Troll field*, in [80th EAGE Conference and Exhibition 2018](#) (Eur. Ass. of Geosc. and Eng., Expanded abstracts, 2018).
7. **S. Qu** and D.J. Verschuur, *Simultaneous joint migration inversion for semicontinuous time-lapse seismic data*, in [SEG Technical Program Expanded Abstracts 2017](#) (Society of Exploration Geophysicists, 2017) pp. 5808-5813.
6. **S. Qu**, D.J. Verschuur, Y. Chen, *Full Waveform Inversion Using an Automatic Directional Total Variation Constraint*, in [79th EAGE Conference and Exhibition 2017](#) (Eur. Ass. of Geosc. and Eng., Expanded abstracts, 2017).
5. **S. Qu** and D.J. Verschuur, *Simultaneous Joint Migration Inversion for Accurate Time-lapse Analysis of Sparse Monitor Surveys*, in [First EAGE Workshop on Practical Reservoir Monitoring](#) (Eur. Ass. of Geosc. and Eng., Expanded abstracts, 2017).
4. **S. Qu** and D.J. Verschuur, *Simultaneous time-lapse imaging via Joint Migration Inversion*, in [78th EAGE Conference and Exhibition 2016](#) (Eur. Ass. of Geosc. and Eng., Expanded abstracts, 2016).
3. **S. Qu** and D.J. Verschuur, *Getting accurate time-lapse information using geology-constrained Simultaneous Joint Migration Inversion*, in [SEG Technical Program Expanded Abstracts 2016](#) (Society of Exploration Geophysicists, 2016) pp. 5451–5456.
2. **S. Qu**, H. Zhou, J. Yuan, M. Qin, and H. Zhang, *An effective denoising method for removing harmonic distortion in correlated vibroseis data*, in [SEG Technical Program Expanded Abstracts 2014](#) (Society of Exploration Geophysicists, 2014) pp. 4284-4288.
1. **S. Qu**, H. Zhou, H. Chen, S. Zu, and L. Zhi, *Separation of simultaneous vibroseis data*, in [SEG Technical Program Expanded Abstracts 2014](#) (Society of Exploration Geophysicists, 2014) pp. 4340-4344.